

Submitted by
Dogukan Hazar Apaydin

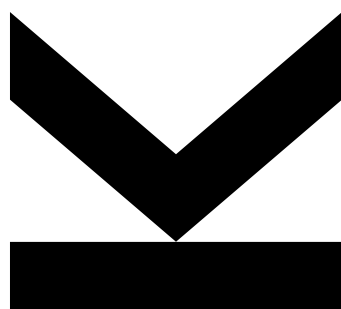
Submitted at
**Linz Institute for Organic
Solar Cells (LIOS) / Institute
of Physical Chemistry**

Supervisor and
First Examiner
**Prof. Dr. Niyazi Serdar
Sariciftci**

Second Examiner
Prof. Dr. Günther Knör

February 2018

Electrocatalytic Applications of Organic Semiconductors



Doctoral Thesis

to obtain the academic degree of

Doktor der Naturwissenschaften

in the Doctoral Program

Technical Chemistry

STATUTORY DECLARATION

I hereby declare that the thesis submitted is my own unaided work, that I have not used other than the sources indicated, and that all direct and indirect sources are acknowledged as references.

This printed thesis is identical with the electronic version submitted.

Place, Date

Signature

ABSTRACT

With the announcement of Nobel Prize in chemistry in 2000, organic semiconductors and conjugated structures have been used for various applications like organic solar cells (OSCs), organic light emitting diodes (OLEDs), organic field effect transistors (OFETs). Due to the common belief in their instability in solutions (both in organic and in aqueous) exploration of their activity as catalytic materials remains mainly unexplored. This study aims to explore catalytic properties of organic semiconductors with a heterogeneous approach. As a first step a well-known organic semiconductor, polythiophene is used as backbone for the immobilization of metal complexes which are capable of reducing CO₂ to further products. This combined with photoactive property of polythiophene enabled the photoelectrocatalytic reduction of carbon dioxide. Apart from fixing the catalyst on the electrode via polymerization, anchoring of the catalyst CuTPP-COOH for driving the photoelectrochemical reduction of O₂ to H₂O₂ was also carried out. CuTPP-COOH supported on TiO₂ NTs showed good stability over time and more importantly reduced dissolved oxygen to hydrogen peroxide in neutral pH with a rate of 13.4 μg H₂O₂ / g_{CuTPP-COOH} / h. This value is comparable to the well-known literature examples of ZnO and g-C₃N₄. In another approach H-bonded semiconductors, namely Quinacridone, Indigo and naphthalene diimide, were utilized as efficient carbon dioxide (CO₂) capturing agents in organic solvents as well as in aqueous media. These compounds showed uptake capacities of 4.6 mmol.g⁻¹ and 2.3 mmol.g⁻¹ which are comparable to state-of-the-art amine based capturing agents (uptake capacity of 8 mmol.g⁻¹).

KURZFASSUNG

Spätestens seit der Bekanntgabe des Nobelpreises für Chemie im Jahr 2000 wurden vermehrt organischer Halbleiter und konjugierter Strukturen für verschiedene Anwendungen wie organische Solarzellen (OSCs), organische Leuchtdioden (OLEDs), organische Feldeffekttransistoren (OFETs) verwendet. Aufgrund des allgemeinen Glaubens an ihre Instabilität in Lösungen (sowohl in organischen als auch in wässrigen) bleibt die Erforschung ihrer Aktivität als katalytisches Material weitgehend vernachlässigt. Diese Studie zielt darauf ab, katalytische Eigenschaften von organischen Halbleitern mit einem heterogenen Ansatz zu erforschen. In einem ersten Schritt wurde ein bekannter organischer Halbleiter, Polythiophen, als Rückgrat zur Immobilisierung von Metallkomplexen verwendet, die in der Lage sind, CO₂ zu weiteren Produkten zu reduzieren. In Kombination mit der photoaktiven Eigenschaft von Polythiophen ermöglichte dies die photoelektrokatalytische Reduktion von Kohlendioxid. Neben der Fixierung des Katalysators auf der Elektrode durch Polymerisation wurde auch der Katalysator CuTPP-COOH zur Steuerung der photoelektrochemischen Reduktion von O₂ zu H₂O₂ verankert. Das durch TiO₂-NTs getragene CuTPP-COOH zeigte im Laufe der Zeit eine gute Stabilität und, was noch wichtiger ist, reduzierte gelösten Sauerstoff zu Wasserstoffperoxid bei neutralem pH-Wert mit einer Rate von 13.4 µg H₂O₂ / g_{CuTPP-COOH} / h. Dieser Wert ist vergleichbar mit den bekannten Literaturbeispielen von ZnO und g-C₃N₄. In einem anderen Ansatz wurden H-gebundene Halbleiter, nämlich Chinacridon, Indigo und Naphthalin-Diimid, als wirksame Kohlendioxid-(CO₂)- Speicheragenten sowohl in organischen Lösungsmitteln als auch in wässrigen Umgebungen verwendet. Diese Zusammensetzungen zeigten Aufnahmekapazitäten von 4.6 mmol.g⁻¹ und 2.3 mmol.g⁻¹, was sie vergleichbar macht mit den sich auf dem Stand der Technik befindlichen Amine-basierten Speicheragenten (Aufnahmekapazität von 8 mmol.g⁻¹).

Acknowledgements

First and foremost, I would like to express my gratitude to my supervisor Prof. Dr. Niyazi Serdar Sariciftci who not only taught me to be a good scientist with a skepticism-driven approach but also to be a better and active member of the society. For these and for many other reasons that I am not able to list here I am eternally grateful.

Furthermore, I would like to thank my second supervisor Prof. Dr. Günther Knör for always supporting me and always sparing time for extended discussions in order to answer my questions.

A big thank you goes to Assoc. Prof. Dr. Markus C. Sharber and Dr. Helmut Neugebauer for teaching me how to approach a problem and how to always be self-critical with my results. I have learned that the right amount of skepticism is important for achieving good results!

This study would not be possible without the immense support I have given by Gerda Kalab, Gabriele “Gabi” Hinterberger, Birgit Paulik, Nadja Aichinger and Patrick Denk. They were always there for me when I needed help. I am grateful to Birgit and Nadja for helping me through the labyrinths of bureaucracy. I am thankful to Gerda and Gabi for encouraging me to learn and speak German and for always being there when I needed friendly advice.

Throughout this thesis, I have had the privilege to work with great students. Dominik Wielend, Kathrin Ebner, Hathaichanok “Hathai” Seelajaroen, Nikolas Heitzmann and Zoja Lakovic; I am grateful to you for always being curious and not holding back to push me to reach the information you would like to have. I have learned a great deal from you and I am also lucky to have you as friends.

I owe a great deal to my friends, Cigdem Yumusak, Mateusz Bednorz, Engelbert Portenkirchner, Martin Kaltenbrunner, Jacek Gasiorowski, Zeynep Bozkurt, Kerstin Oppelt, Monika Gora, Marzena Grucela, Stefanie Schlager, Dong Whang, Elisa Tordin, Lucia Leonat, Nevsal Sünger, Patchanita Thamyongkit and Oleksandr Boiko who have been the absolute motivation and source of fun in LIOS through my PhD.

Words are not sufficient when it comes to explain my gratitude to Daniela Neubacher. You are my source of inspiration, my motivation and my never-lasting support! I am really lucky to have you!

Finally, I would not be able to carry out this thesis without the support of my family! For that I am eternally grateful. A special thank you goes to my parents in Austria, Josef and Brigitte, who accepted me as their own and have always supported me!

The last but not least I am truly thankful to the members of LIOS team who taught me the value of friendship and how to be a big family!

Table of Contents

ABSTRACT	iii
KURZFASSUNG	iv
Acknowledgements.....	v
List of Figures	viii
1. Introduction.....	1
1.1. Greenhouse Gases and Climate Change	1
1.1.1. On the Thermodynamics of Carbon Dioxide	3
1.2. Carbon Capture and Storage.....	4
1.3. Hydrogen Peroxide as Alternative Chemical Energy Storage Medium.....	6
1.4. Homogeneous vs. Heterogeneous Catalysis	7
1.4.1. Organic Semiconductors	8
1.4.2. Electrochemical and Photoelectrochemical Reduction of Carbon Dioxide	10
1.4.2.1. Homogeneous Approaches.....	10
1.4.2.2. Heterogeneous Approaches.....	12
2. Experimental Methods and Materials	15
2.1. Materials.....	15
2.2. Methods	16
2.2.1. Electrochemistry	16
2.2.2. Fourier Transform Infrared Spectroscopy	21
2.2.2.1. <i>In-situ</i> ATR-FTIR Spectroelectrochemistry	23
2.2.3. UV-Vis Spectroscopy.....	25
2.2.4. Gas Chromatography	25
2.2.5. Scanning Electron Microscopy.....	26
2.2.6. Electrode Preparation and Cleaning	26
2.2.7. Electrochemical Impedance Spectroscopy	26
3. Results and Discussion.....	31
3.1. Carbon Capture and Storage (CCS) Using H-Bonded Pigments	31
3.1.1. Carbon Capture and Storage in Organic Solvents	31
3.1.2. Carbon Capture and Storage (CCS) in Aqueous Medium.....	38
3.2. Heterogeneous Photoelectrocatalysis Using Organic Semiconductor Modified Electrodes	46
3.2.1. Third Generation of Conjugated Polymers for CO ₂ Reduction	46
3.2.2. Photoelectrochemical Reduction of O ₂	55
4. Conclusions and Outlook	65
4.1. Conclusions.....	65

4.2. Outlook.....	67
5. References	68
6. Curriculum Vitae	77

List of Figures

Figure 1. Depiction of factors affecting the climate.	1
Figure 2. Possible products that can be derived from carbon dioxide.	2
Figure 3. Gibbs Free Energy diagram for carbon dioxide and other hydrocarbons (on the left). Correlation between standard Gibbs energy of reaction ($\Delta^R G$) and reaction equilibrium (on the right).	3
Figure 4. Formal thermodynamic potentials for conversion of carbon dioxide (adjusted for pH 7 vs. NHE).	3
Figure 5. A campaign poster designed to promote CO ₂ capture and underground storage.	4
Figure 6. Energy level diagram of a p-type semiconductor-electrolyte interface, before contact and at equilibrium.	8
Figure 7. Schematic representation of band bending at electrode-electrolyte interface in semiconductors. (a) n-type and (b) p-type.	9
Figure 8. Effect of applied potential on the band edges of the bulk of the semiconductor.	10
Figure 9. Chemical structure of Re(bpy)(CO) ₃ Cl where bpy is 2,2'-bipyridine.	11
Figure 10. Set of equations leading to the formation of sparingly-soluble dimer.	11
Figure 11. Reaction pathways suggested by Sullivan <i>et al.</i> ⁸⁷	12
Figure 12. Potentiodynamic formation of Lehn catalyst bearing polymer.	14
Figure 13. Potential waveform in cyclic voltammetry.	16
Figure 14. Photos of a one-compartment cell (a) and a two-compartment cell (b).	17
Figure 15. Typical cyclic voltammogram of Ferrocene / Ferrocenium couple.	17
Figure 16. Photo of a photoelectrochemical experiment in progress.	18
Figure 17. A typical current-time curve used for extracting the charges consumed during electrolysis.	19
Figure 18. Current-time curve used for calculating the number of active molecules on an electrode.	20
Figure 19. Schematics of an IR spectrophotometer.	21
Figure 20. Schematic of the IR transmission cell.	21
Figure 21. FTIR spectrum of CO ₂ and CO.	22
Figure 22. Photo of the ATR-FTIR thin film measurement setup. Magnified photo of the actual measurement area (inset).	23
Figure 23. A photo of the Ge reflection element (on the left) and disassembled electrochemical cell (on the right).	24
Figure 24. A schematic representation of ATR-FTIR spectroelectrochemistry cell.	24
Figure 25. Photo of the Thermo Scientific Trace GC Ultra (on the left) and two typical chromatograms (overlaid) showing the detectable products.	25
Figure 26. A sinusoidal potential pulse and its current response in an alternating current system.	27
Figure 27. Schematic representation of a typical Nyquist plot.	28
Figure 28. A representative Bode plot (Image taken from Gamry Instruments website).	29
Figure 29. An equivalent circuit model where R _s is the solution resistance, C _{dl} is a double layer capacitor and R _{ct} is charge-transfer resistance (image taken from Gamry Instruments website).	29
Figure 30. A typical EIS cell during assembly (on the left) and before measurement in a Faraday cage (on the right).	30

Figure 31. Chemical structure of Quinacridone	31
Figure 32. Photo of a ~100 nm Quinacridone thin film on an ITO coated glass slide.	32
Figure 33. Electrochemical behavior of QNC under N ₂ (blue curve), under CO ₂ (red curve) and after CO ₂ release (green curve).	32
Figure 34. Setup used for the time-dependent release of CO ₂ from the QNC electrode upon heating.....	33
Figure 35. Release of CO ₂ over time upon heating the electrode.	34
Figure 36. Cyclic voltammetry of QNC thin film depicting the electrochemical capture and release of CO ₂	35
Figure 37. Overall equation for capture of CO ₂ by a QNC molecule (a). Proposed mechanism for capture and release of CO ₂ (b).	36
Figure 38. Electrosynthesis of poly(dithienyl indigo) (PDTI).....	37
Figure 39. Electrochemical behavior of PDTI under N ₂ (blue curve) and under CO ₂ (red curve).	38
Figure 40. Chemical structure of 2,7-bis(4-(2-(2-ethylhexyl)thiazol-4-yl)phenyl)benzo[Imn][3,8]phenanthroline- 1,3,6,8(2H,7H)-tetraone (NBIT) (a). DFT calculations showing the HOMO and LUMO levels of NBIT.....	39
Figure 41. Two-compartment electrochemical cell.	40
Figure 42. Electrochemical behavior of NBIT under N ₂ (red curve) and under CO ₂ (blue curve). Inset: Proposed mechanism for CO ₂ capture.	41
Figure 43. Cyclic stability of NBIT upon repetitive potential cycling.	41
Figure 44. (a) CV of NBIT film on a glassy carbon electrode (WE) with colored points indicating the potentials of EIS data acquisition shown in b and c. Nyquist plots of NBIT film on a glassy carbon electrode (b) under Ar and (c) under CO ₂ respectively.	42
Figure 45. Corresponding equivalent electrical circuits for EIS data fitting of NBIT under (a) Ar atmosphere and (b) CO ₂ atmosphere at -1.0V and below, consisting of the ohmic resistance of the electrolyte solution (R _s), the double layer capacitance (C _{dl}) and the charge transfers resistance (R _{ct}). While under Ar saturation the EIS data can be well explained by a single R/C element in series with the R _s two R/C elements have to be used, in series with the R _s , to fit the spectra under CO ₂ saturation at -1.0V and below.....	43
Figure 46. <i>In-situ</i> ATR-FTIR-SPEC spectrum of NBIT under CO ₂	44
Figure 47. Cyclic voltammogram of NBIT under N ₂ (red curve), after CO ₂ capture (blue curve) and after CO ₂ release (green curve).	45
Figure 48. Three generations of conjugated polymers; a) Polymers with good conductivity but low processibility, b) Polymers with alkyl chains allowing solubility hence processibility, c) Polymers with good conductivity, processibility and/or new chemical/physical functions/properties.	46
Figure 49. Chemical structure of P[3HRe(bpy)(CO) ₃ Cl-Th].	48
Figure 50. Electropolymerization of [3HRe(bpy)(CO) ₃ Cl-Th]. Inset: Photo of a very-thick polymer film for visualization.....	49
Figure 51. Electropolymerization of [3HPyr-Th].	49
Figure 52. Reflectance spectrum of P[3HRe(bpy)(CO) ₃ Cl-Th].....	50
Figure 53. Electrochemical behavior of P[3HRe(bpy)(CO) ₃ Cl-Th] in dark and under illumination (60 mW/cm ²).	51
Figure 54. Working principle of the polymeric catalyst upon irradiation with light. H ₂ can also be observed as a product when the electrolyte medium is protic.	53
Figure 55. Current increase upon the saturation of electrolyte solution with CO ₂	54

Figure 56. Electrochemical behavior of P[3HPyr-Th] under N ₂ and CO ₂ -saturated conditions upon illumination.	55
Figure 57. Chemical structure of CuTPP-COOH.	55
Figure 58. TiO ₂ NTs bearing electrode before (on the left) and after coating with CuTPP-COOH (on the right).	56
Figure 59. SEM images of TiO ₂ NTs (on the left) and CuTPP-COOH coated TiO ₂ NTs (on the right).	58
Figure 60. ATR-FTIR spectrum of the electrode TiO ₂ NTs / CuTPP-COOH.	59
Figure 61. Possible binding modes of –COOH group on TiO ₂ . (Reproduced with permission) ..	59
Figure 62. Chronoamperometry experiments conducted on TiO ₂ NTs / CuTPP-COOH under Argon (a) and under O ₂ -saturated conditions.	60
Figure 63. Calibration curve used for quantifying the produced H ₂ O ₂ . Reaction leading to <i>p</i> -NP formation (upper left inset). Increase in absorbance with increasing concentration of H ₂ O ₂ (lower right inset). Points with turquoise color are the concentrations of H ₂ O ₂ obtained from electrolysis at constant potentials of -0.05 V and -0.3 V vs. NHE.	61
Figure 64. Nyquist plots for illuminated, porphyrin covered TiO ₂ NTs at – 0.2 V vs. NHE under Ar (squares) and O ₂ (circles) saturation in 0.1 M Na ₂ SO ₄ . Symbols represent the experimental data and the dashed lines are only a guide for the eye with no physical meaning. (a) Illustration of the semi-circle (III) at low frequencies between 0.94 Hz and 20 mHz, which is only observable when the electrolyte is saturated with O ₂ , (b) magnification of the high frequency domain in (a), highlighted with the blue dashed square, to illustrate the second semi-circle (II) at medium frequencies between 65 Hz and 1.4 Hz; The finite length Warburg impedance (ZW) under O ₂ (circles) saturation is indicated by a green dashed line with a slope of 45°. (c) Magnification of the high frequency domain in (b), highlighted with the blue dashed square therein, to illustrate the onset of semi-circle (I) at high frequencies between 4.5 kHz and 200 Hz.	62
Figure 65. Nyquist plots at different potentials for TiO ₂ NTs / CuTPP-COOH electrode (illuminated) under (a) Ar and (b) O ₂ -saturated conditions. Symbols represent the experimental data and the lines the best fit. (c) Enlarged view of the high frequency domain of (b) indicated therein with a grey, dashed square. (d) Equivalent electric circuit used for fitting the EIS data. R _s : solution resistance, R _f and C _f : interfacial TiO ₂ NTs / CuTPP-COOH electron charge transfer resistance and the corresponding capacitance, R _{tr} and CPE _{nt} : resistance for electron transport along the TiO ₂ NTs and the corresponding capacitance (modelled with a CPE), ZW: Warburg element for semi-infinite diffusion, R _r and CPE _r : charge transfer resistance for the O ₂ reduction and corresponding capacitance (modelled with a CPE).	63
Figure 66. Bode plot at -0.3 V vs. NHE for illuminated, porphyrin covered TiO ₂ NTs under O ₂ -saturated conditions. Symbols represent the experimental data and the dashed lines the corresponding best fit in the frequency range from 10 kHz to 20 mHz.	64
Figure 67. Homogeneous vs. Heterogeneous catalysis.	65

1. Introduction

1.1. Greenhouse Gases and Climate Change

According to the Intergovernmental Panel on Climate Change (IPCC) a greenhouse gas can be defined as a constituent of the atmosphere which absorbs and emits radiation at a specific wavelength within the spectrum of thermal infrared radiation originating from Earth's surface, clouds and atmosphere itself¹. Hence the effect caused by such gases is called greenhouse effect which has been keeping the scientists, researchers, politicians and public busy since decades. According to their potency the greenhouse gases can be listed as follows²:

- Water vapor (H₂O)
- Carbon dioxide (CO₂)
- Methane (CH₄)
- Nitrous oxide (N₂O)
- Ozone (O₃)

To talk about climate change one should consider the definitions of “climate” and “weather” first. While it is a challenging task to predict the weather for the next couple days, the prediction of climate behavior is relatively easier for scientists. Climate can be defined as the long-term average weather and making predictions on its behavior is easier by looking at atmospheric composition. As a simple analogy; we are not able to predict the age when a certain individual will die. However, it is relatively easy to say that a human's average lifetime is around 75 years in developed countries².

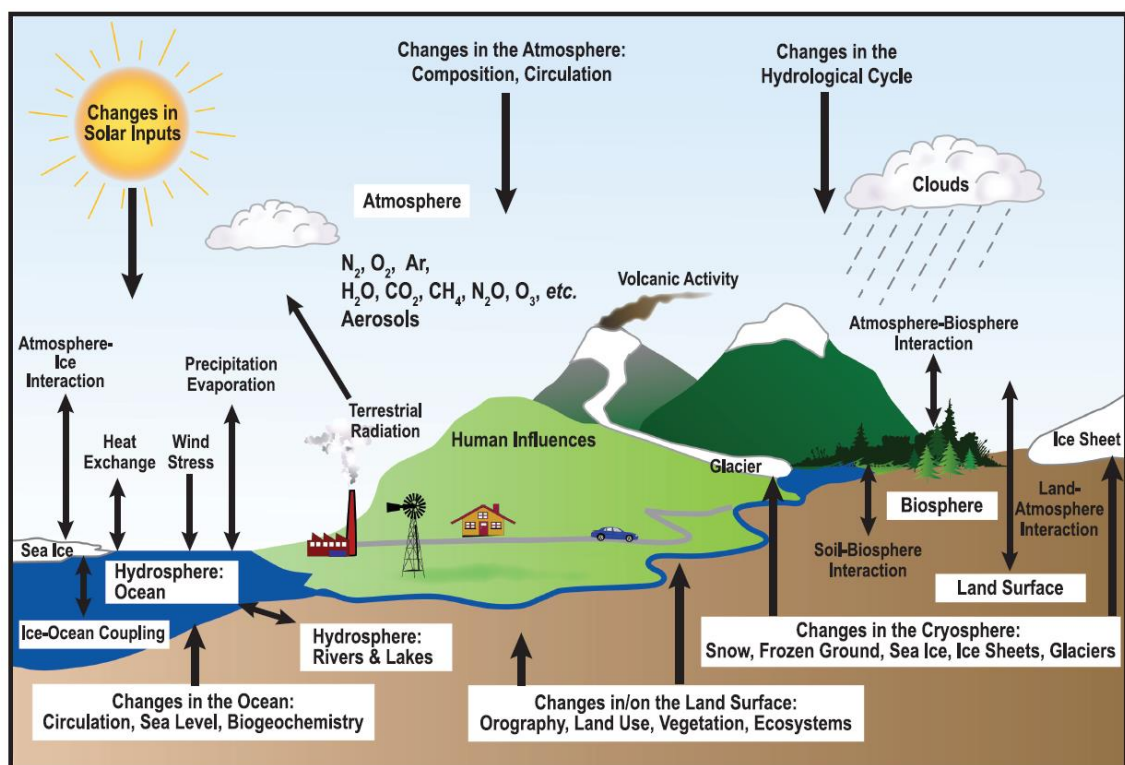


Figure 1. Depiction of factors affecting the climate.

It is important to know that local extreme cold weather or long winters is not an evidence against the climate change. Earth has witnessed such extreme cold and hot events. It is not the event itself that changes but its frequency that is affected by the changes in climate. There are many factors affecting the climate which are beyond the scope of this thesis.

We can ask ourselves why, if carbon dioxide is the second in potency as a greenhouse gas, scientists are interested in addressing the issue of anthropogenic (human-originated) carbon dioxide in the atmosphere more urgently than the others? When concentration in the atmosphere of each gas is considered the amount of water vapor in Earth's atmosphere is on the order of 10000-50000 ppm while carbon dioxide has concentration of ~ 400 ppm. The answer lies in a specific important parameter which is called "atmospheric lifetime". Atmospheric lifetime can be defined as the time (in years) a greenhouse gas spends in the atmosphere which results in a global concentration all over the world. For water vapor the atmospheric lifetime is in the order of days while for carbon dioxide it is somewhere between 30-100 years which makes it our prime concern³.

This concern is being tackled by many scientists around the globe to ensure a less carbon-dependent future. There are two main approaches in tackling this global problem. The first one is Carbon Capture and Storage where carbon dioxide is captured either from the atmosphere or at the point of released and stored underground facilities (CCS). This approach will be discussed in detail in the following chapters. The second approach is called Carbon Capture and Utilization (CCU) which allows us to convert carbon dioxide into higher hydrocarbons.

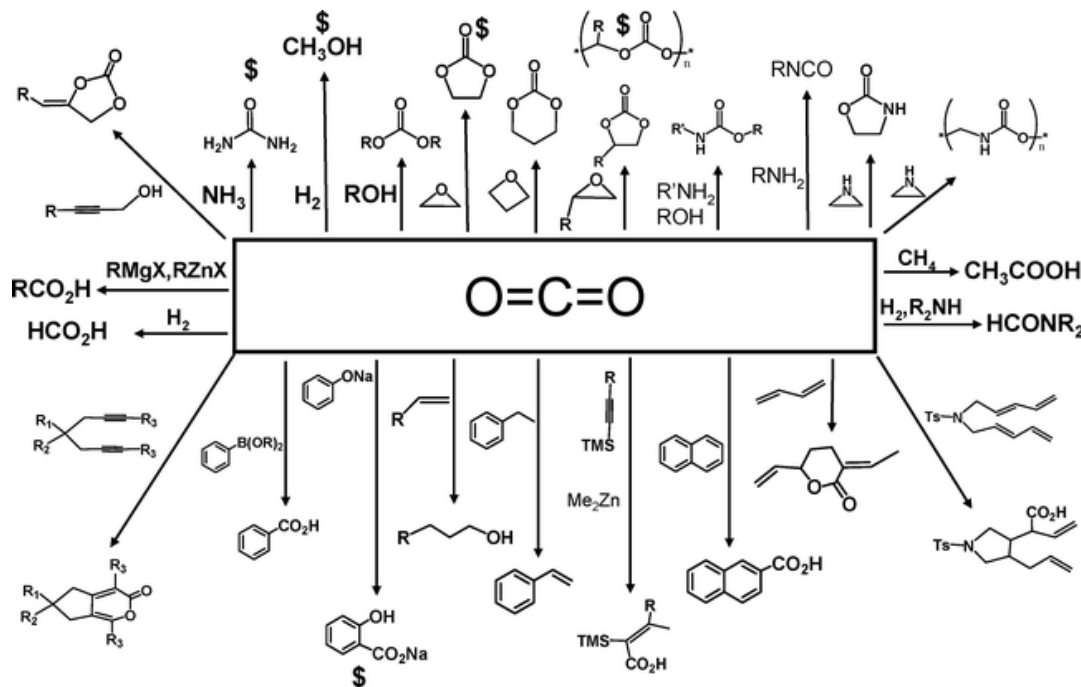


Figure 2. Possible products that can be derived from carbon dioxide.

1.1.1. On the Thermodynamics of Carbon Dioxide

To address the anthropogenic CO₂ issue we have to look at the molecule itself. Carbon dioxide is a thermodynamically stable linear molecule with a Gibbs free energy of formation, ΔG°_f of -394.4 kJ/mol. This makes the conversion of carbon dioxide to higher hydrocarbons highly challenging^{4,5}.

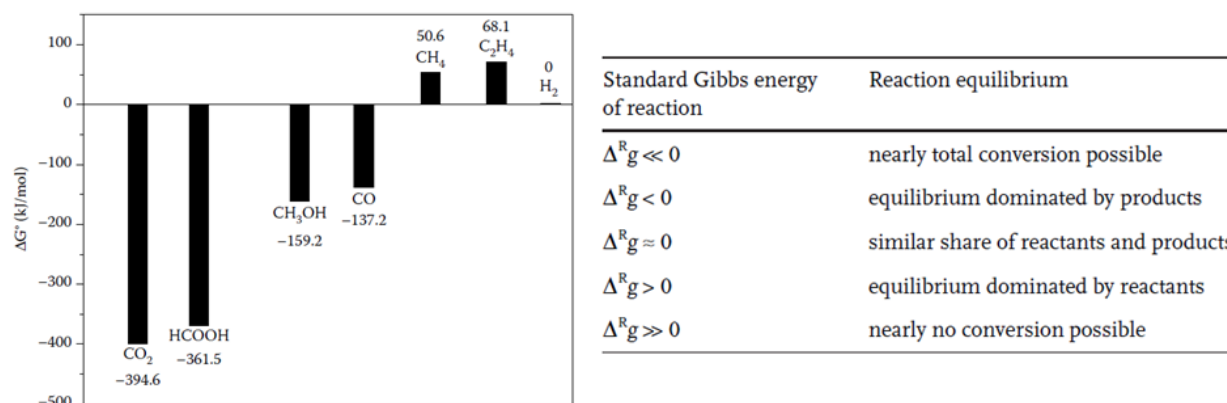


Figure 3. Gibbs Free Energy diagram for carbon dioxide and other hydrocarbons (on the left). Correlation between standard Gibbs energy of reaction ($\Delta^R g$) and reaction equilibrium (on the right).

The other important aspect one needs to take into account is the kinetics of the process where CO₂ is converted to 1-electron reduced carbon dioxide radical where a change in the hybridization from sp to sp² is occurred followed by a change in the linearity of the molecule upon bending^{6,7}.

However, addressing the stability of carbon dioxide and its conversion reactions to higher hydrocarbons using Gibbs free energy can be confusing and not straightforward. For that purpose the field of catalysis uses redox potentials to define the conversion of carbon dioxide. A typical table with redox potentials is given below:

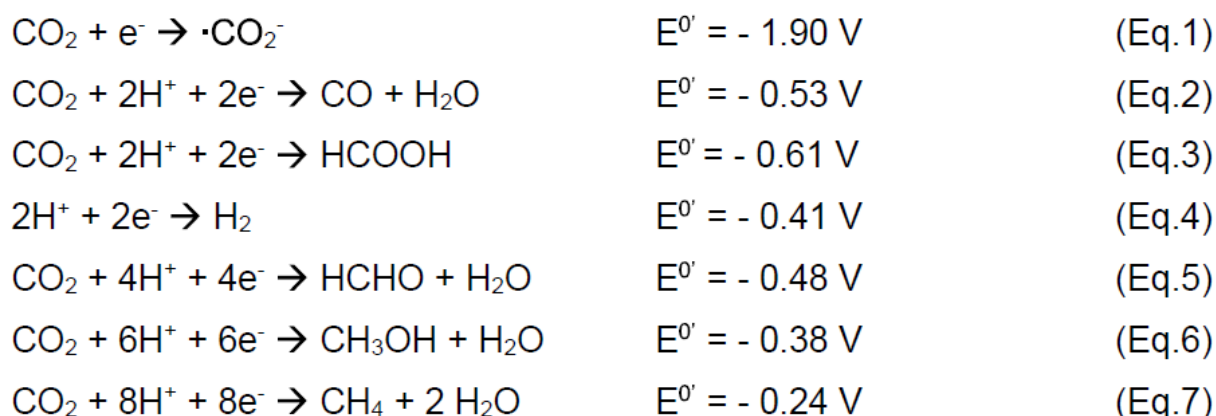


Figure 4. Formal thermodynamic potentials for conversion of carbon dioxide (adjusted for pH 7 vs. NHE).

This requires the use of special molecules called catalysts. Catalysts are molecules that change (increase) the rate of a reaction and they continue to do so as long as a certain substrate is there to react with. Conversion of carbon dioxide to higher hydrocarbons requires the use of the catalysts. In addition, the need of high energy to convert carbon dioxide calls for non-carbon energy sources like wind and solar energy for conversion. Together with non-carbon energy sources used in CO₂ reduction together with reduction in overall carbon emission can result in a carbon-neutral cycle.

Reduction of carbon dioxide can be achieved via several approaches:

- Electrochemical reduction of carbon dioxide
- Photochemical reduction of carbon dioxide
- Photoelectrochemical reduction of carbon dioxide

This thesis focuses on both of the approaches for addressing the existing problem of carbon dioxide in the atmosphere.

In addition to carbon dioxide, photoelectrochemical synthesis of another chemical energy storage medium, *i.e.* hydrogen peroxide will be discussed.

1.2. Carbon Capture and Storage

Carbon capture constitutes the initial step for both storage and utilization of CO₂. Although atmospheric concentration of CO₂ reaches a threatening value of ~400 ppm this concentration is still not feasible enough to efficiently capture CO₂ from the atmosphere directly. Concentration of carbon dioxide for addressing its further reaction is a necessary step. Direct atmospheric capture of CO₂ is not energy efficient and unlikely to compete with the existing post-combustion capture methods^{8,9}. Post-combustion capture methods include the capture of release carbon dioxide at the source by treating the flue gas with a capturing agent.

Below figure was designed to promote CO₂-capture and underground storage which may not be the ideal long term solution. Nevertheless, scientists are working on various approaches to address the issue of capturing carbon dioxide which is the key step for further conversion.



Figure 5. A campaign poster designed to promote CO₂ capture and underground storage.

Industrial-scale CO₂ capture relies on the purging of flue gas through an alkaline solution where it most likely forms a salt^{10,11}. There are several established industrial methods for capturing of carbon dioxide at the origin:

- Benfield process in which CO₂ is treated with K₂CO₃ solution for capturing and then carbonate is regenerated¹².
- Rectisol process which includes the removal of gases like CO₂ and H₂S by using pressurized methanol¹⁰.
- Use of organic amines in capturing of carbon dioxide via covalent bonding of carbon dioxide upon nucleophilic attack which requires high thermal energy inputs for regeneration^{10,13,14}.

Besides these well-established industrial approaches, scientists also tried to address the issue by introducing various materials like porous graphitic materials^{15–18}, microporous polymeric resins^{19–21} and metal organic frameworks (MOFs)^{22–25}. Almost all of these methods exclusively rely on physical adsorption upon thermal activation. The idea of direct electrochemical CO₂ capture exploiting the redox behavior of molecular materials, however, remains largely unexplored.

Some examples of redox active organic molecules reacting with CO₂ can be found in the literature: A 1971 study by Reddy *et al.* found that electrochemically reduced benzaniline reacts at 140 °C with CO₂ to form 1- α -phenyl-phenylglycine²⁶. In 1984, Sasaki *et al.* reported the electrochemical carboxylation of α,β -unsaturated ketones with carbon dioxide²⁷. DuBois and coworkers showed the potential of electroactive CO₂ carriers for capturing CO₂ for space applications^{28,29}. Wrighton and Mizen studied similar quinone structures showing that CO₂ undergoes reductive addition with chemically reduced 9,10-phenanthrenequinone, forming a bicarbonate dianion³⁰. Later Stern *et al.* conducted theoretical calculations on 1,4-benzoquinone structures to support the mechanism proposed by Wrighton and Mizen³¹. Buttry and coworkers combined the use of small organic molecules with electrochemistry for assessing the performance of 4,4'-bipyridine as a CO₂ capturing agent³². The same group also introduced benzylthiolate as a carbon dioxide capturing agent which is generated by electrochemical reduction of benzyldisulfide³³. These studies show the power of electrochemical capture and release of carbon dioxide as an alternative to energy and cost-intensive established capturing agent. Another important point to address is the physical status of the electrochemical capturing agent. Up to now all reported literature is about small organic molecules which are in solution. This adds another toll to the energy and cost since the regeneration of the capturing agent requires shifting of whole solvent-capturing agent mixture. Heterogeneous electrodes which CO₂ can be loaded onto are still missing in the field. Such electrodes might eliminate the necessity of shifting whole electrolyte mixture for further releasing of CO₂. Instead just the electrodes can be mobilized to the desired area where CO₂ can be released.

1.3. Hydrogen Peroxide as Alternative Chemical Energy Storage Medium

Reduction of dissolved oxygen in water, also known as oxygen reduction reaction (ORR), leads to formation of H_2O_2 which is a high-energy and versatile product³⁴. H_2O_2 is capable of participating in several different redox reactions and is an active species in plethora of biological processes¹⁰. In addition H_2O_2 has been used as a propellant throughout history starting with the Second World War. The fuel grade H_2O_2 is called High-Test Peroxide (HTP) which is a hydrogen peroxide solution consists of typically 85-98% hydrogen peroxide. When in contact with a catalyst (e.g. metallic silver, permanganates of alkali metals, and manganese oxides like manganese dioxide (MnO_2) and dimanganese trioxide (Mn_2O_3)) HTP decomposes into high temperature mixture of O_2 and steam without remaining liquid water. This reaction has been exploited as rocket propellant, torpedo propellant and in some cases as fuel for Vernier engines which are small booster rockets that are used for adjusting the altitude and velocity of spacecrafts³⁵⁻³⁷. Since the industrial process for the formation of H_2O_2 which uses anthraquinone process, is known to be energy intensive due to involvement of high temperatures, high-pressure hydrogenation and noble metal catalysts³⁸. Researchers have been extensively studying since the reaction also takes place, although not so favorable, in fuel cells. Efforts to make production of H_2O_2 production less energy-intensive are underway³⁹.

Oxygen reduction reaction can take place in several ways which are listed in the table below⁴⁰:

Table 1. Thermodynamic potentials of electrochemical O_2 reduction reactions

Electrolyte medium	ORR reactions	Thermodynamic electrode potential in Volt (at standard conditions)
Acidic	$O_2 + 4H^+ + 4e^- \rightarrow H_2O$	1.23
	$O_2 + 2H^+ + 2e^- \rightarrow H_2O_2$	0.70
	$H_2O_2 + 2H^+ + 2e^- \rightarrow 2H_2O$	1.76
Alkaline	$O_2 + H_2O + 4e^- \rightarrow 4OH^-$	0.40
	$O_2 + H_2O + 2e^- \rightarrow HO_2^- + OH^-$	-0.06
	$HO_2^- + H_2O + 2e^- \rightarrow 3OH^-$	0.867
Non-aqueous aprotic solvents	$O_2 + e^- \rightarrow O_2^-$	-*
	$O_2^- + e^- \rightarrow O_2^{2-}$	-*

*: Thermodynamic potentials for 1-electron reduction and superoxide formation are not given in this table since they are strongly dependent on the solvent used.

Hydrogen peroxide is an alternative green oxidant in industry since its only by products are H_2O and O_2 and production of it via solar conversion might be an alternative way energy storage^{34,41-43}.

Dedicated to this quest, researchers have tried to address this issue and tackle the problem by introducing metal catalysts⁴⁴⁻⁴⁹, core-shell structures, metal oxides, metal chalcogenides etc.⁵⁰⁻⁵² Additionally, photocatalytic reduction of O_2 to H_2O_2 by inorganic semiconductors (e.g. ZnO, CdS and TiO_2) and organometallic complexes has been reported^{43,51,53,54}. Recently, metal-free

carbon-based catalysts are in the focus for (photo)electrochemical reduction of dissolved O_2 . This class mainly includes graphitic carbon nitrides ($g-C_3N_4$) and organic pigments⁵⁵⁻⁵⁷. However, almost all of these reactions require either acidic or basic conditions which make daily applications challenging. Although there are a few examples⁵⁸, the search for a catalyst which works under mild pH conditions is still in progress.

1.4. Homogeneous vs. Heterogeneous Catalysis

According to the Gold Book of International Union of Pure and Applied Chemistry (IUPAC) homogeneous catalysis can be defined as the catalytic reaction which takes place where the catalyst and the reactants are in the same phase. In the case of heterogeneous catalysis catalyst and the reactants are in different phases which might be gas-solid, liquid-solid or liquid-liquid. Heterogeneous catalysis takes place in an interface. Almost 90 % of the catalysis taking place in chemical industry is heterogeneous based. Certain examples can be found in the table below⁵⁹:

Table 2. Examples of industrial processes where heterogeneous catalysis is used.

Process	Catalyst used in the process
Sulfuric acid synthesis	Vanadium oxides
Haber-Bosch process (ammonia synthesis)	Iron oxides on Al_2O_3
Ostwald process (Nitric acid synthesis)	Unsupported Pt-Rh gauze
Hydrogen production via steam reforming	Nickel or K_2O
Andrussov oxidation (Hydrogen cyanide synthesis)	Pt-Rh
Ziegler-Natta polymerization of olefins	$TiCl_3$ on $MgCl_2$
Ethylene oxide synthesis	Ag on Al_2O_3
Hydrodesulfurization	Mo-Co on Al_2O_3

Homogeneous and heterogeneous approaches have both advantages and disadvantages which are listed below⁶⁰⁻⁶³:

Table 3. Comparison of Homogeneous and Heterogeneous Catalysis

Features of Homogeneous Catalysis	Features of Heterogeneous Catalysis
Industrially less relevant	High industrial relevance
Mild reaction conditions ($-78^\circ C$ to $250^\circ C$)	Wide range of operating conditions
Ease of investigation of mechanism and reaction conditions directly in solution (NMR, IR, UV-Vis etc.)	Requires specialized analytic methods (operando methods, ATR-FTIR)
Fine-tuning of the catalyst properties is easy	Fine-tuning is not always easy
High selectivity and high diffusivity	High selectivity is not always possible
Well defined-active site	Poorly defined active site
Catalyst separation and recycling is expensive and energy intensive	Catalyst separation and recycling is simple and easy.

1.4.1. Organic Semiconductors

With aforementioned features and many others in mind this thesis aims to use the properties of both catalysis and make a synthesis of both. Organic semiconductors are solids which bare π -bonded molecules or polymers in their structure which made up by carbon and hydrogen mainly. These structures can also contain heteroatoms like nitrogen, oxygen and sulfur. In their neutral states they are generally electrical insulators. Upon injection of charges, doping or photoexcitation they become semiconducting.

First known example of organic semiconductors was synthesized by Henry Letheby who was an English analytical chemist and a public health officer in 1862⁶⁴. Later on in 1960, Kallmann and Pope reported that a hole current can flow through an anthracene crystal contacted with a positively biased iodine-containing electrolyte which acted as hole injector^{65,66}. This was the first proof-of-concept that the organic compounds can be semiconductors. Since then organic semiconductors and conjugated polymers were studied extensively⁶⁷⁻⁷⁴. These studies include, but not limited to, Organic Solar Cells (OSCs), Organic Field Effect Transistors (OFETs), Organic Light Emitting Diodes and many others. Interested readers may also refer to many books published on the topic of organic semiconductors and their applications⁷⁵⁻⁸⁰.

In comparison to their inorganic counterparts, organic semiconductors can be modified chemically and their properties like absorption, emission, crystallinity, conductivity, solubility etc. can be tailored. These properties made them suitable for various applications as mentioned above. In addition to well-known device applications, organic semiconductors were also used in photoelectrochemical cells, which constitute an important part of this thesis. Photoelectrochemical cells convert light energy, together with the help of electrical input, into chemical energy^{81,82}. Their interfaces between electrodes and electrolytes have been investigated for different applications but catalytic applications of organic semiconductors remain mostly unexplored.

A semiconductor-electrolyte interface is shown below for a p-type semiconductor.

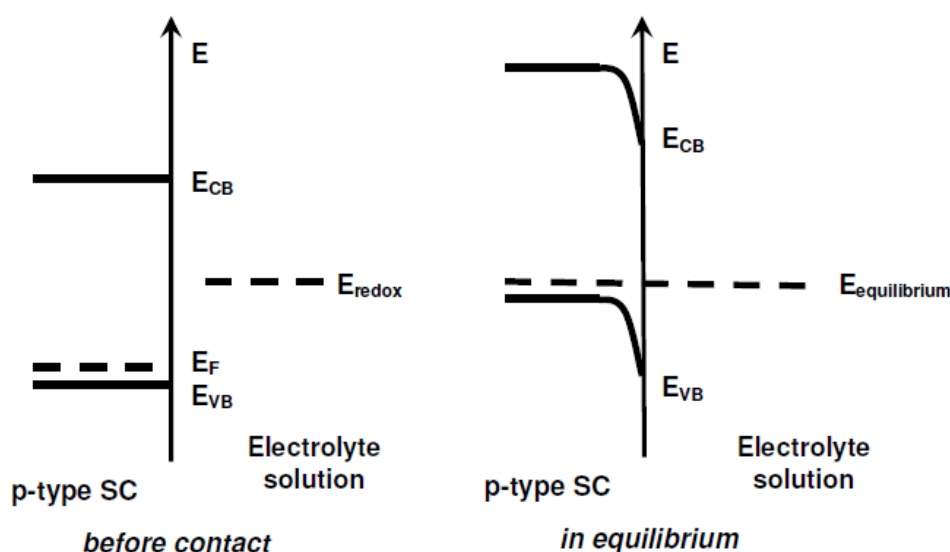


Figure 6. Energy level diagram of a p-type semiconductor-electrolyte interface, before contact and at equilibrium.

E_F in this diagram is the Fermi level, which is defined as the energy level at which the probability of being occupied by an electron is $\frac{1}{2}$. This level lies in the middle of conduction and valence bands in an undoped semiconductor. Upon doping the Fermi level changes due to the change of the distribution of electrons in the semiconductor. For a p-type semiconductor Fermi level lies just above the valence band whereas it is located right below the conduction band in case of an n-type semiconductor. When a semiconductor electrode dipped into an electrolyte solution the abovementioned picture is altered. If the redox potential of the electrolyte solution and the Fermi level do not lie at the same energy, charges move between the semiconductor and electrolyte solution in order to equilibrate the two phases. The excess charge now extends into the semiconductor forming *space charge region*. This creates an electric field and one has two double layers to take into account which are interfacial double layer and space charge double layer. In case of a p-type semiconductor, electrons will be transferred from the electrolyte to the electrode since the Fermi level usually lies below redox potential. This creates a negatively-charged *space charge region* causing the band edges to bend downwards. With this, the holes in the space charge region are removed which results in a depletion region. The process is reversed for n-type semiconductors^{83,84}.

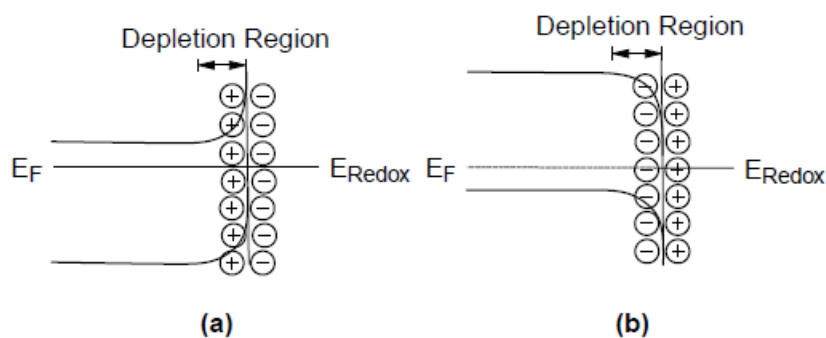


Figure 7. Schematic representation of band bending at electrode-electrolyte interface in semiconductors. (a) n-type and (b) p-type.

As the semiconductor is usually situated on a metal electrode the change in the potential of the electrode will have an effect. The behavior of the bulk of the semiconductor (*i.e.*, away from the depletion region) varies with the applied potential and this is translated from the bulk of the semiconductor to the interface which opens up three possibilities:

- At potentials where the Fermi energy level lies at the same energy level as the redox potential of the solution there is no net charge transfer. This results in no bending of the bands which is called *flatband potential*, E_{fb} .
- Depletion regions arise at potentials more negative of the flatband potentials for p-type semiconductors and at more positive potentials for n-type semiconductors.
- At potential positive of the flatband potential an excess of majority carriers (holes) is observed in this space charge region which is now referred to as *accumulation region*. This true for more negative potentials of the flatband potential in n-type semiconductors.

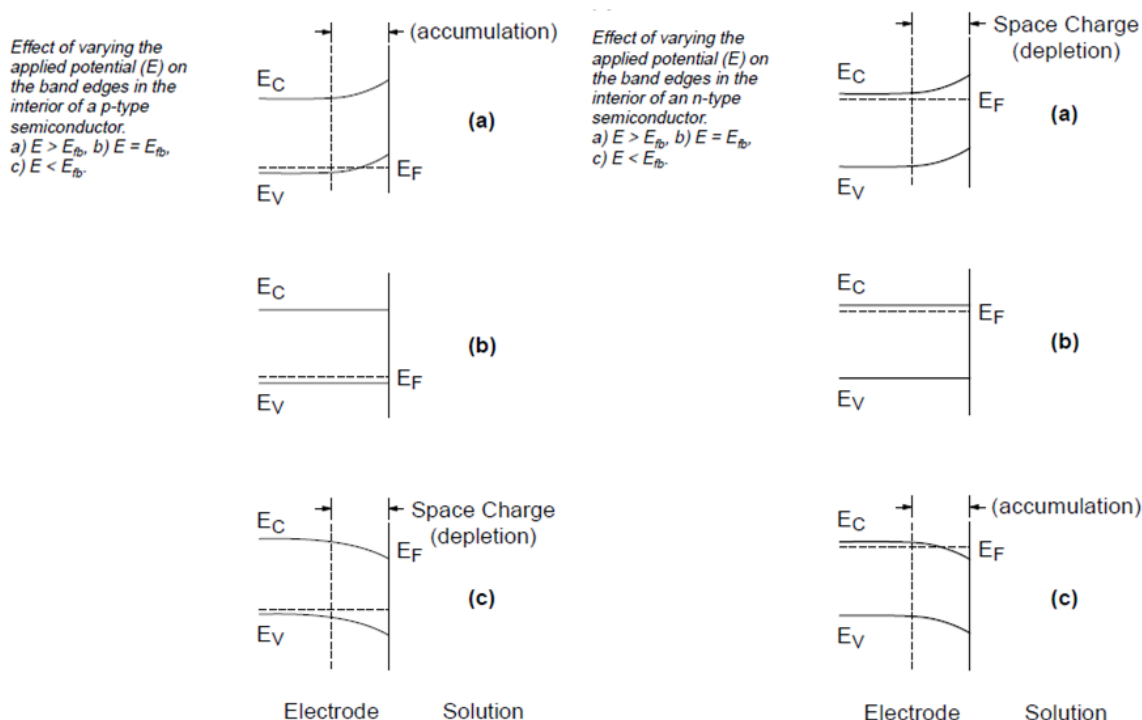


Figure 8. Effect of applied potential on the band edges of the bulk of the semiconductor.

This thesis aims to implement the abovementioned logic for well-known organic semiconductors like polythiophenes and porphyrins via modifying them chemically to be immobilized on the surface of an electrode in order to drive catalytic reactions like carbon dioxide reduction and oxygen reduction.

1.4.2. Electrochemical and Photoelectrochemical Reduction of Carbon Dioxide

1.4.2.1. Homogeneous Approaches

There are many types of catalysts that have been investigated for the reduction of carbon dioxide to further products and among them organometallic complexes, especially polypyridine, are of main interest⁸⁵. Rhenium containing pyridine complexes are probably the most studied class of materials in the field of CO₂ reduction.

The first of the Re-containing complexes was reported by Hawecker, Lehn and Zissel in 1984⁶⁰. In their paper, the authors describe their findings on [Re(bpy)(CO)₃Cl] (bpy=2,2'-bipyridine), which had been introduced as a homogeneous photocatalyst by the same group previously for the electrochemical reduction of carbon dioxide to carbon monoxide⁸⁶. Hawecker et al. showed that [Re(bpy)(CO)₃Cl] (also known as Lehn's catalyst) can produce 32 mL of CO if held at a potential of -1250 mV (vs. NHE) for 14 h without degradation, giving a remarkable faradaic efficiency of 98% and a TON of 300. The authors note that the complex gives the highest efficiency if a mixture of DMF/H₂O (9:1) is used together with 0.1m Et₄NCl as the supporting electrolyte. If no water was added, CO production was observed to be much slower, leveling off after a few hours. This study was a milestone which inspired many subsequent ones in the field.

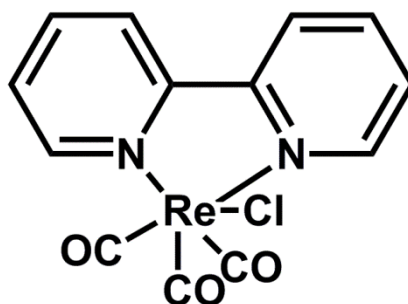


Figure 9. Chemical structure of $\text{Re}(\text{bpy})(\text{CO})_3\text{Cl}$ where bpy is 2,2'-bipyridine.

Although the study of Hawecker and co-workers set a milestone in the field, in the initial paper, the mechanism behind the process was not elaborated in detail. However, the study did have an important comparative experimental aspect in which electrolyte solutions with and without water were used. This was an important hint for the subsequent studies. Sullivan *et al.*⁸⁷ performed a detailed study on the $[\text{Re}(\text{bpy})(\text{CO})_3\text{Cl}]$ complex to clarify the mechanism. Their report describes the electrochemical behavior of the complex as well as the related derivatives, which led the authors toward two independent pathways for the electrochemical reduction of carbon dioxide. The derivatives used in the study were represented with the general formula $[\text{Re}(\text{bpy})(\text{CO})_3\text{L}]^{n+}$, where L =4-ethylpyridine ($n=1$), Cl^- ($n=0$) or hydride ($n=0$). The authors showed that the variation of the ligand did not affect the redox potential of the first reversible reduction peak, which was observed at approximately -1120 mV (vs. NHE), and concluded that this peak originates from the reduction of bipyridine (bpy). The second (irreversible) reduction peak potential varied with the changing ligands L suggesting that this process is metal based. Coulometry and bulk electrolysis at -1100 to -1200 mV (vs. NHE) demonstrated that the first reduction is a one-electron process. However, this process is coupled to the formation of the sparingly soluble green dimer $[\text{Re}(\text{bpy})(\text{CO})_3]_2$. The authors characterized this dimer by UV/Vis, IR and ^1H NMR spectroscopy as well as elemental analysis. They also produced this dimer by chemical synthesis to further support their spectroscopic conclusions. The mechanism for the formation of the Re–Re dimer proposed by Sullivan *et al.* can be summarized as follows:

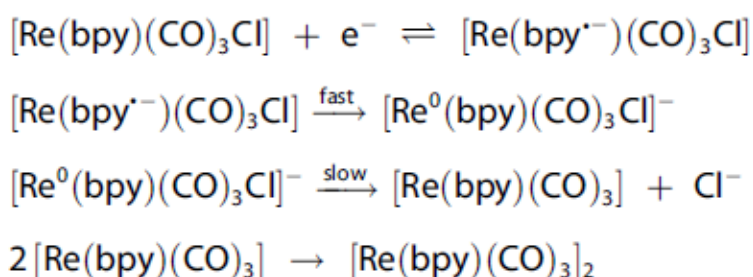


Figure 10. Set of equations leading to the formation of sparingly-soluble dimer.

The lack of redox activity, indicating the formation of dimer species in the cyclic voltammogram of the complex, was explained by the slow rate of the process. The authors suggest that loss of Cl^- might be preceded by intramolecular electron transfer to a metal-based $d\sigma^*$ orbital, which, as a result, might facilitate metal–metal bond formation. The authors conducted a constant-potential experiment at -1500 mV (vs. NHE), which consumed two electrons per Re atom to give a red-purple solution. This is believed to be the anionic form ($[\text{Re}(\text{bpy})(\text{CO})_3]^-$) of the complex. If CO_2

was introduced into the electrolyte the first reversible peak at -1120 mV did not show a catalytic enhancement, suggesting that bpy does not take part in the catalytic reduction of carbon dioxide if a current enhancement in the second reduction peak of the complex is observed. Finally the authors' findings were summarized in a two-way reaction scheme and it is stated that the process starts with a radical form of $[\text{Re}(\text{bpy})(\text{CO})_3]$ or its solvated form $[\text{Re}(\text{bpy})(\text{CO})_3]\cdot\text{MeCN}$. It is concluded that the dimer formation occurs when CO_2 is not present in the vicinity of the electrode. The second path (two-electron pathway) involves the anion $[\text{Re}(\text{bpy})(\text{CO})_3]^-$ and results in the formation of CO ⁸⁸.

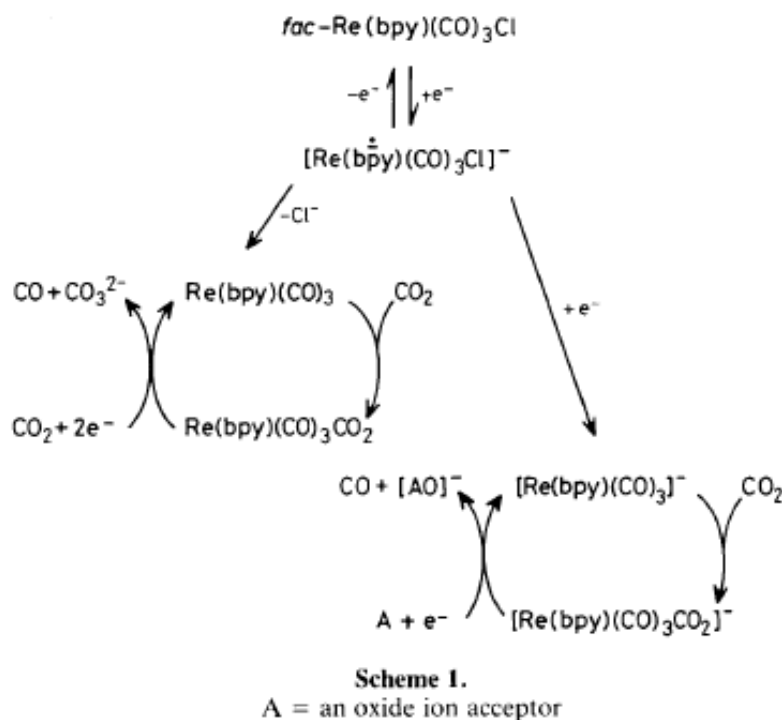


Figure 11. Reaction pathways suggested by Sullivan *et al.*⁸⁷

Detailed information on the further studies of Re containing complexes and their catalytic performances can be found in this review⁸⁹.

1.4.2.2. Heterogeneous Approaches

Scientists tried to address the issue of side reactions and dimer formation with various approaches where they tried to immobilize the catalyst on the electrode surface. Another important issue regarding the Re-complex-driven CO_2 electrocatalysis is the high potential values required⁹⁰⁻⁹⁴ for the reduction which makes the process energy inefficient. One way to address this issue is the use of light energy as an addition to the electrochemical reduction. This should not be confused by the photocatalytic reduction of CO_2 which can be found in detail in these reviews⁹⁵⁻⁹⁸.

Photoelectrocatalytic reduction of CO_2 offers lower energy requirements since the energy needed to reduce carbon dioxide is partially supplied by the light source. In the literature there are several examples for photoelectrochemical reduction of carbon dioxide where semiconductors and/or semiconductors modified with catalysts were utilized⁸⁸.

One of the earliest examples of photoelectrochemical reduction of CO₂ was introduced by Hallmann in 1978 where he used a p-type gallium phosphide (GaP) as the working electrode for CO₂ reduction⁹⁹. He obtained formic acid, formaldehyde and methanol as products. Another study where GaP was used followed this one and reported formic acid with a 15.2 % faradaic efficiency¹⁰⁰. Canfield and Frese reported the use of p-type GaAs and InP for catalytic reduction of carbon dioxide to methanol with faradaic efficiencies ranging between 52 – 80%¹⁰¹. Bocarsly and co-workers used GaP as the photoelectrode where they addressed pyridinium ion in solution to produce methanol from carbon dioxide¹⁰². Other examples where semiconductors were used to drive the catalytic reduction of carbon dioxide can be found in literature^{88,103–106}.

Another approach is the covalent attachment of a catalytically active material on the electrode surface. Possibly the earliest example in the literature is the study reported by Spiro and Ghosh in 1980 where authors covalently immobilized [Ru(bpy)₃]²⁺ on n-type SnO₂¹⁰⁷. The study did not investigate the catalytic properties of the electrode but this was an important demonstration of covalent attachment of such molecules. Reisner and co-workers attached [Re{2,2'-bipyridine-4,4'-bis(phosphonic acid)}(CO)₃(L)] (L=3-picoline or bromide) onto TiO₂ nanoparticles and investigated the catalytic properties and reached a TON of 48 for the formation of CO¹⁰⁸. This study followed by a similar approach by the same group where they immobilized MnP on TiO₂ and drove the photoelectrochemical reduction of carbon dioxide with a faradaic efficiency of 62%¹⁰⁹.

Studies in which well-known Re bipyridine complex is immobilized are not too many in the literature. The earliest example was introduced by Meyer *et al.* in which the authors used Re containing 4-vinyl-4'-methyl-2,2'-bipyridine in polymer backbone. The polymer was grown electrochemically from Re complex and yielded CO as the main product with a faradaic efficiency of ~90% in CO₂-saturated solutions¹¹⁰. Cosnier and co-workers attached Lehn's catalyst as a pendant group onto a pyrrole molecule and electropolymerized it to yield a polymer with polypyrrole backbone where Lehn's catalyst as the pendant group¹¹¹. The polymer gave oxalate and CO as products and reached a faradaic efficiency of 78% but the catalytic activity decreased rapidly with time. Portenkirchner and coworkers introduced an n-type polymer where they incorporated Lehn's catalyst into the backbone and investigated its catalytic properties. The polymer reached faradaic efficiencies around ~30% with CO being the main product¹¹².

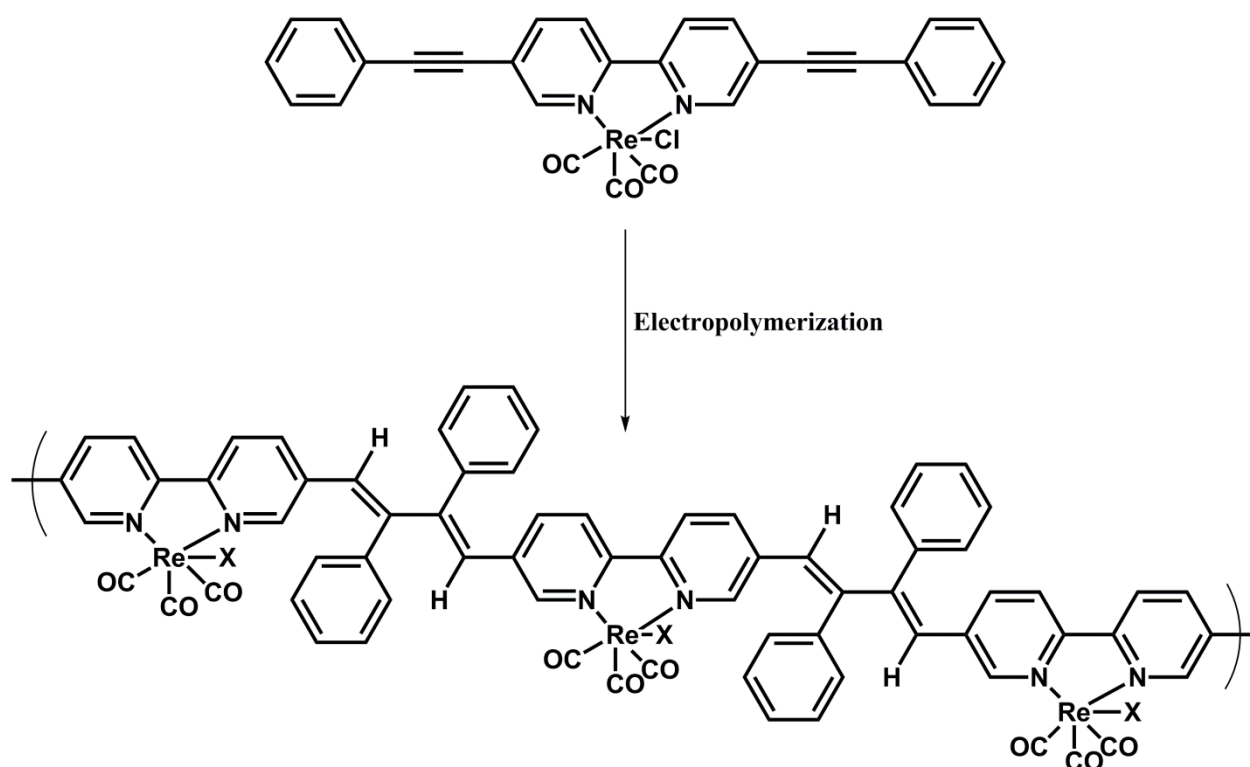


Figure 12. Potentiodynamic formation of Lehn catalyst bearing polymer.

Later on Nervi and coworkers also introduced polymer structures with thiophene having Lehn's catalyst as the pendant group which yielded a faradaic yield of 84% at -2100 mV^{113} .

All these molecules bearing Lehn's catalyst in their structure have a trait in common that is being operated in electrocatalytic mode where high potentials are required. A different route where the combination of electrocatalysis and photocatalysis is combined is still missing which is one of the motivations for photoelectrocatalytic reduction of carbon dioxide using third generation conjugated polymers.

2. Experimental Methods and Materials

2.1. Materials

Materials used throughout this thesis are listed in the table below along with their suppliers.

Material	Formula	Supplier	Purity	Abbreviation
Acetone	C ₃ H ₆ O	VWR Chemicals	technical	-
Acetonitrile	C ₂ H ₃ N	Roth	> 99.9%	MeCN
Carbon dioxide	CO ₂	Linde	99.995%	-
Chlorobenzene	C ₆ H ₅ Cl	VWR Chemicals	100%	-
Chromium on tungsten rod	Cr	Kurt J. Lesker	99.9%	-
Copper sulphate pentahydrate	CuSO ₄ * 5 H ₂ O	Sigma Aldrich	p.a. >99.0%	-
<i>N,N</i> -dimethylformamide	C ₃ H ₇ NO	VWR Chemicals	100%	DMF
Glass		Thermo Scientific	Pre-cleaned	-
Glassy Carbon, 2 mm		Alfa Aesar	type 1	GC
Gold	Au	Ögussa	99.99%	-
Hydrochloric acid	HCl	Sigma-Aldrich	37.5%	HCl
Isopropanol	C ₃ H ₈ O	VWR Chemicals	AnalaR Normapur	IPA
Nitrogen	N ₂	JKU		-
Pyridine	C ₅ H ₅ N	Sigma Aldrich	99.8%	Pyr
Quinacridone	C ₂₀ H ₁₂ N ₂ O ₂	TCI	> 93.0%	QNC
Silver wire	Ag	Alfa Aesar	99.99%	Ag
Sodium chloride	NaCl	ACM	99.98%	-
Sodium sulphate anhydrous	Na ₂ SO ₄	Sigma Aldrich	> 99.0%	-
Sulfuric acid	H ₂ SO ₄	J. T Baker	95 - 97%	-
Tetrabutylammonium hexafluorophosphate	C ₁₆ H ₃₆ NPF ₆	Sigma Aldrich	>99.0%	TBAPF ₆

2.2. Methods

2.2.1. Electrochemistry

Cyclic voltammetry was used extensively for characterization and catalysis throughout this thesis and the basics will be explained briefly in this part.

Cyclic voltammetry is a useful method which involves the imposing of a triangular waveform which is created by a potentiostat, as the potential of the working electrode in an electrochemical cell. The electrochemical cell usually includes a three-electrode configuration with a working electrode (WE), a counter electrode (CE) and a reference electrode (RE).

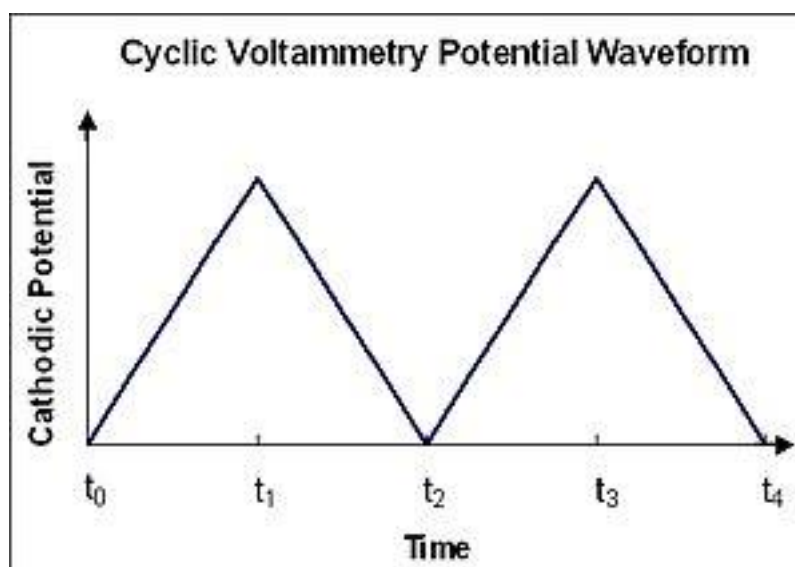


Figure 13. Potential waveform in cyclic voltammetry.

A potential is applied by the function generator to the WE against the RE which maintains a constant potential. This potential is maintained at the desired value by a potential difference applied between WE and CE. The current also flows between WE and CE while RE carries no current in order to protect its integrity and to keep its potential constant⁴⁰.

Various different electrochemical cells were utilized during this study. Initial characterization of the compounds of interest was done in a one-compartment cell where all the electrodes were in the same compartment for the sake of simplicity. For constant potential electrolysis experiments a two-compartment cell was used in order to prevent the re-oxidation of the newly-formed products on the anode and cross contamination which might arise from the reactions at the CE.

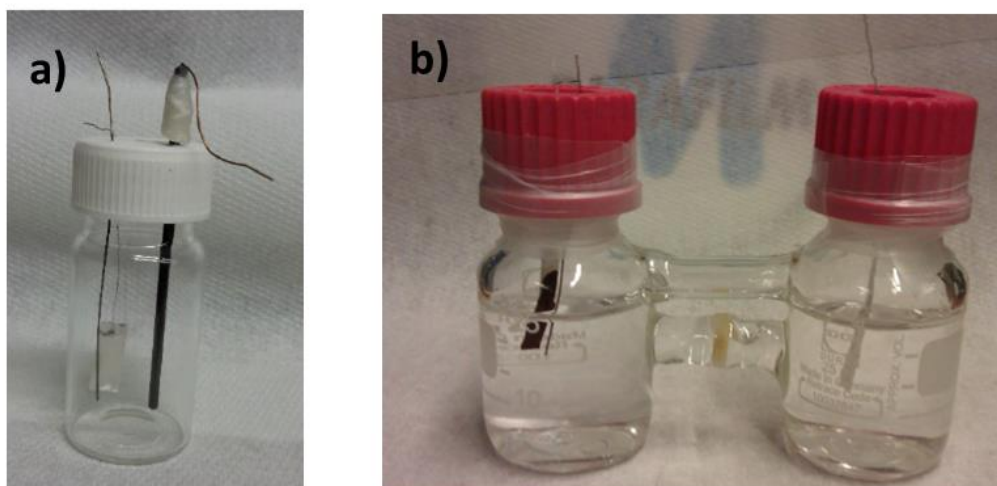


Figure 14. Photos of a one-compartment cell (a) and a two-compartment cell (b).

When organic solvents were used as the solvent, the supporting electrolyte of choice was 0.1 M tetrabutylammonium hexafluorophosphate (TBAPF₆) in the the corresponding organic solvent. A silver wire coated with silver chloride¹¹⁴ was used as the quasi-reference in all cases where the electrolyte solution was of organic origin. This electrode is then calibrated externally against ferrocene / ferrocenium (Fc / Fc⁺) couple. Ferrocene was chosen because of its stability and distinct one-electron redox property.

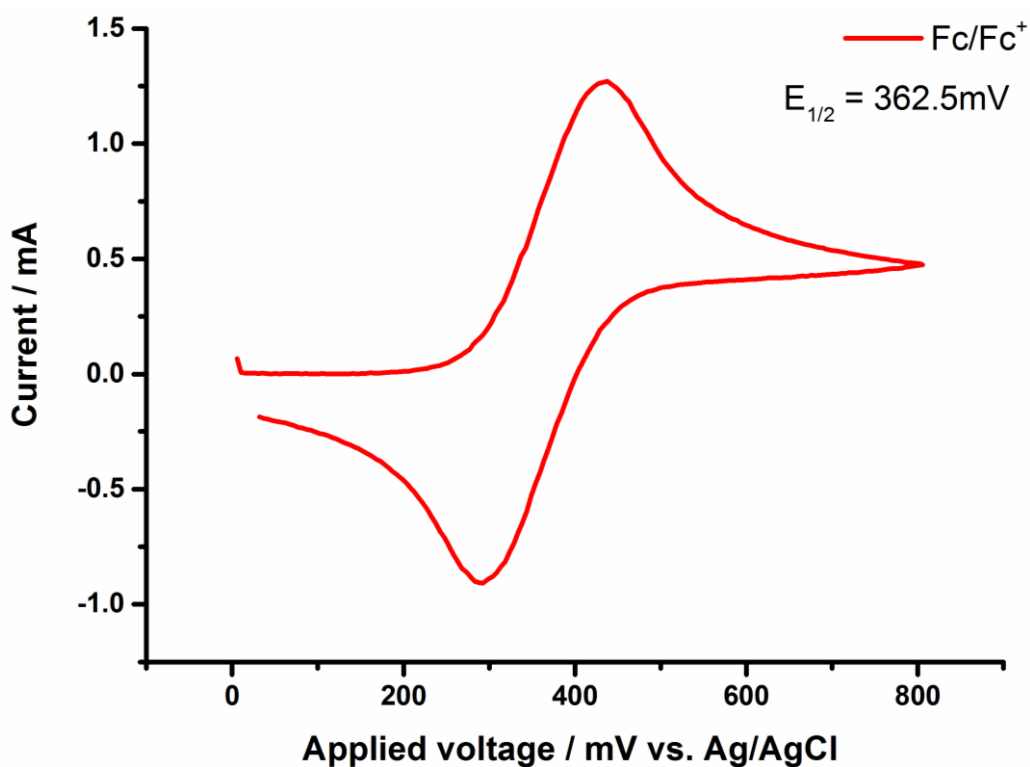
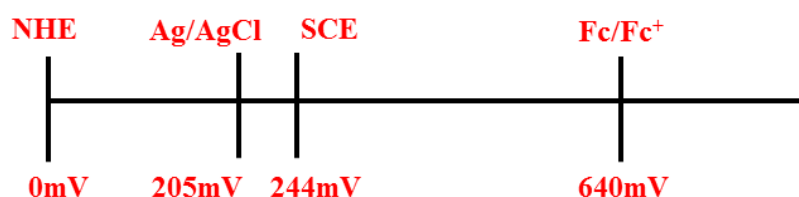


Figure 15. Typical cyclic voltammogram of Ferrocene / Ferrocenium couple.

Figure above shows a typical voltammogram of Fc / Fc⁺ couple in 0.1 M TBAPF₆ in acetonitrile. The half-wave potential is deduced from the cyclic voltammogram and then converted to normal hydrogen electrode (NHE) values by taking the E_{1/2, ferrocene} as 640 mV.

In the case of aqueous solvents 0.1 M sodium sulfate (Na₂SO₄) in water was used as the electrolyte.

A conversion of the electrode potentials that are used throughout this thesis to each other is given below.



For photoelectrochemical experiments a halogen lamp was used at a certain distance to maintain the same intensity for each experiment which is 60 mW cm⁻². This value was obtained by measuring the intensity of the incoming light intensity in the vicinity of the electrochemical cell using a calibrated Si diode.



Figure 16. Photo of a photoelectrochemical experiment in progress.

The electrochemical cell was cooled with a pair of small fans or a big home-type fan during the experiments to avoid the heating effect which might originate from the halogen lamp.

Except in the case of O₂ reduction experiments, all other experiments started with purging the electrochemical cell extensively with N₂ or Ar to remove the atmospheric oxygen. Since all experiments in this thesis deals with the reductive part of the voltammogram, atmospheric oxygen is an important contaminant. It may cause oxidation of the reduced species or itself can be reduced causing interference in the electrochemical behavior of the compound of interest. The time of purging varied depending on the nature of the electrolyte. Aqueous based electrolytes require more than 60 min of purging in order to sufficiently get rid of atmospheric oxygen since the solubility of oxygen in water is 8 mg/L. In organic solvents this time can be reduced to 15 – 30 minutes for N₂ or Ar. In the case of CO₂ purging aqueous solvents need again more than 60 min while for organic solvents like acetonitrile 10 minutes is enough since the solubility of CO₂ is 34 times higher in acetonitrile than that is in water. That is also true for O₂ in aqueous electrolytes as it was mentioned earlier.

Upon completion of the initial characterization of the interested compounds a constant potential electrolysis (CPE) was conducted to assess the performance of the material as a catalyst. For this the electrochemical cell was sealed with air-tight caps having a septum in the middle. Then the cell was purged either with CO₂ or with O₂ around 15 minutes to achieve saturation. In all constant potential electrolysis cases the electrolyte solution was stirred during electrolysis. The potential that was kept constant was decided upon the behavior of the compound in cyclic voltammetry under CO₂.

When CPE was concluded a gas-tight glass syringe was used to penetrate the septum of the cathode compartment to sample the headspace. A sample of 2 mL gas was taken and then injected to gas chromatograph (GC) or in the gas sampling chamber of Fourier transform infrared spectrophotometer (FTIR). In the case of ORR experiments an aliquout of 100 µL were taken from the electrochemical cell and were mixed with the detection medium containing the precursor.

During CPE the current-time curve was observed and recorded in order to extract the amount of charges that were used in the process. A current-time curve is plotted with the units Ampere and seconds and then the area under the curve is integrated to obtain the charge passed in Coulomb.

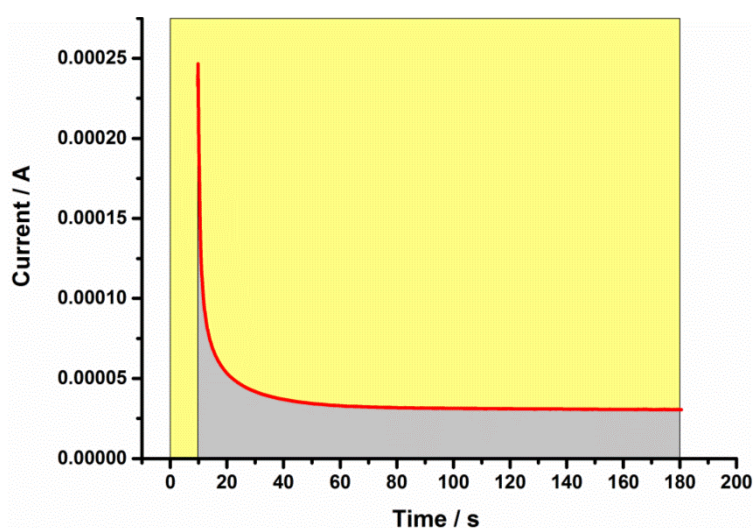


Figure 17. A typical current-time curve used for extracting the charges consumed during electrolysis.

Extracting the number of charges used during CPE is important for the calculation of faradaic efficiency which defines the selectivity of a catalyst toward a certain product. The faradaic efficiency can be calculated by the dividing the number of moles of product obtained by the number of moles of electrons consumed. This is then multiplied by the number of electrons needed to convert the substrate (CO₂ or O₂).

$$\eta = \frac{\# \text{ moles of product}}{\# \text{ of moles of electrons}} \times \# \text{ electrons needed for conversion}$$

Other important parameters for assessing the performance of a catalyst are overpotential which can be described as the difference between the applied potential and the thermodynamic potential that is needed to drive the mentioned process, and turnover number (TON). Turnover number tells us the stability of a catalyst over time and can be calculated as:

$$TON = \frac{\# \text{ moles of product}}{\# \text{ catalytically active sites (or moles of catalyst)}}$$

Calculating the number of catalytically active sites is not always trivial. For that reason scientists use the number of molecules of catalyst in the solution or on the electrode and assume that all of the catalyst in there is active. However, when a catalyst is formed by electropolymerization *i.e.* third-generation conjugated polymers it is not easy to understand how many moles of catalyst is deposited on the electrode. To overcome this issue one can use electrochemistry and calculate the amount of electrochemically active sites on the electrode from the cyclic voltammogram^{115,116}.

This can be done by extracting the charges during one CV cycle and calculating the mole of electrons using Faraday constant.

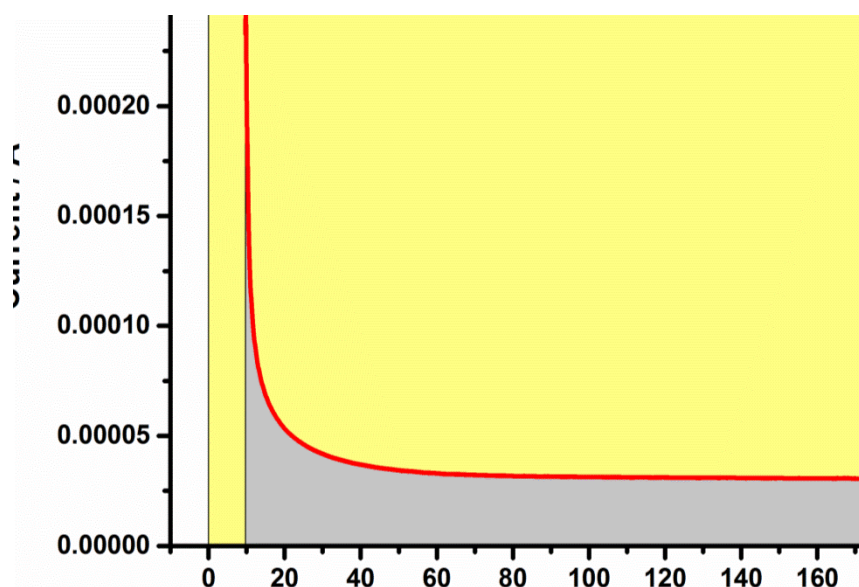


Figure 18. Current-time curve used for calculating the number of active molecules on an electrode.

2.2.2. Fourier Transform Infrared Spectroscopy

FTIR measurements constitute an important portion of characterization and product identification in this thesis. Each gaseous product which was detected using gas chromatography was double checked using FTIR spectroscopy for their chemical structure.

FTIR measurements were performed on Bruker IFS 66/S and Bruker Vertex 80 spectrophotometers with 4 cm^{-1} resolution in each case. The general schematics of an FTIR spectrophotometer are depicted below.

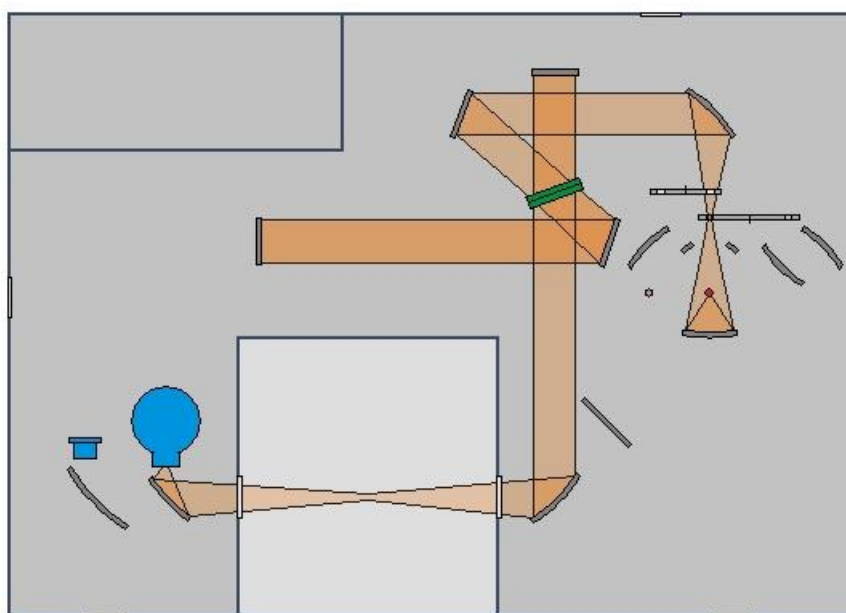


Figure 19. Schematics of an IR spectrophotometer.

The setup consists of Globar (IR source), a Michelson Interferometer with a KBr beam splitter, the sample compartment and a Mercury Cadmium Telluride (MCT) detector.

For the FTIR measurement of gaseous samples a self-made transmission mode gas cell equipped with IR-transparent ZnSe windows and two air tight septa for purging the cell and injecting the sample.

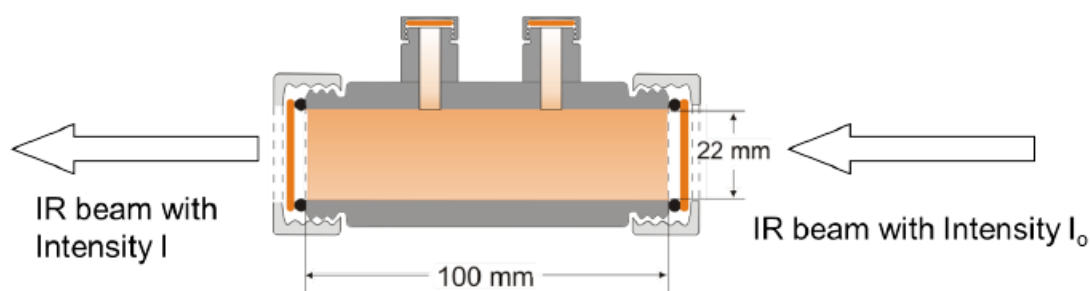


Figure 20. Schematic of the IR transmission cell.

For FTIR measurements a 2 mL-sample was taken from the headspace of the electrochemical cell and was injected to the sample compartment. A measurement where there is no sample was also conducted as the baseline measurement to remove any effects which might originate from the chamber itself.

For quantification of the interested gas sample, a calibration curve was established by injecting a known amount of gas. Later on the area under the related peak in the IR spectrum was plotted against the concentration to obtain a straight line.

Figure below shows a typical difference spectrum for CO₂ and carbon monoxide (CO). Difference spectrum was used throughout this thesis and it is very helpful in order to see small changes. The idea behind the different spectrum is the relative change where the transmission change (ΔT) is divided by the initial transmission which results in peaks pointing downward. To make the spectrum more trivial we add a minus sign in front of it to make the absorbing peaks upwards yielding a $(-\Delta T / T)$ vs. wavenumber plot. In this plot the peaks pointing upwards are newly developing peaks while the peaks pointing downward are diminishing ones.

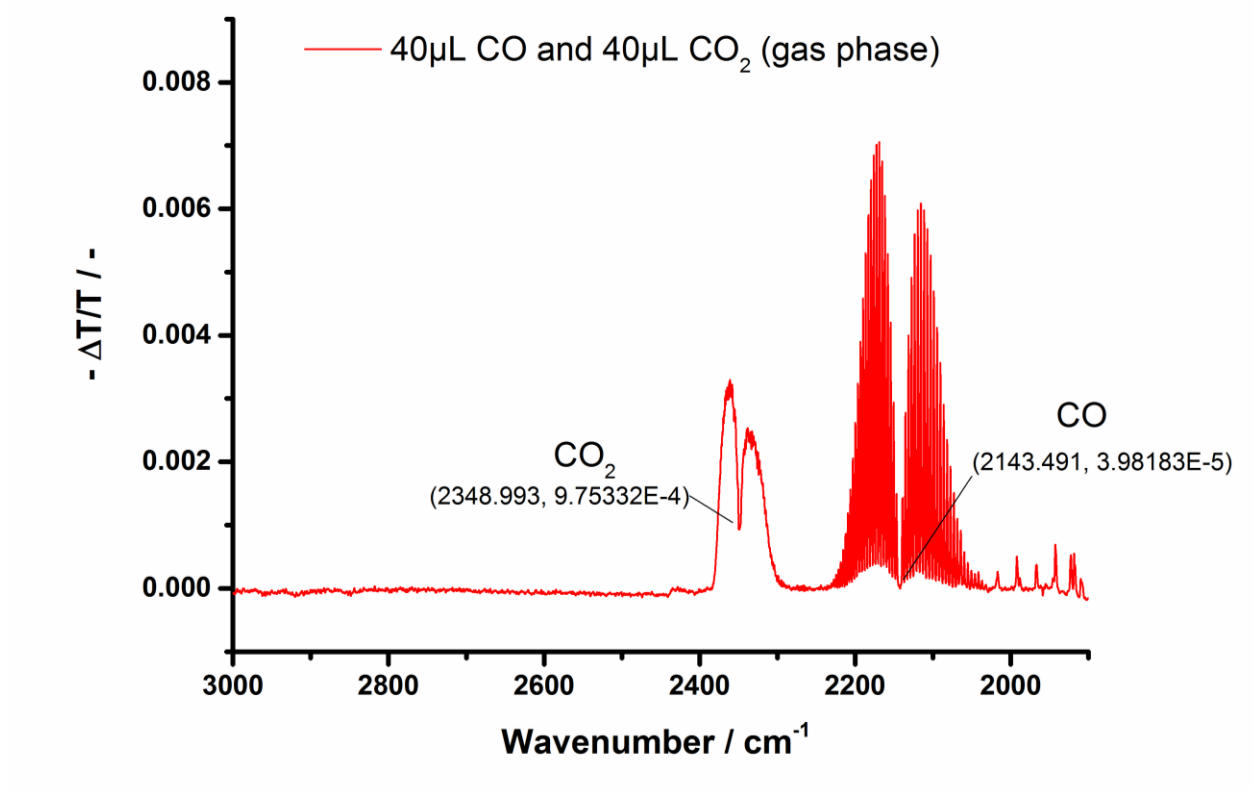


Figure 21. FTIR spectrum of CO₂ and CO.

As it can be seen from the figure there are two double peaks; one centering at 2143 cm^{-1} which corresponds to the infrared active rotational-vibrations of the P and R branches of gas-phase CO. The second one centering at 2348 cm^{-1} corresponds to the infrared active vibration of CO₂. Interested readers are suggested to refer to the work of Harris and Bertolucci for further IR active compounds¹¹⁷.

For FTIR characterization of thin films a Bruker Vertex 80 equipped with a Platinum ATR module was used. In this configuration an electrode with a thin film on it is placed facing downwards on the module where it becomes in contact with the diamond reflection element of the module. The lever is lowered onto the sample to apply pressure in order to remove any trapped air to avoid optical as well as atmospheric interference. This is a reflective mode measurement rather than a transmission mode which allows the characterization of thin films in short time with precision.



Figure 22. Photo of the ATR-FTIR thin film measurement setup. Magnified photo of the actual measurement area (inset).

2.2.2.1. *In-situ* ATR-FTIR Spectroelectrochemistry

In-situ techniques allow us to observe changes inflicted on the electrode during the electrochemical process upon an external stimulus. In this study *in-situ* ATR-FTIR spectroelectrochemistry was used in order to determine the structural changes during electrochemical CO₂ capture process. The experiments were conducted on Bruker IFS 66/s FTIR spectrophotometer equipped with an MCT detector. Prior to the experiments the detector was cooled down to liquid nitrogen temperatures to ensure high sensitivity. The detector, in this state, can be used up to 8-10 hours.

To construct a mini-electrochemical cell a polytetrafluoroethylene (PTFE) housing is used with a Pt-plate in it serving as the counter electrode. A silver wire coated with silver chloride is inserted from the top via a hole to serve as the reference electrode while a Ge crystal coated with material of interest serves as the working electrode. Finally the assembly is completed with an O-ring between the WE and the electrochemical cell. This setup is put into the sample chamber of the FTIR and the PTFE tubes are inserted from above to maintain the electrolyte flow during the experiment. When all is assembled and the electrodes are contacted a paraffin wax sealing is applied around the electrode and tube entry points to ensure atmospheric as well as liquid tightness.

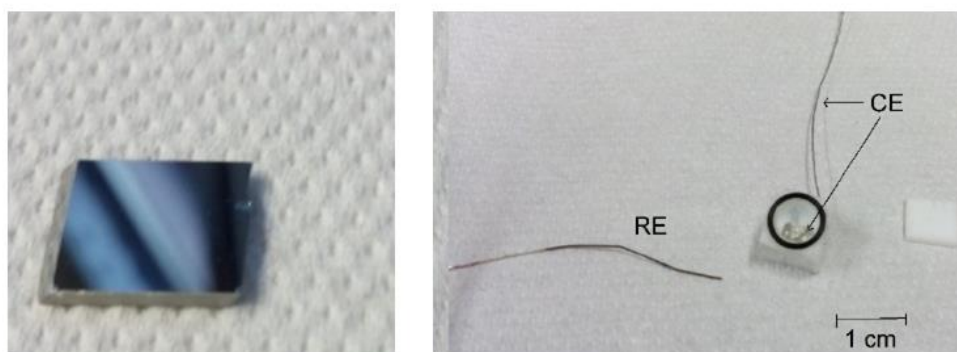


Figure 23. A photo of the Ge reflection element (on the left) and disassembled electrochemical cell (on the right).

A schematic of the top view of the assembled cell is given below.

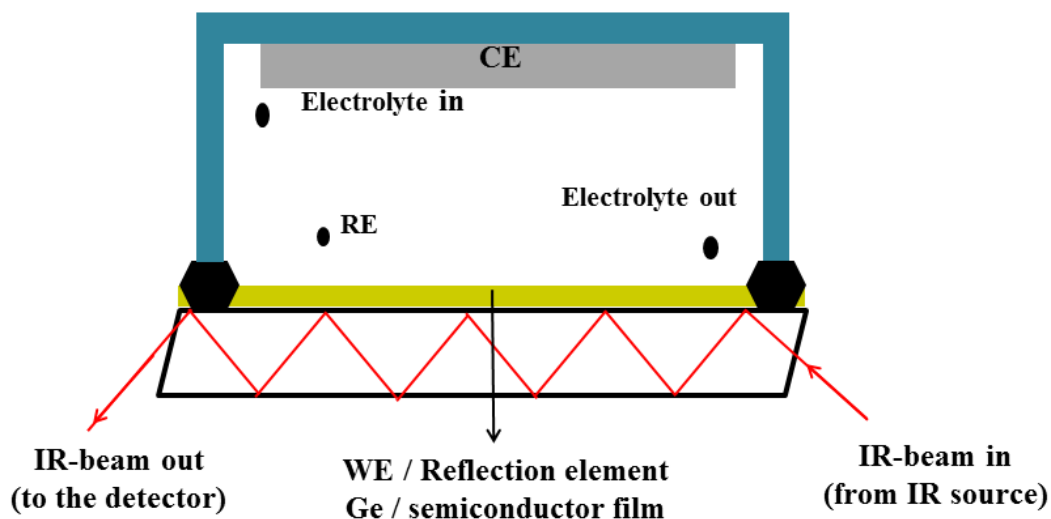


Figure 24. A schematic representation of ATR-FTIR spectroelectrochemistry cell.

After setting up the electrochemical cell inside the sample compartment of the FTIR spectrophotometer the sample compartment is sealed with a plastic foil allowing only the cables for electrodes and tubes for the electrolyte. A step potential program is created in the potentiostat with the desired potential steps. When the electrolyte (organic or aqueous) flow is maintained in a steady flow rate the potential-step measurement is started simultaneously with the collection of spectra in FTIR. Typical example for such an experimental setup is 50 mV potential intervals (applied for 20 seconds) with a measurement of a spectrum every 20

seconds. It is important to note that in case of using Ge electrodes the nature of the applied potential is of essence since oxidative processes tend to degrade the Ge itself. In cases where the reflection element is ZnSe this is not an issue. However, ZnSe is not conductive itself which requires a thin coating (5-7 nm) of Pt layer prior to deposition of material of interest.

Resulting spectra are calculated in the $-\Delta T/T$ configuration and plotted against wavenumber.

2.2.3. UV-Vis Spectroscopy

Uv-Vis absorption measurement of the films and monomers as well as the small molecules was performed in a 1 cm quartz cuvettes at ambient temperatures using a PerkinElmer Lambda 1050 UV-Vis-NIR spectrophotometer. Baseline correction was carried out prior to each set of measurements.

In cases where a fast detection of species is needed, a Thermo Fischer Scientific MultiSkan Go microplate-reading UV-Vis spectrophotometer was used. This allows the detection of multiple species in triplicates or quadruplicates in less than a minute.

2.2.4. Gas Chromatography

For the judgment of a material's ability as a CO₂ catalyst direct product detection is of essence. To this end, a Thermo Fischer Trace GC Ultra gas chromatograph was used. The chromatograph has 2 channels with carrier gases N₂ and He in order to broaden the variety of detectable products. Each channel is also equipped with respective thermal conductivity detector (TCD) which allows the product detection.

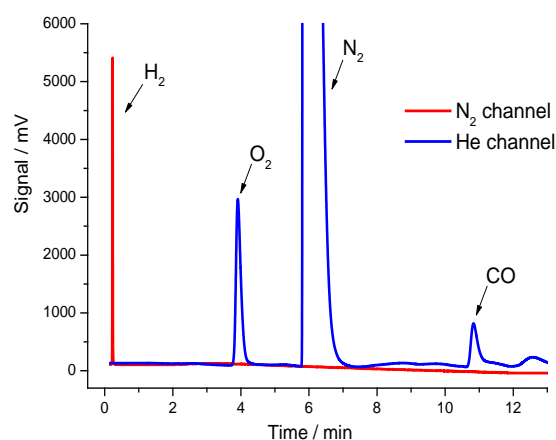


Figure 25. Photo of the Thermo Scientific Trace GC Ultra (on the left) and two typical chromatograms (overlaid) showing the detectable products.

2.2.5. Scanning Electron Microscopy

For the characterization of the electrodes and thin films in nanoscale scanning electron microscopy (SEM) is essential. In the case of O₂ reduction reaction (ORR) electrodes constructed on TiO₂ nanotubes (TiO₂ NTs) a JEOL JSM-6360LV scanning electron microscope was used. Images were taken with a working distance (WD) of 9 mm and an acceleration voltage between 3-15 kV.

2.2.6. Electrode Preparation and Cleaning

Different electrodes were used throughout this study and proper cleaning of electrodes constitutes an important step to reach pristine semiconductor modified electrodes.

Indium Tin Oxide (ITO) coated glass slides were first cut into the desired sizes and then cleaned in different solvent baths ultrasonically. The sequence of cleaning was base-piranha (to smoothen the glass surface), acetone, 2% *Hellmanex* solution, DI water (×2) and isopropanol.

Glassy carbon electrodes were polished both mechanically and electrochemically prior to experiments. For mechanical polishing three different sizes of 1.0 μm, 0.3 μm and 0.05 μm Al₂O₃ powder was used as slurry with the abovementioned order. Each side of the glassy carbon plate was polished 30 s followed by a rinsing with 18 MΩ water. Final polishing was done using a simple white toothpaste since Al₂O₃ particles tend to remain on the surface. Afterwards the electrodes were polished electrochemically by cycling the potential between +1.5 V and -1.5 V with a scan rate of 50 mV s⁻¹ for 30 cycles in 0.5 M H₂SO₄.

TiO₂ NTs electrodes were used as they were delivered from University of Innsbruck. Further cleaning was done by using a *Soxhlet* setup with toluene as the solvent.

Pt counter electrodes were flame cleaned prior to use. In the case of there were residues on the electrodes they were dipped into concentrated nitric acid, rinsed and flame cleaned.

2.2.7. Electrochemical Impedance Spectroscopy

Electrochemical impedance spectroscopy (EIS) is one of the most powerful techniques to understand underlying mechanisms of an electrode's behavior. Resistance in the case of an ideal resistor can be defined as the ability of a certain circuit element to resist the flowing of electrical current. However, most of the systems mentioned here are far from ideal resistor which requires the need of a specialized analysis technique. Impedance can have the same definition as a resistor but in a more general way. Impedance can be referred as the frequency-dependent resistance of a circuit element to current flow. A simple comparison between resistance and impedance can be given as follows:

$$\text{Impedance: } Z\omega = \frac{E\omega}{I\omega}$$

where E_ω is defined as the frequency-dependent potential while I_ω is the frequency-dependent current. Ideal resistor follows Ohm's Law which is defined as:

$$R = \frac{E}{I}$$

EIS is measured by application of a sinusoidal alternating current or voltage to the sample over a range of frequencies¹¹⁸.

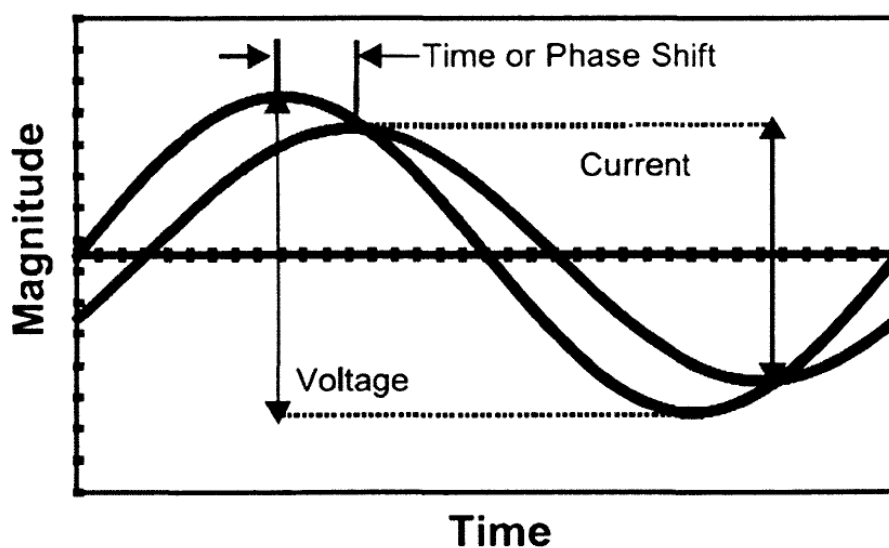


Figure 26. A sinusoidal potential pulse and its current response in an alternating current system.

This excitation signal (voltage) is expressed as a function of time and has the form:

$$E_t = E_0 \sin(j\omega t)$$

where E_t is the potential at time t , E_0 is the amplitude of the signal, and ω is the radial frequency which is dependent on the frequency expressed in Hertz ($\omega = 2\pi f$).

In a linear system, the response signal I_t is shifted in phase and has a different amplitude than I_0 .

$$I_t = I_0 \sin(\omega t + \phi)$$

Finally, an expression analogous to Ohm's Law can be given to calculate the impedance of a system.

$$Z\omega = \frac{E \sin(\omega t)}{I \sin(\omega t + \phi)} = Z\omega \frac{\sin(\omega t)}{\sin(\omega t + \phi)}$$

When E_t is plotted against I_t the resulting shape of the cross-section of these functions is an oval. This oval is known as the Lissajous Figure which was analyzed on oscilloscope screen prior to the modern EIS equipment.

Following the Euler's relationship;

$$\text{Exp}(j\vartheta) = \cos\vartheta + j\sin\vartheta$$

it is possible to express the impedance as a complex function which describes the potential as,

$$E_t = E_0 \exp(j\omega t) \text{ with the current response as } I_t = I_0 \exp(j\omega t - \vartheta)$$

Finally, the impedance is represented as a complex number:

$$Z\omega = \frac{E}{I} = Z_0 \exp(j\vartheta) = Z_0 (\cos\vartheta + j\sin\vartheta)$$

Using EIS may help to:

- Distinguish between two or more electrochemical reaction kinetics,
- Identify diffusion-limited reactions,
- Provide information about the capacitive behavior of an electrode,
- Determine the electron transfer rate of a reaction

EIS results can be reported in two main plots which are Nyquist and Bode plots and they are useful in the making of internal resistance estimates. The Bode plot displays frequency-dependent impedance and phase shift which is useful for estimating the parameters of equivalent circuit model. Very low phase shifts can be associated with resistance e.g. charge transfer resistance, ohmic resistance. The Nyquist plot on the other hand, gives information about ohmic/solution resistance and total resistance in a cell. The type of transport of species like kinetically-controlled or mass transfer controlled transport can also be deduced from Nyquist plot^{119,120}.

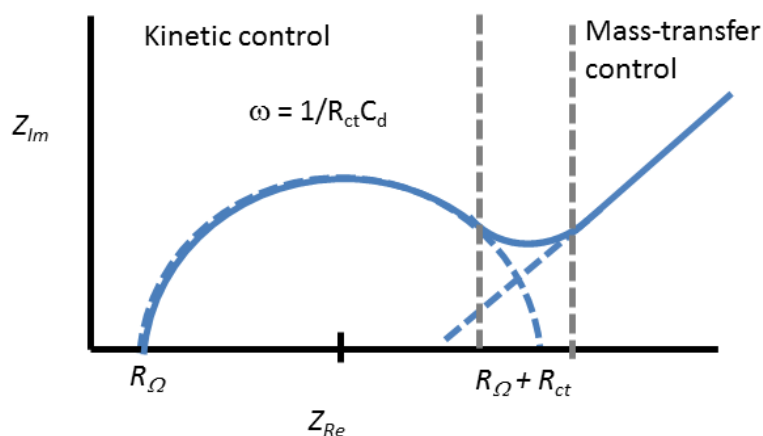


Figure 27. Schematic representation of a typical Nyquist plot.

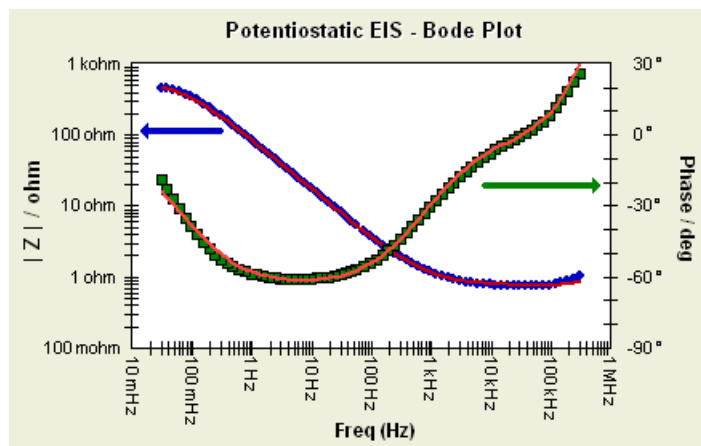


Figure 28. A representative Bode plot (Image taken from Gamry Instruments website).

Upon investigating the EIS properties displayed by the material/electrode an equivalent circuit model is proposed that explains the behavior of the electrode and interfaces thereof in terms of circuit elements.

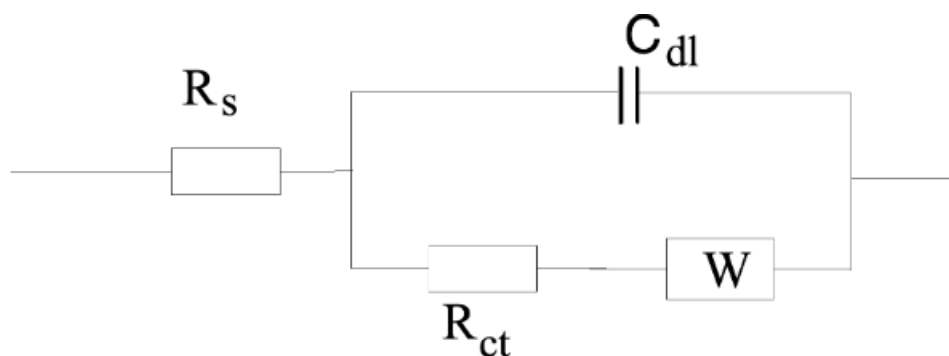


Figure 29. An equivalent circuit model where R_s is the solution resistance, C_{dl} is a double layer capacitor and R_{ct} is charge-transfer resistance (image taken from Gamry Instruments website).

All electrochemical impedance measurements mentioned in this thesis were conducted at University of Innsbruck in collaboration with Dr. Engelbert Portenkirchner and Prof. Julia Kunze-Liebhäuser. Electrochemical cells were assembled in atmospheric conditions and then purged with respective gases (Ar, CO₂ or O₂) for at least 60 min prior to any measurement. Experiments were conducted using a BioLogic VMP3 potentiostat. In order to shield any interference from outside, all experiments were carried out in a self-made Faraday cage.

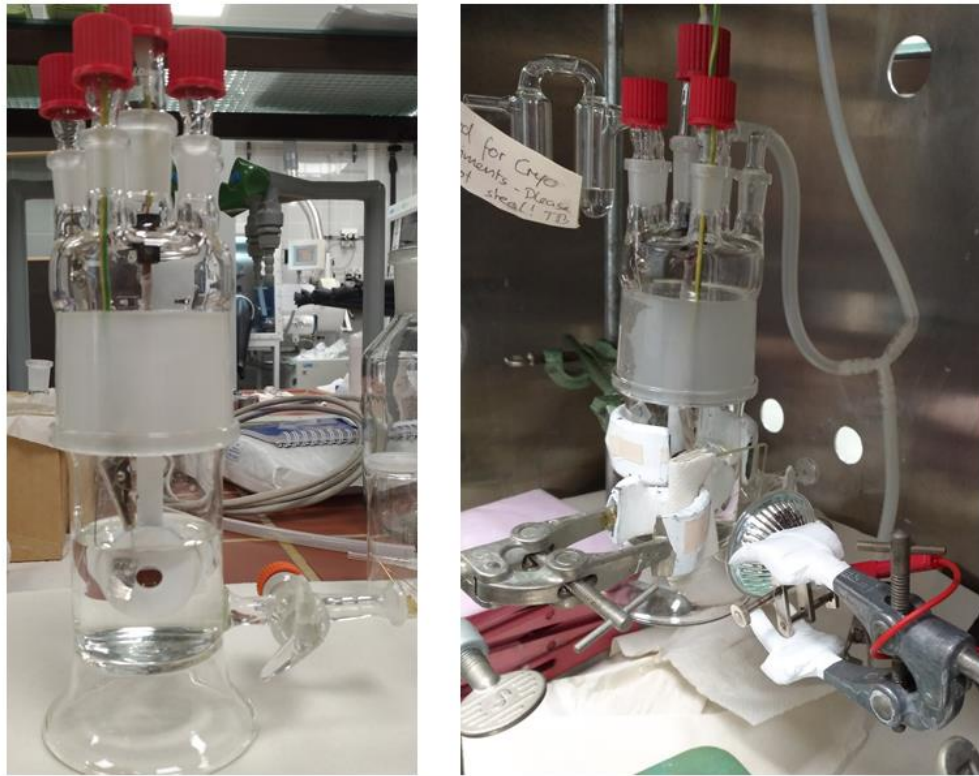


Figure 30. A typical EIS cell during assembly (on the left) and before measurement in a Faraday cage (on the right).

3. Results and Discussion

3.1. Carbon Capture and Storage (CCS) Using H-Bonded Pigments

Carbon dioxide capture is the key process to electrochemically or photochemically address it to form products. Once it's captured the molecular symmetry can be broken and the energy barrier which needs to be overcome for reducing carbon dioxide can be lowered. Among many others, electrochemical capture and release of carbon dioxide is an alternative way to existing technologies where the capture and release can be realized in ambient temperature and pressure. Existing technologies use temperature or pressure swinging to release captured carbon dioxide which can be energy intensive.

3.1.1. Carbon Capture and Storage in Organic Solvents

Quinacridone (QNC) was discovered in recent years to be an organic semiconductor^{121,122}. Its two-electron redox property makes it a suitable candidate for redox applications. Its long term stability and ease of processing together with its competitive cost makes it attractive as a semiconducting electrode¹²¹.

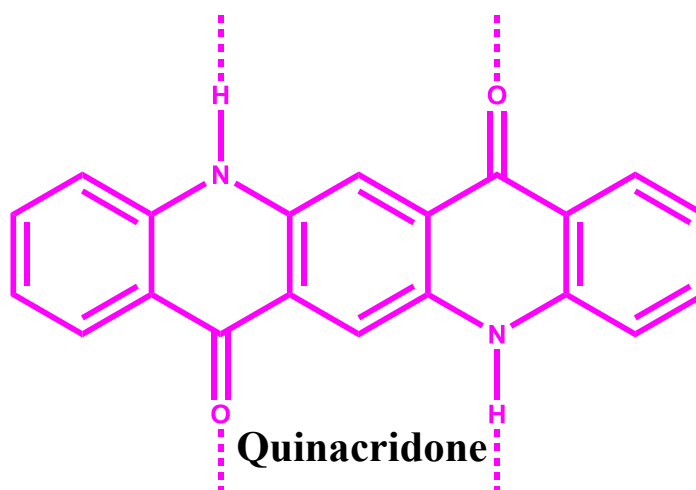


Figure 31. Chemical structure of Quinacridone

With these motivations in mind, quinacridone thin film electrodes were prepared by subliming quinacridone at 355°C in a home-made hot wall epitaxy system onto ITO slides.

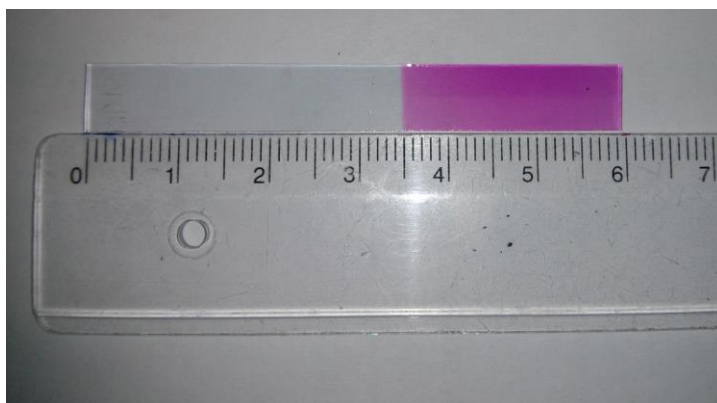


Figure 32. Photo of a ~100 nm Quinacridone thin film on an ITO coated glass slide.

The electrochemical characteristics of QNC were investigated in an electrochemical cell consisting of three-electrode setup. Glass/ITO/QNC was used as the working electrode; a silver wire coated with silver chloride was used as the reference electrode, and a Pt-plate electrode was utilized as the counter electrode. **Figure 33** shows the electrochemical behavior of the electrode under N_2 and under CO_2 saturated conditions.

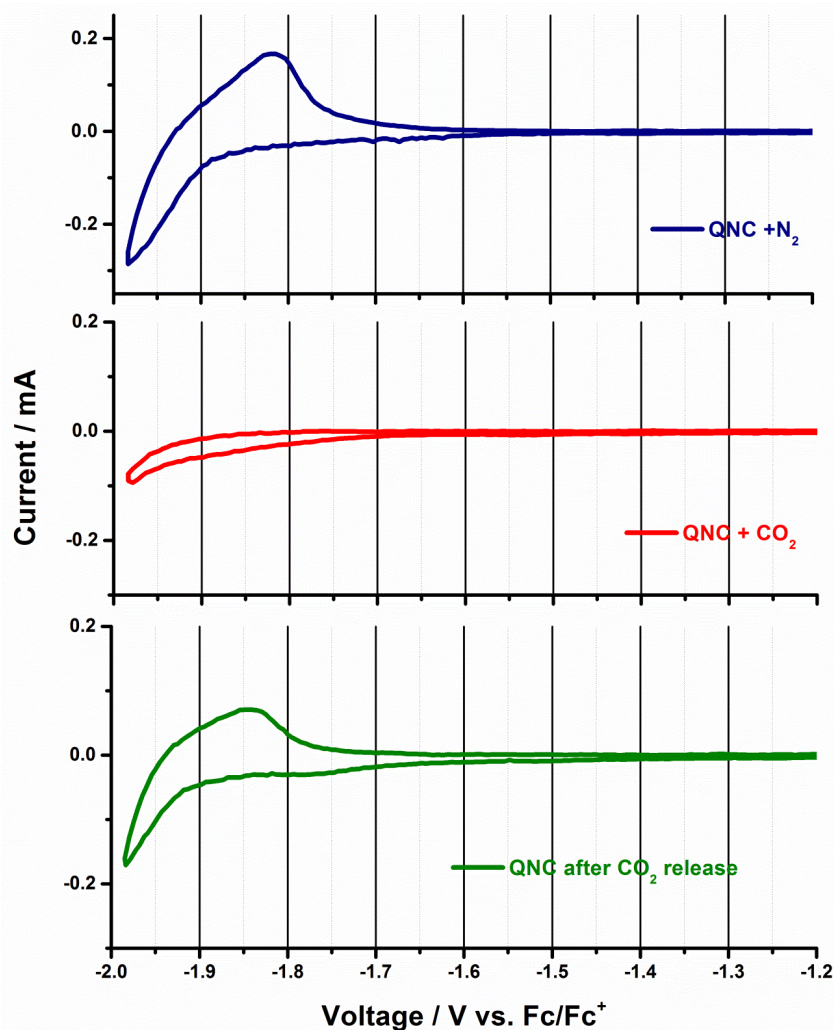


Figure 33. Electrochemical behavior of QNC under N_2 (blue curve), under CO_2 (red curve) and after CO_2 release (green curve).

Under N_2 atmosphere QNC shows a reversible reduction peak around -1950 mV and its re-oxidation at around -1820 mV vs. Fc/Fc^+ originating from the carbonyl moiety on Quinacridone. Upon saturation of the electrolyte solution with CO_2 the characteristic peak diminishes yielding a featureless voltammogram. Upon release of CO_2 the peaks can be recovered (green curve). The release of carbon dioxide was done in two ways. One of which is thermal release where the CO_2 loaded electrode is placed in an air-tight container equipped with a septum on top which then was placed on a heater. The heating and the release of carbon dioxide was monitored with a Lab-view program and an IFS66/S FTIR spectrophotometer with an air-tight gas transmission cell.

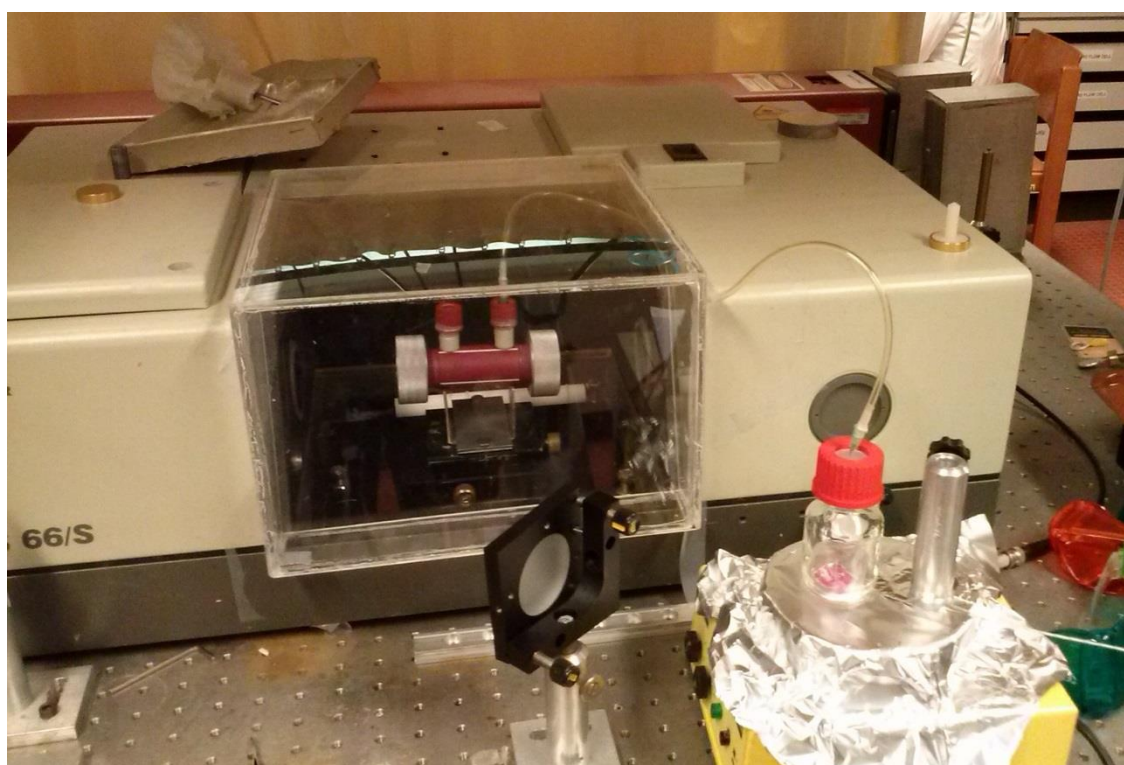


Figure 34. Setup used for the time-dependent release of CO_2 from the QNC electrode upon heating.

Release of CO_2 started around $40^\circ C$ and reached a saturation value at around $120^\circ C$ (**Figure 35**). The amount of CO_2 was determined using a calibration curve made by increasing the amount of CO_2 in the transmission cell and calculating the area under the CO_2 peak at around 2348 cm^{-1} .

For electrochemical release of CO_2 the electrolyte solution was purged with N_2 vigorously after electrochemical capture. CO_2 loaded electrode remained in solution while purging. After purging the electrolyte and the electrochemical cell to remove any residual uncaptured CO_2 potential was cycled between 1000 mV and -1900 mV to release captured CO_2 . **Figure 36** shows the electrochemical behavior of the electrode under N_2 (blue curve), under CO_2 (red curve) and under N_2 again after release (green curve). Scanning towards positive potentials yielded a peak around 10 mV which was attributed the release of CO_2 . Further scanning showed the recovery of oxidation peaks of QNC which were first observed in blue curve under N_2 . A sample of 2 mL was taken from the headspace of the air-tight cell and was injected to gas transmission cell in

sampling room of FTIR spectrophotometer to estimate the amount of released CO₂. In both cases (thermal and electrochemical release) it is assumed that the released amount of CO₂ is equal to the amount of CO₂ captured.

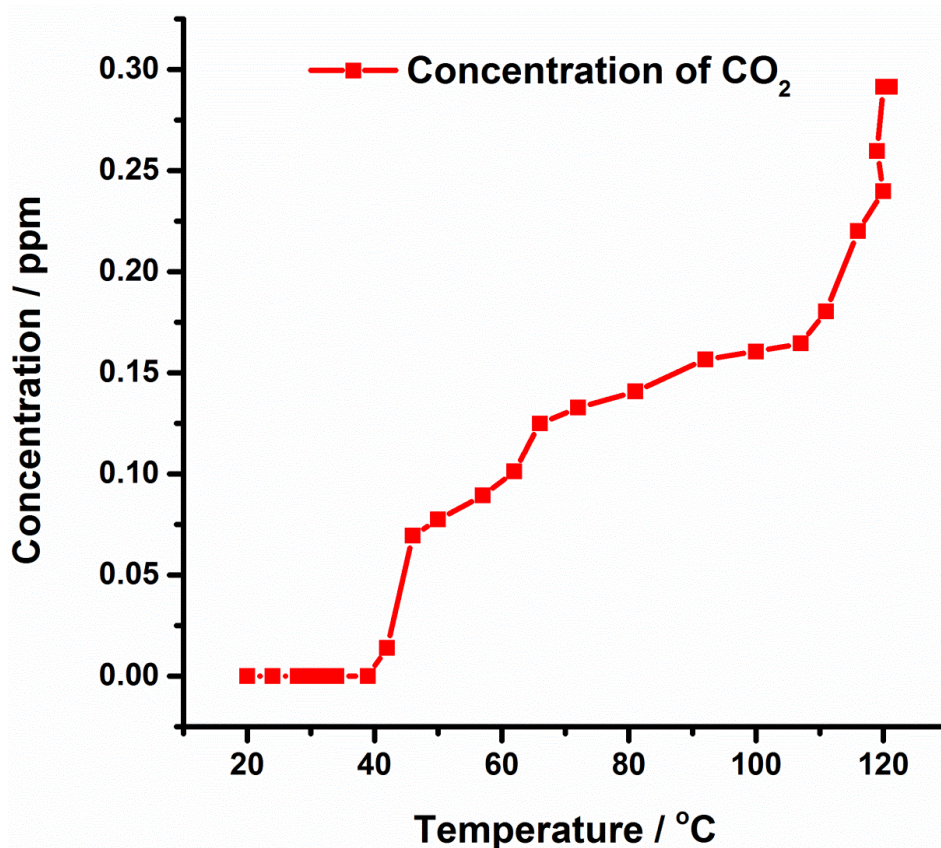


Figure 35. Release of CO₂ over time upon heating the electrode.

The figure of merit for assessing the performance of a CO₂ capturing agent is the “Uptake Capacity” which is demonstrated by the millimoles of CO₂ captured by a gram of capturing agent. The amount of captured CO₂ was calculated from the headspace using FTIR spectroscopy. For calculating the amount of QNC on the surface, two methods were utilized. In the first method the thickness of the QNC film was used together with the geometric dimensions of the electrode. The density of QNC was taken as 1.47 g/cm³¹²³. From this calculation the amount of QNC on the surface was found as 1.35 × 10⁻⁷ mol. The second method is the calculation of the charge passed through the electrode in one cycle of the cyclic voltammetry under N₂ which can then be correlated to the amount of electrochemically active species. This method gave similar results to the first method.

The uptake capacities for thermal and electrochemical were calculated as 2.28 mmol CO₂ / g QNC and 4.61 mmol CO₂ / g QNC, respectively^{124,125}.

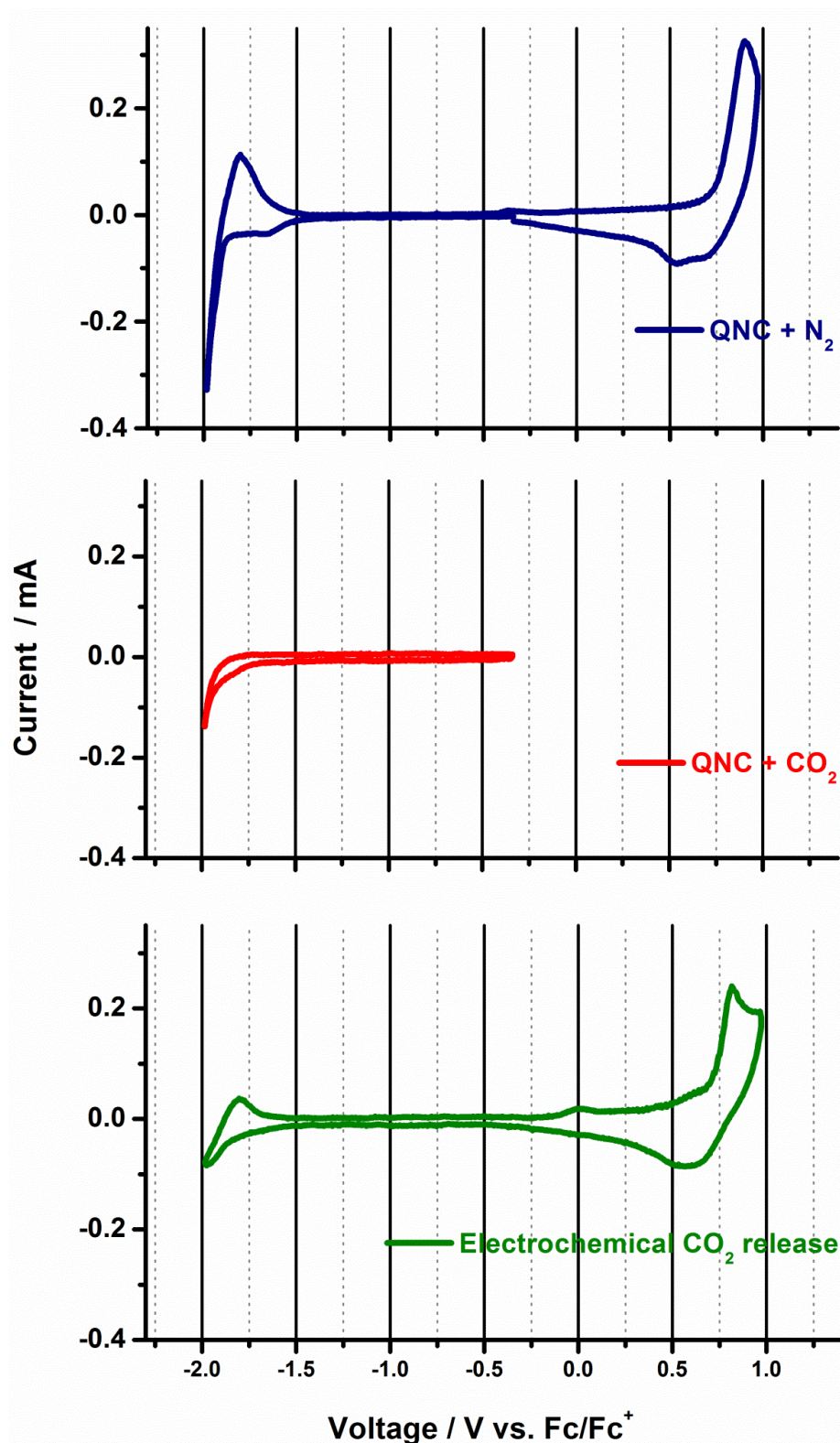


Figure 36. Cyclic voltammetry of QNC thin film depicting the electrochemical capture and release of CO₂.

Based on the determination of amount of captured CO₂ the molar ratios of CO₂ to QNC was calculated as 0.70:1 and 1.43:1 for thermal and electrochemical release cases. In this respect, it can be concluded that the electrochemical release is more efficient than the thermal release.

Next, building on these results a definitive reaction stoichiometry cannot be determined, *i.e.*, whether one or two carbonates attach to each QNC molecule, as the reaction is likely more complete at the surface of the film than in bulk. Nevertheless, it is plausible to assume that there are two carbonate groups per QNC molecule based on the 1.43:1 ratio found in the electrochemical release case, and also based on the assumed formation of a dienolate structure¹²³. Like the better-known indigoid and anthraquinone vat dyes; due to the electron-accepting properties of conjugated segments with carbonyl groups it is known that the carbonyl family of dyes and pigments undergo electrochemical reduction³¹. QNC forms a dienolate structure upon two-electron reduction¹²³. Building forward from the previous information, a mechanistic proposal where each enolate attacks a CO₂ molecule, forming a dicarbonate structure can be made. This structure is then stabilized by the extensive hydrogen bonding in the QNC. Newly formed dicarbonate-QNC carries a net charge of “-2”, with two tetrabutylammonium counterions maintaining the charge neutrality^{124,125}.

Based on these assumptions, previous work³⁰ and the amount of released CO₂ a mechanistic picture is depicted in **Figure 37**.

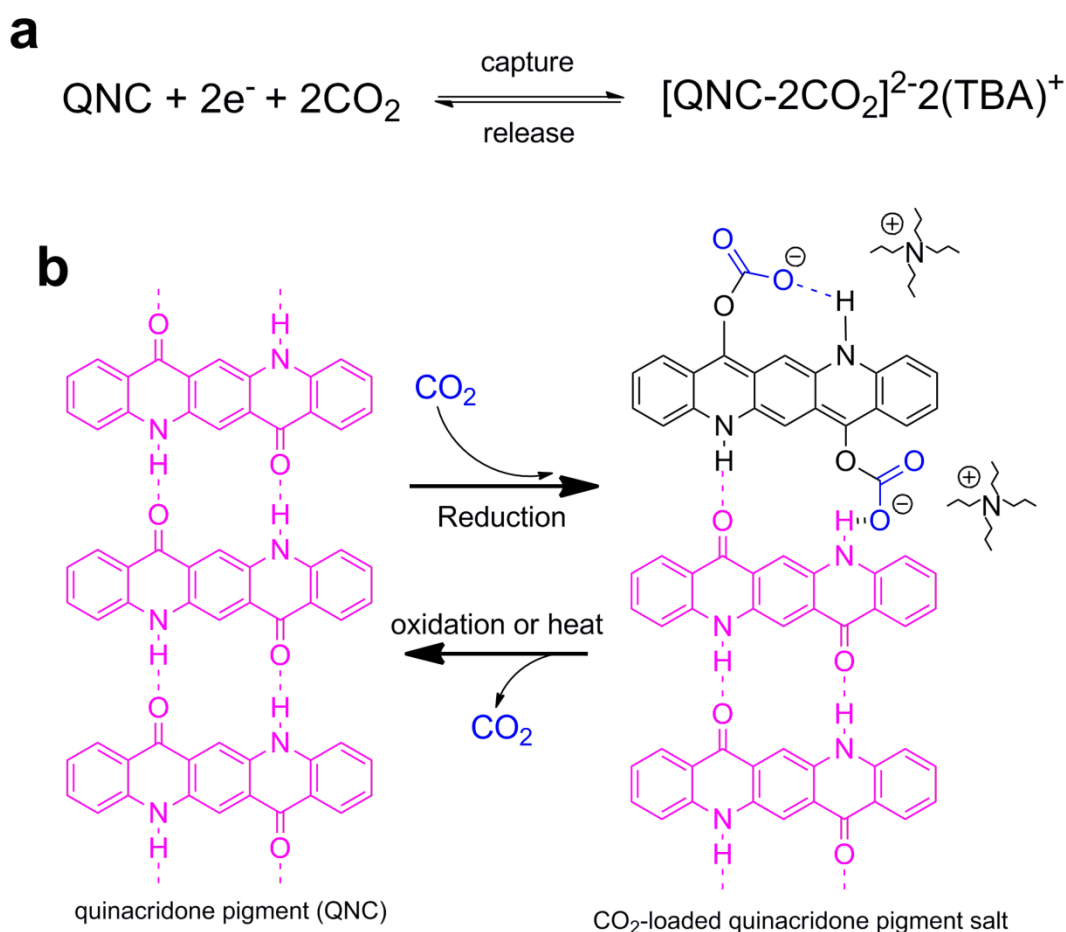


Figure 37. Overall equation for capture of CO₂ by a QNC molecule (a). Proposed mechanism for capture and release of CO₂ (b).

Owing to their characteristics, H-bonded carbonyl pigments tend to dissolve upon reduction or oxidation. This was also the case for QNC. Although CO₂-loaded structure is more stable upon potential cycling the overall reproducibility over repetitive cycling is limited. Maximum 15 consecutive capture-release cycles can be obtained for QNC. Further electrochemical treatment causes QNC thin film to dissolve. To overcome this issue our group has introduced an H-bonded conjugated polymer based on Indigo¹²⁶ which is another well-known H-bonded pigment for vat dyeing of jeans. The details for the synthesis can be found in the abovementioned reference.

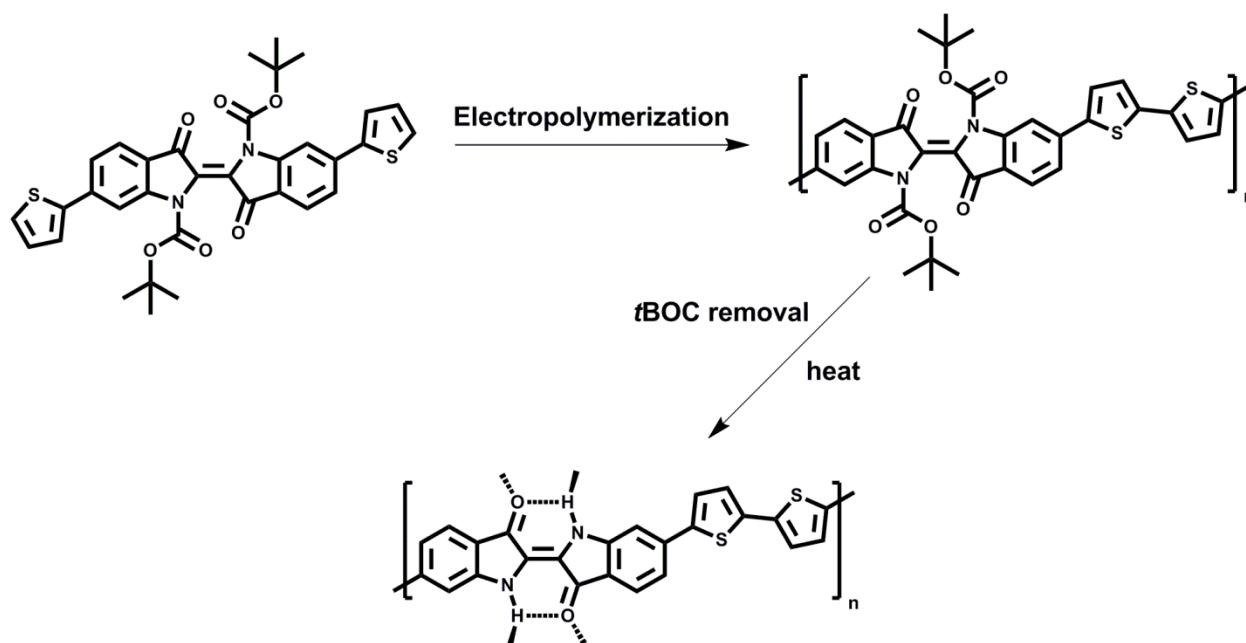


Figure 38. Electrosynthesis of poly(dithienyl indigo) (PDTI).

The solubilizing tBOC moieties on nitrogen atoms allow the otherwise-insoluble indigo to be chemically altered. Upon introduction of tBOC the indigo structure becomes soluble so that the thiophene substitutions can be added on 6,6' positions. After that the monomer DTI was placed in a solution containing 0.1 M TBAPF₆ in acetonitrile with a concentration of 5 mM. A three-electrode electrochemical setup was used where an ITO coated glass slide served as the working electrode with a Ag/AgCl quasi-reference electrode and a Pt-plate counter electrode. Potentiodynamic polymerization of the monomer yielded the polymer PDTI. Afterwards the electrode was heated up to 150 °C for 10 min to remove the solubilizing tBOC moieties. Later on PDTI was placed in a monomer free 0.1 M TBAPF₆ solution in acetonitrile and its electrochemical behavior was observed under N₂ and under CO₂ (**Figure 39**).

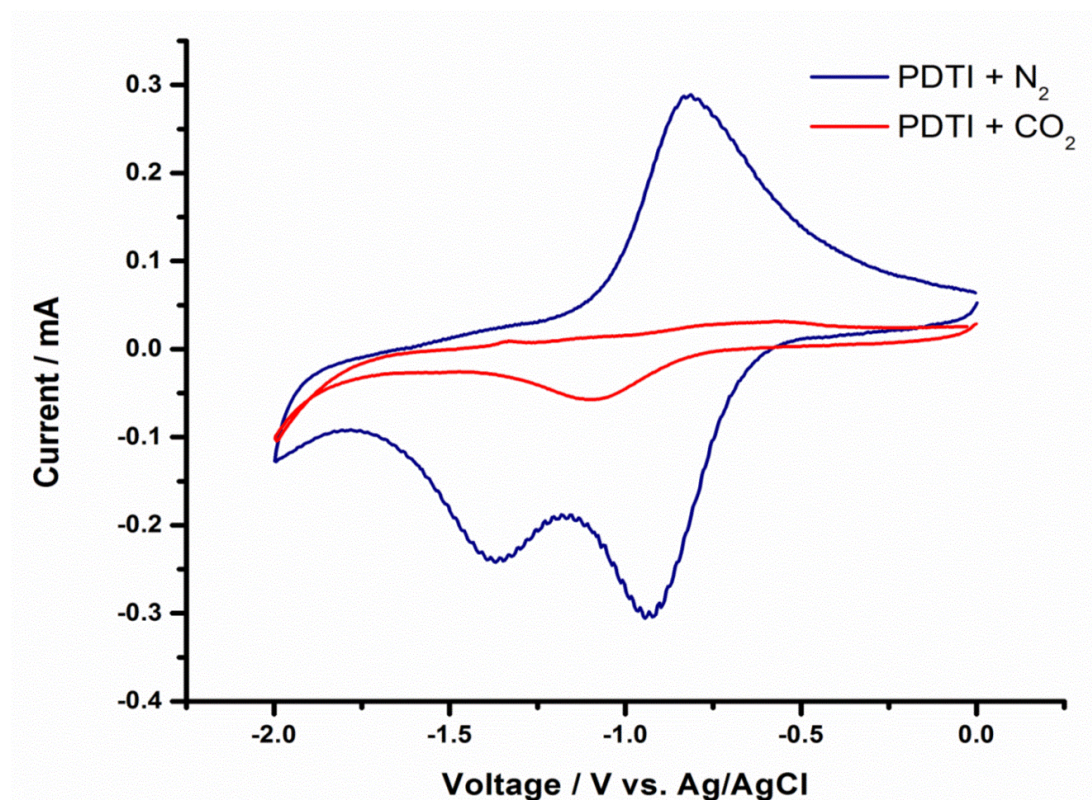


Figure 39. Electrochemical behavior of PDTI under N_2 (blue curve) and under CO_2 (red curve).

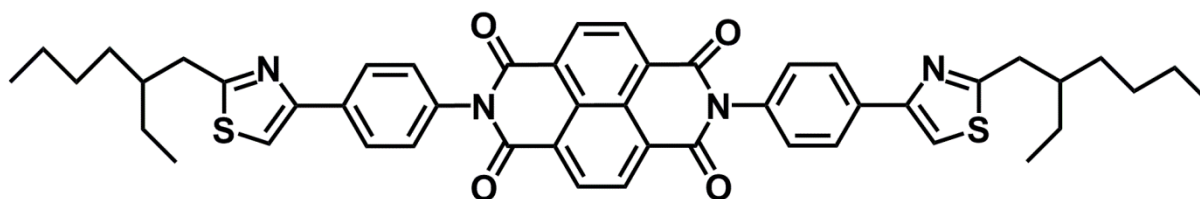
As can be seen from the voltammogram the blue curve yielded two characteristic peaks originating from the 2-electron reduction of carbonyl moiety of the polymer. Upon introduction of CO_2 these peaks disappeared and a new peak around -1.25 V appeared. This peak might be authored by the electrochemical behavior of the polymer backbone. Upon releasing of CO_2 electrochemically the characteristic peaks were recovered but not the full extent. PDTI is stable in abovementioned electrochemical conditions up to 500 cycles which addresses the problem of encountered in QNC case.

Up to now, the electrochemical capture and release of carbon dioxide was carried out in organic solvents which might limit everyday applications. Organic solvents can be expensive and disposal is energy intensive. CO_2 capturing agents that are active in water is a necessity.

3.1.2. Carbon Capture and Storage (CCS) in Aqueous Medium

For addressing the issue of CO_2 capture in water a carbonyl pigment which can undergo reduction within the electrochemical window of water splitting is necessary. This molecule should be n-type in character and must be electrochemically addressable with a high overpotential for hydrogen evolution. With these in mind a new molecule designed and synthesized by Monika Gora of Warsaw University was introduced (**Figure 40**).

a)



b)

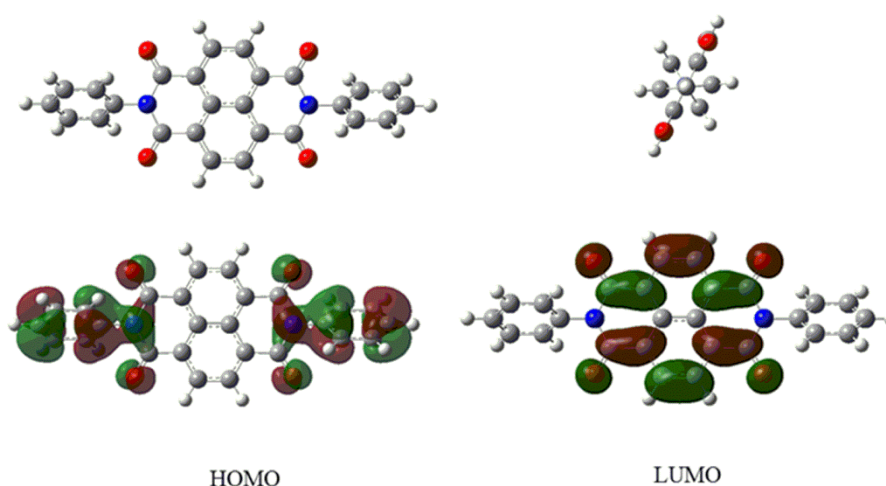


Figure 40. Chemical structure of 2,7-bis(4-(2-(2-ethylhexyl)thiazol-4-yl)phenyl)benzo[Imn][3,8]phenanthroline-1,3,6,8(2H,7H)-tetraone (NBIT) (a). DFT calculations showing the HOMO and LUMO levels of NBIT.

As DFT calculations shows the LUMO level lies on the naphthalene bisimide core of the structure. The naphthalene bisimide core was chosen as the electron-deficient carbonyl pigment unit. To further lower its reduction potential to ensure reduction of the carbonyl moieties in aqueous electrolytes at potentials more positive than the onset of proton reduction, para-phenylene thiazole substituents were added. This, however, might be a trade-off due to the lowering of reduction potential which might eventually affect the nucleophilic character of the enolate that is formed as a result of reduction¹²⁷. Finally, 2-ethylhexyl termination was chosen to provide resistance to dissolution in aqueous electrolyte upon repeated cycling.

NBIT was deposited on glassy carbon electrodes from its solution in chlorobenzene via spin coating. Glassy carbon was chosen due to its high overpotential against hydrogen evolution in water. The thickness of NBIT was measured with a Dektak Profilometer and found to be on the order of 100 nm. Backside of the glassy carbon electrode was coated with a PMMA solution ($M_w = \sim 1000000$, 50mg in 5 mL chlorobenzene) and dried off to prevent any electrochemical activity originating from the glassy carbon itself.

NBIT coated glassy carbon was then placed into a two-compartment homemade electrochemical cell (**Figure 41**).

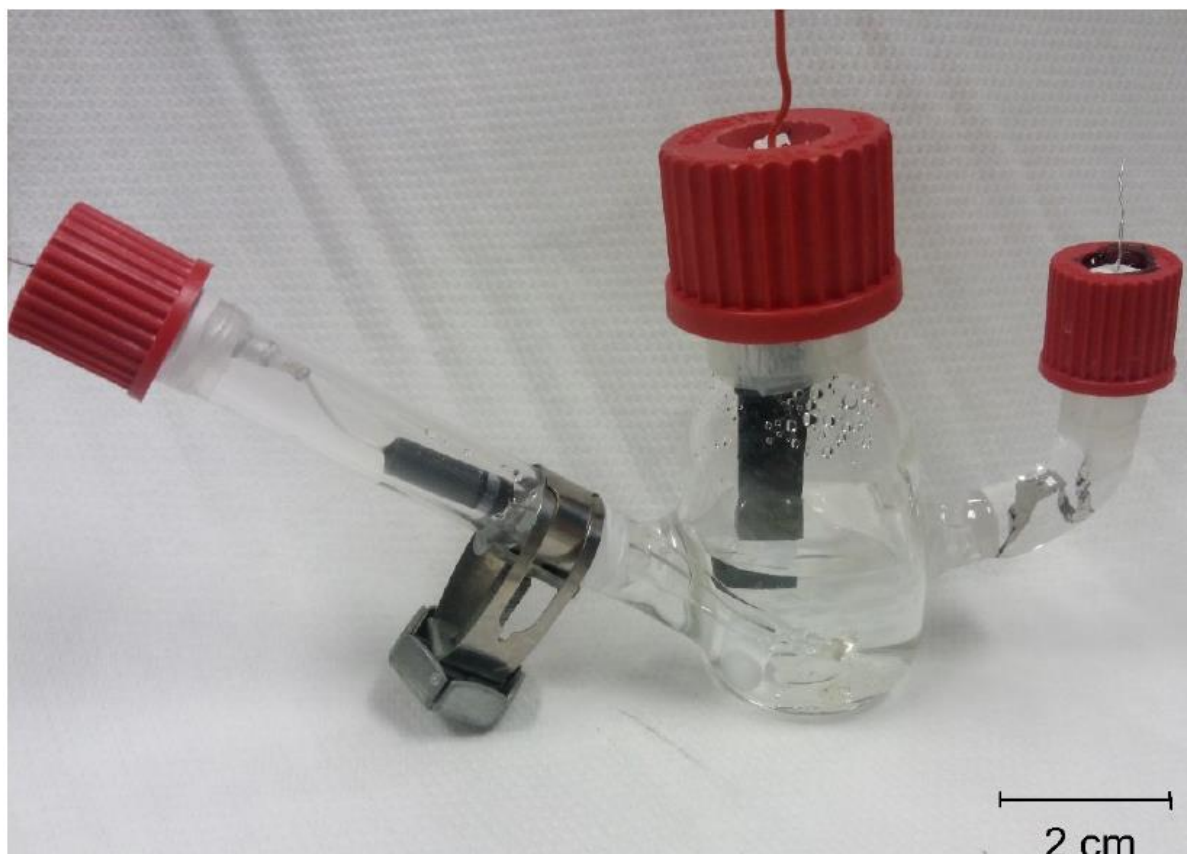


Figure 41. Two-compartment electrochemical cell.

An Ag/AgCl (3.5 M KCl) served as the reference electrode in the same chamber as the working electrode whereas a Pt plate was used in the anode chamber as the counter electrode. Since the solubility of atmospheric oxygen in water is quite high (8 mg/L) aqueous solutions need more time for N₂ purging. Prior to each experiment the electrochemical cell was purged for 90 min with respective gases which are N₂ and CO₂ in this case. 0.1 M Na₂SO₄ in water was used as the electrolyte solution.

Electrochemical behavior of NBIT under N₂ and CO₂ can be seen in **Figure 42**.

Upon cycling between 0 and -1 V NBIT shows a quasi-reversible one-electron reduction at -0.7 V and a second one-electron reversible reduction at -0.85 V. These peaks are fingerprints for many other carbonyl pigments and have been reported previously^{126,128–132}. NBIT can withstand 20 cycles under N₂ saturated conditions without showing any change in its electrochemical behavior and up to 30 cycles with a 30% decrease in current density (**Figure 43**). When the electrolyte solution is saturated with CO₂ and the potential is cycled, a complete loss of the peaks is observed (**Figure 42** blue curve). The stability under CO₂ atmosphere is different than that of N₂. The word stability should not be confused with the chemical stability but rather its stability as a compact film on the surface. In the case of N₂ saturated conditions NBIT becomes soluble upon repetitive cycling under reductive conditions. The reduced NBIT in solution can be observed upon UV-vis measurement¹³³.

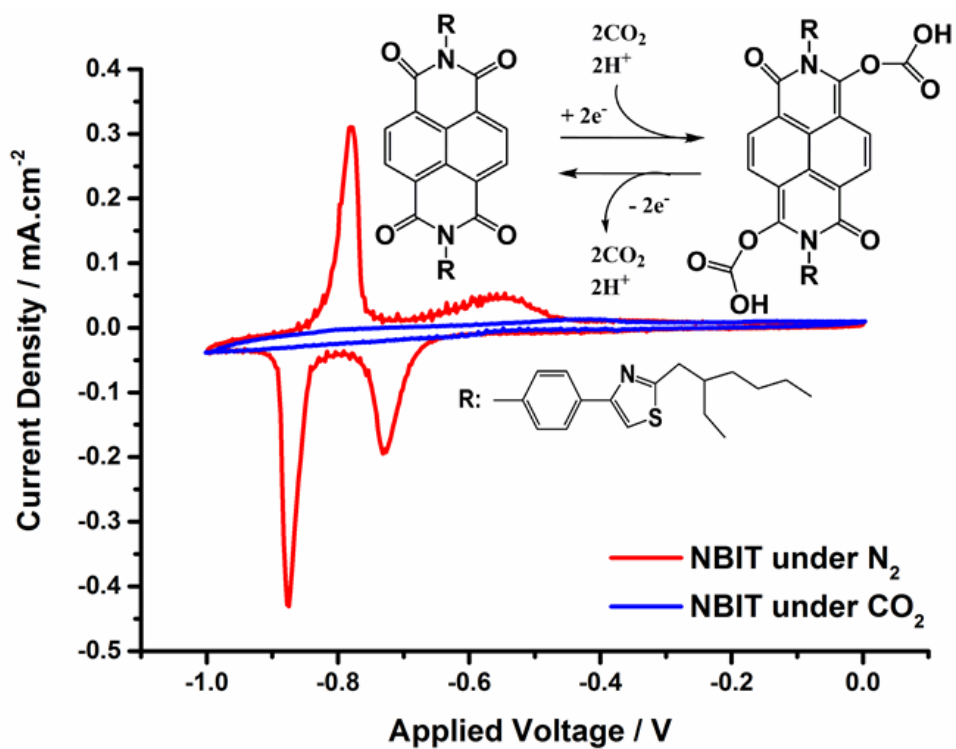


Figure 42. Electrochemical behavior of NBIT under N₂ (red curve) and under CO₂ (blue curve). Inset: Proposed mechanism for CO₂ capture.

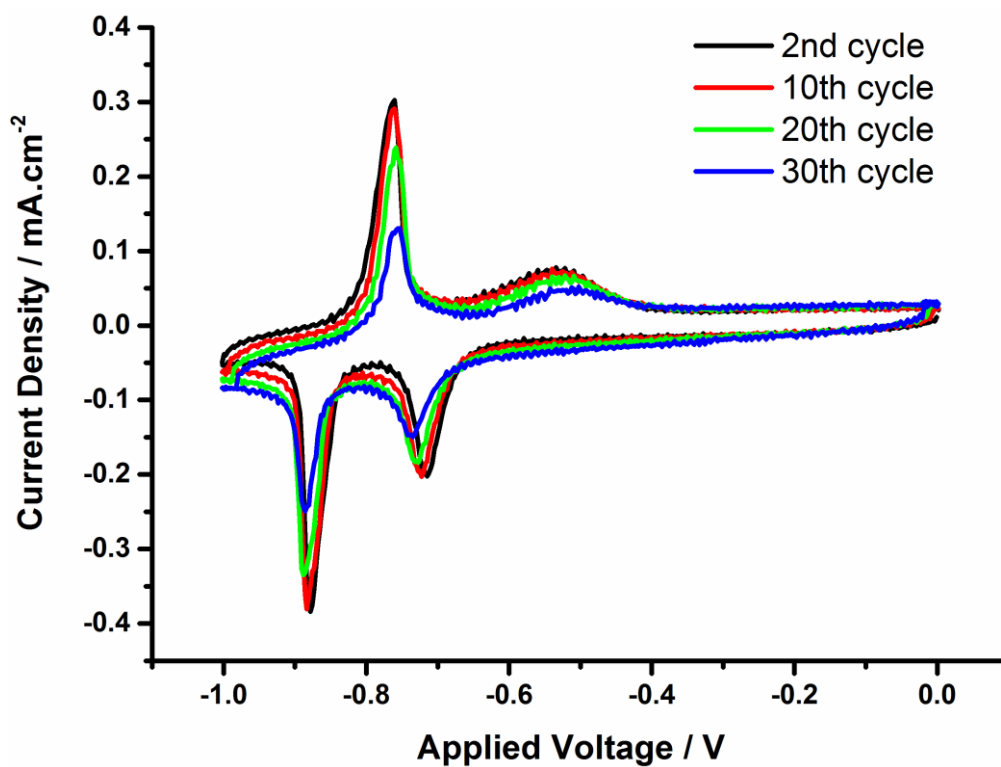


Figure 43. Cyclic stability of NBIT upon repetitive potential cycling.

The loss of peaks, as in the case of QNC, is signaling the binding of CO₂ to the now-reduced carbonyl groups. To support this, Gaussian 09 was employed for basic quantum-chemical calculations using a density functional theory (DFT) / HF-based method with the B3LYP hybrid functional and the 3-21g basis set. For the sake of simplicity and reducing the calculation time only the naphthalene bisimide core with phenyl rings was chosen for frequency calculation and geometry optimization (**Figure 44**).

In order to gauge electrochemical origin of the disappearance of the redox peaks, electrochemical impedance spectroscopy (EIS) was conducted. EIS was performed after 3 cyclic voltammograms to maintain quasi-reversible conditions. Spectra were collected in the potential range between 0 and -1.2 V with a step size of 0.2 V. Each applied potential was kept for 5 min to keep steady state before the impedance measurement. Frequency was ranged from 500 kHz to 100 mHz with a peak amplitude of ±10 mV. These set of measurements were performed both under Ar and under CO₂.

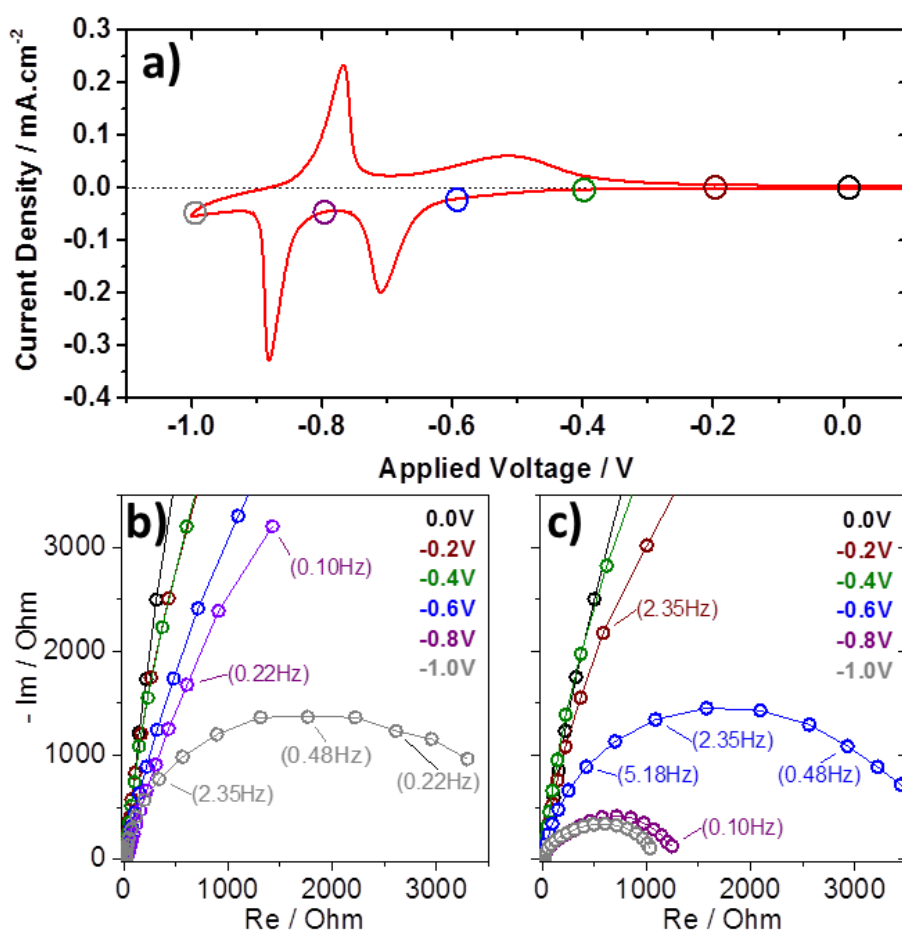


Figure 44. (a) CV of NBIT film on a glassy carbon electrode (WE) with colored points indicating the potentials of EIS data acquisition shown in b and c. Nyquist plots of NBIT film on a glassy carbon electrode (b) under Ar and (c) under CO₂ respectively.

It can be concluded from the EIS data that the ohmic resistance of the electrolyte solution (R_s) and the double layer capacitance (C_{dl}) were almost equal in all measurements. However, the charge transfer resistance (R_{ct}) changed substantially. Ohmic resistances from 15.5 Ω to 17.0 Ω were measured under Ar and under CO₂ respectively. C_{dl} varied from 26 to 71 $\mu\text{F cm}^{-2}$. It was found that the R_{ct} of the NBIT film was strongly dependent on the atmosphere. R_{ct} decreased significantly with the applied decreasing potential. Although under Ar atmosphere, at high potentials between 0.0 V and -0.6 V, the R_{ct} was expected to be very large and could not be measured within the given frequency range, it was found to be 2864 Ω at -1.0 V and 537 Ω at -1.2 V, respectively. Under CO₂ atmosphere the R_{ct} changed from 3213 Ω at -0.6 V to 746 Ω at -1.0 V and finally to 96 Ω at -1.2 V. Even though the measurements under Ar saturation can be well-explained by a single R/C element in series with the R_s (**Figure 45a**), two R/C elements have to be used, in series with the R_s , to fit the spectra under CO₂ saturation at -0.8 V and below, indicating the presence of two time constants (**Figure 45b**). The first one may be attributed to the interface between the glassy carbon support and the NBIT film, while the second one is indicative for the interface between the NBIT film and the electrolyte. Because of the high resistance of the NBIT film under Ar atmosphere, the second interface to the electrolyte is not resolved with the performed EIS measurement. In general, the overall R_{ct} decreases with applied negative potential under both, Ar and CO₂ atmosphere, possibly through improved electronic conductivity of NBIT and most likely due to cathodic charge transfer at ≤ -1.0 V (**Figure 45b**).

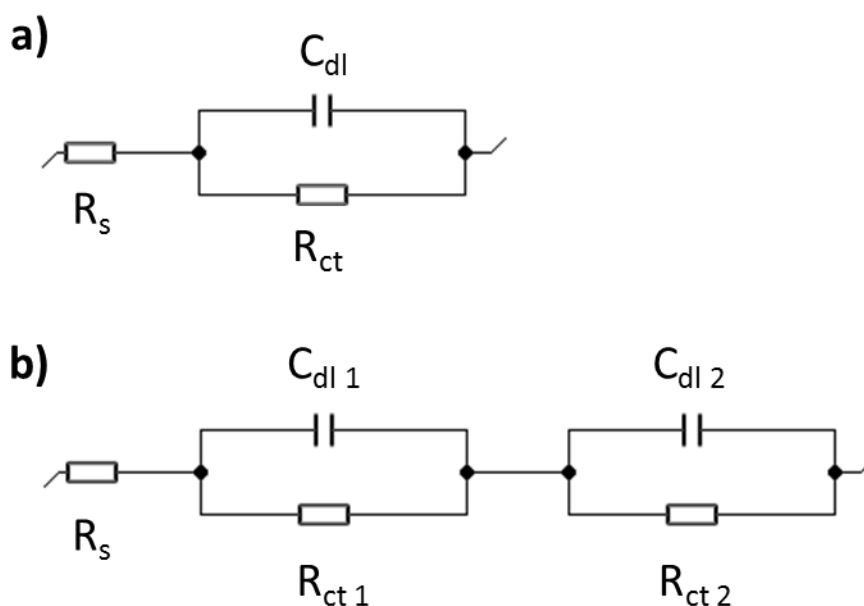


Figure 45. Corresponding equivalent electrical circuits for EIS data fitting of NBIT under (a) Ar atmosphere and (b) CO₂ atmosphere at -1.0V and below, consisting of the ohmic resistance of the electrolyte solution (R_s), the double layer capacitance (C_{dl}) and the charge transfers resistance (R_{ct}). While under Ar saturation the EIS data can be well explained by a single R/C element in series with the R_s two R/C elements have to be used, in series with the R_s , to fit the spectra under CO₂ saturation at -1.0V and below.

For the confirmation of the aforementioned carbonate-like structure, *in-situ* attenuated total reflection Fourier transform infrared spectroelectrochemistry (ATR-FTIR-SPEC) technique was employed. NBIT film was coated on a Ge crystal which served as both the reflection element and the working electrode. A Pt plate together with a silver chloride coated silver electrode served as counter and quasi-reference electrodes, respectively.

Figure 46 shows the FTIR characteristics of NBIT film under a constant flow of CO₂-saturated electrolyte (flow rate = 3 mL min⁻¹) at different potentials. Prior to electrochemistry a FTIR spectrum was recorded as the baseline. As the potential of -0.8 V was applied to the working electrode, changes in the FTIR spectrum became visible. A peak arising at ~ 3700 cm⁻¹ signaling the formation secondary alcohol, started to decrease upon applying more negative potentials to yield a peak around ~3300 cm⁻¹ corresponding to carboxylic acid-like - OH functionality. This behavior was associated with the formation of carbonate-like structure upon addition of CO₂ to the now-activated carbonyl group. In addition, the peak around ~1670–1680 cm⁻¹, which corresponds to the imide carbonyl, decreased as a new peak at 1277 cm⁻¹ rose, exhibiting formation of carbonate-like structure^{133,134}.

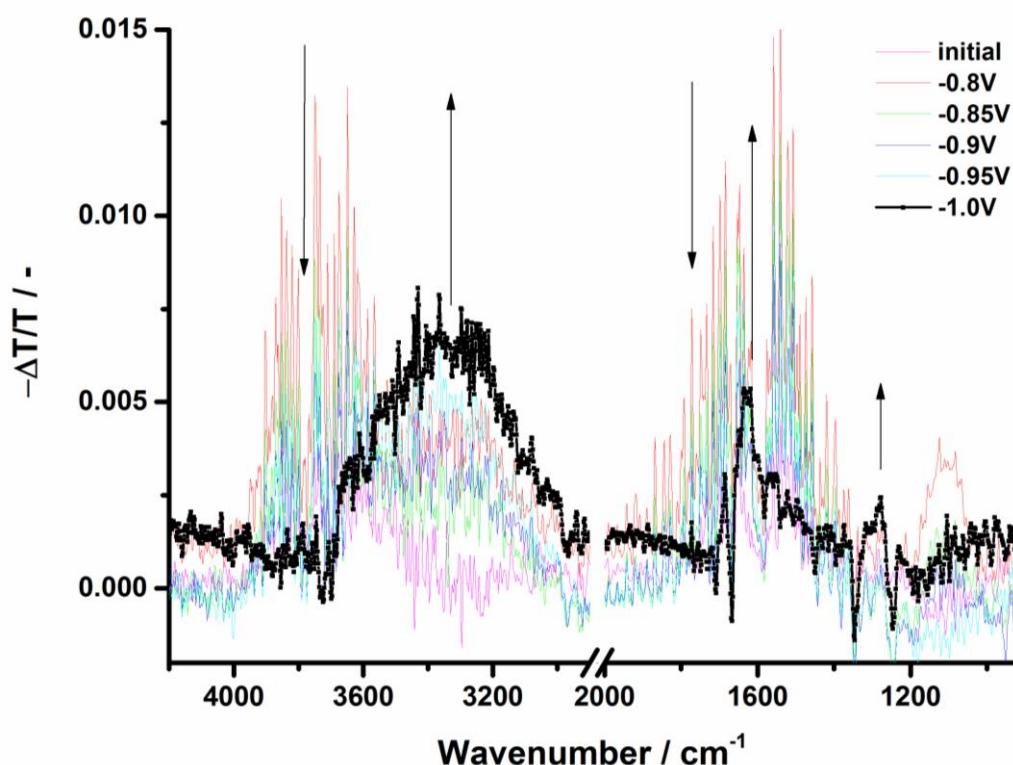


Figure 46. *In-situ* ATR-FTIR-SPEC spectrum of NBIT under CO₂.

Finally, the uptake efficiency of NBIT, which is the figure of merit for CO₂ capture agents, was determined to be ~2.3 mmol CO₂ g⁻¹¹³⁵. The amount of CO₂ was determined by gas chromatography (GC). After the CO₂ was electrochemically captured by the NBIT film from CO₂-saturated solution, the electrolyte solution was purged with N₂ for 120 min to assure that no residual CO₂ was present in the solution. Upon electrochemical oxidation captured CO₂ was released. The release of CO₂ can be observed electrochemically with a new redox peak around 0.24 V and it was seen that the NBIT regained its characteristic peaks (**Figure 47**). A 2 mL headspace sample was taken with a gas-tight glass syringe and injected into GC. The number of NBIT molecules in the film was determined spectrophotometrically as well as electrochemically. The part of the film that was exposed to electrochemical treatment was dried and then dissolved into quartz UV-vis cuvette using chlorobenzene as the solvent. Absorbance measurement was performed, and the amount of NBIT on the surface was found as 22.8 nmol using molar extinction coefficient, which was determined using a calibration curve. Integration of total charge during one CV measurement can be used to estimate the number of electrochemically active

molecules on the surface^{115,136}. In the case of NBIT, this value was found to be 19.1 nmol, which is in good agreement with the obtained value via spectroscopy. The faradaic efficiency of the process can be calculated via dividing the amount of captured CO₂ (3.49×10^{-8} mol) with the number of electrons used for the capture (3.82×10^{-8} mol). CO₂ capture process for NBIT yielded a faradaic efficiency of 91 %.

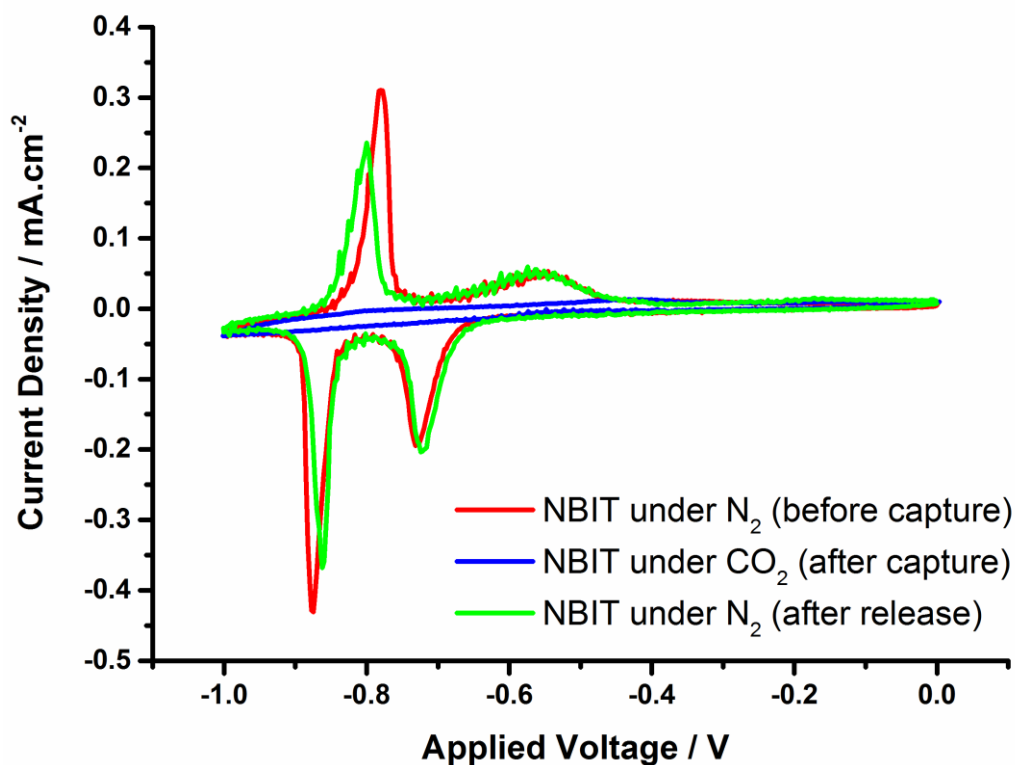


Figure 47. Cyclic voltammogram of NBIT under N₂ (red curve), after CO₂ capture (blue curve) and after CO₂ release (green curve).

This pair of study shows that carbonyl bearing pigments are efficient CO₂ capturing agents and they can be operated under ambient temperature and pressure conditions. They do not require temperature or pressure swinging for the release of captured CO₂. Capture and release process can completely be controlled electrochemically. This is an important step in order to break the molecular symmetry of CO₂ which is a linear molecule in its natural state.

Further addressing of this captured CO₂ is needed in order to reduce it to useful chemicals. One way to achieve this might be the introduction of metal islands on and beneath the surface of the pigments. Interested readers are encouraged to refer to Dominik Wielend's master thesis (can be found in LIOS webpage) where several different carbonyl bearing pigments were screened for their ability to capture CO₂ as well as deposition of metal islands on and beneath the film to address captured CO₂ was investigated.

3.2. Heterogeneous Photoelectrocatalysis Using Organic Semiconductor Modified Electrodes

3.2.1. Third Generation of Conjugated Polymers for CO₂ Reduction

The term “Third-Generation of Conjugated Polymers” (**Figure 48**) was coined in late 80s collectively by several studies^{137–143}. Several studies reported on the synthesis modified polypyrroles and polythiophenes with the aim of introducing a new type of conjugated polymeric structure which is not only processable and highly conducting but also possessing new physical and/or chemical properties for advanced applications.

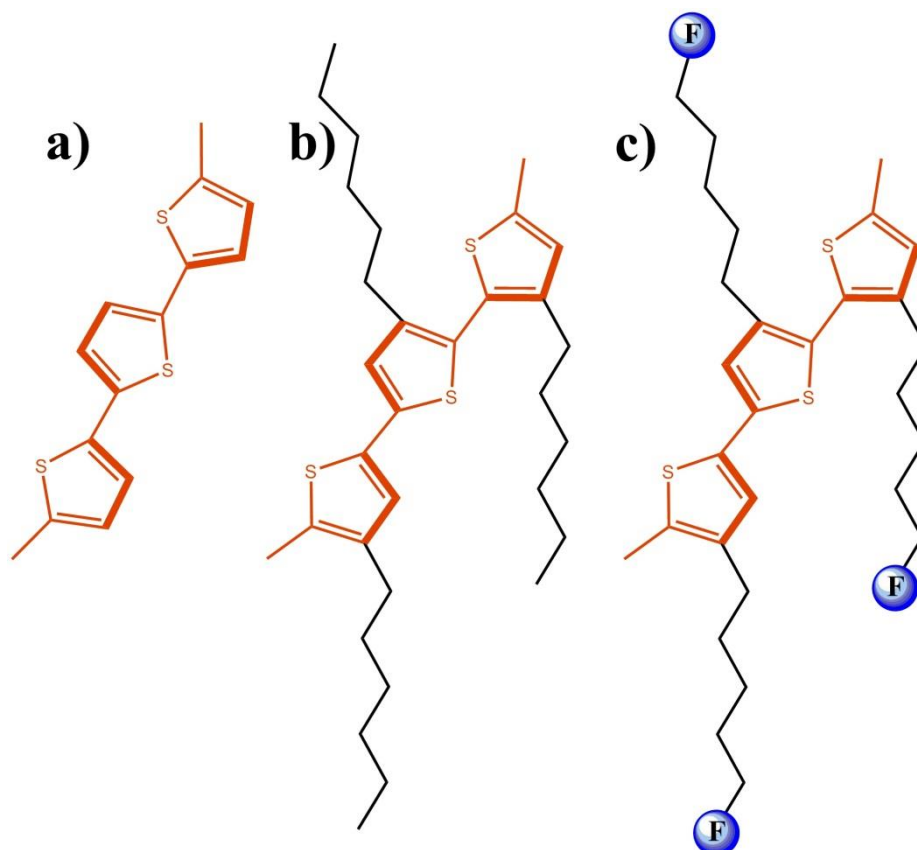
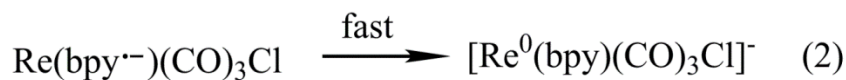
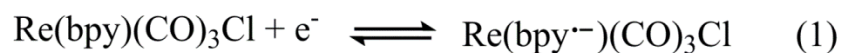


Figure 48. Three generations of conjugated polymers; a) Polymers with good conductivity but low processability, b) Polymers with alkyl chains allowing solubility hence processability, c) Polymers with good conductivity, processability and/or new chemical/physical functions/properties.

As mentioned in previous chapters, Re(I) (bpy)(CO)₃Cl (Lehn catalyst) is one of the most effective catalysts for photochemical and electrochemical reduction of carbon dioxide. It can be utilized in homogeneous conditions in organic solvents with concentrations changing between 1–3 mM^{60,86}. Homogeneous catalytic systems are widely studied and their mechanistic behavior is (most of the time) easier to characterize compared to their heterogeneous counterparts. However, their application can have several disadvantages. Large amounts of expensive catalyst are necessary for efficient CO₂ reduction (~10mg Lehn catalyst is required for 1mL CO produced)⁶⁰ and only the catalyst molecules which are in the proximity of the electrode surface will be active while the rest is idle. Furthermore, homogeneous catalysts may sometimes face solution deactivation pathways, such as the formation of dimers observed in certain rhenium

bipyridine complexes in non-aqueous solution^{87,144}. Dimer formation results in a sparingly soluble $[\text{Re}(\text{bpy})(\text{CO})_3]_2$ compound (**Scheme 1**) which is hindering further participation of the catalyst in catalytic cycle reducing the efficiency⁸⁷.



Scheme 1. Chemical reactions leading to the formation of $[\text{Re}(\text{bpy})(\text{CO})_3]_2$ dimer.

One way to overcome these problems is to immobilize the catalyst on an electrode hence switching from homogeneous to heterogeneous catalysis. The most commonly reported ways to immobilize Rhenium complexes onto solid electrodes were either the insertion of the molecule into a polymer matrix^{111,145,146} or chemical modification of the ligand with a functional group that enables polymerization to form a redox-active polymer^{110,113,147}.

Following these ideas a polythiophene derivative having Lehn catalyst as the pendant group was introduced (**Figure 49**). The polymer was obtained by the electropolymerization of the monomer $[\text{3HRe}(\text{bpy})(\text{CO})_3\text{Cl-Th}]$ on a Pt electrode. The synthetic details of the monomer leading to the electropolymerized catalyst can be found in Gottfried Aufischer's master thesis and I am grateful to Dr. Elisa Tordin and Gottfried Aufischer for providing me the monomer.

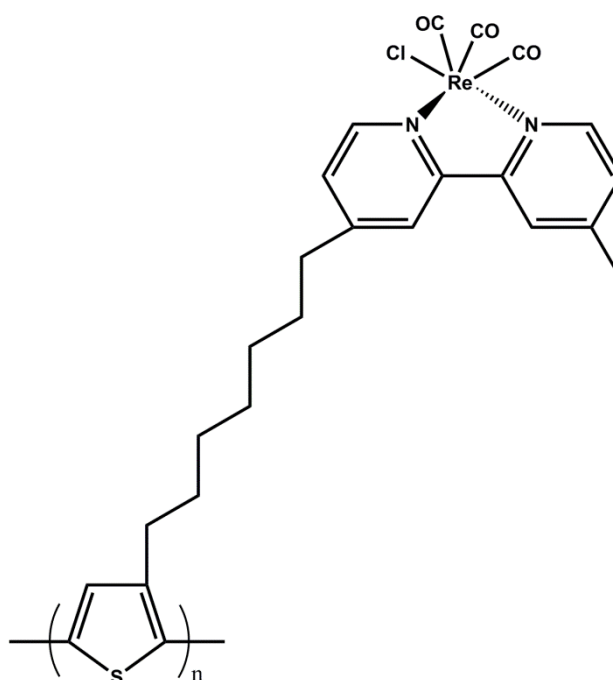


Figure 49. Chemical structure of P[3HRe(bpy)(CO)₃Cl-Th].

Monomer [3HRe(bpy)(CO)₃Cl-Th] was polymerized in a one-compartment cell containing Boron trifluoride diethyl etherate (BFEE) as the supporting electrolyte as well as the solvent with a three-electrode configuration. A Pt plate was used as the working electrode hence as substrate for the redox-active polymer. A silver wire coated with silver chloride was used as the quasi-reference electrode which then calibrated against Fc/Fc⁺ externally. Finally, a Pt-plate placed in the electrochemical cell served as the counter electrode. Polymerization was carried out under oxygen-excluded conditions by cycling the potential between 300mV and 1700mV vs. NHE. As the polymerization progressed, the peak around 1200mV which belongs to monomer decreased as a new broad peak between 600mV and 900mV evolved flagging the growth of the polymer growth. When the polymerization was finalized the surface of the Pt was fully covered with a thin layer of pale yellow polymer film. **Figure 50** contains a photo of a shiny gold color film deliberately grown very thick for visualization purposes. However, such thick films did not show any catalytic activity. For this reason thinner films represented with their CV scans in Figure 3 were used throughout all experiments.

In his original paper¹⁴⁸ Bocarsly suggested that a tiny organic molecule pyridine can reduce carbon dioxide all the way to methanol¹⁴⁹. Since then, pyridinium-catalyzed CO₂ reduction has generated immense discussion in the catalysis community^{150–156}. The arguments were varying from reproducibility of the experiments to undetectable products. Arguments were also focused on the origin of the electrochemical behavior of pyridinium and its assignment on cyclic voltammograms. Bocarsly suggested that the pyridinium ion has to be mobile in order to act as an electron shuttle to drive the electrocatalytic reduction of carbon dioxide. To address this point, a polythiophene with pyridine molecule as pendant group at this time (P[3HPyr-Th]) was electrosynthesized and investigated for its catalytic activity.

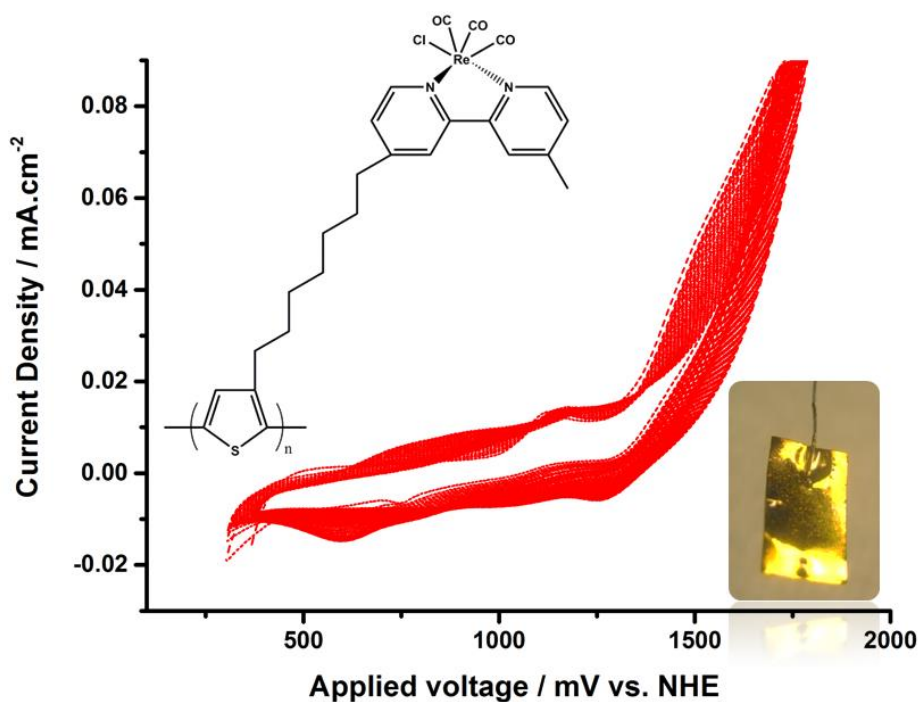


Figure 50. Electropolymerization of [3HRe(bpy)(CO)₃Cl-Th]. Inset: Photo of a very-thick polymer film for visualization.

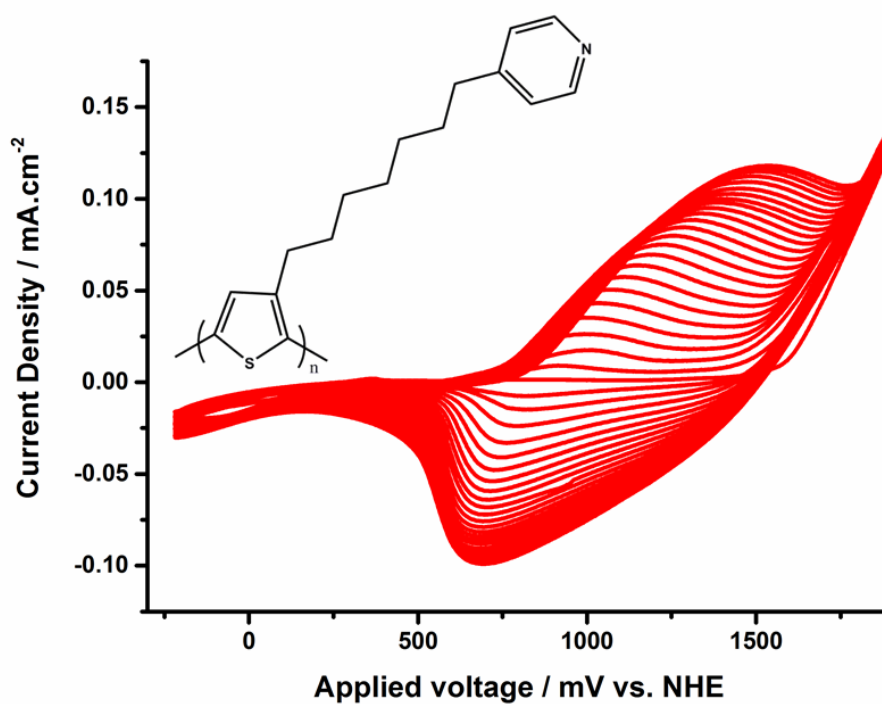


Figure 51. Electropolymerization of [3HPyr-Th].

Photoactivity of P[3HRe(bpy)(CO)₃Cl-Th] was evaluated by cyclic voltammetry measured in dark and under illumination. In order to assess the spectroscopic behavior of the electrode, a reflectance measurement of the electrode was done using PerkinElmer Lambda 1050 UV-Vis-NIR spectrophotometer equipped with an integrated sphere (**Figure 52**).

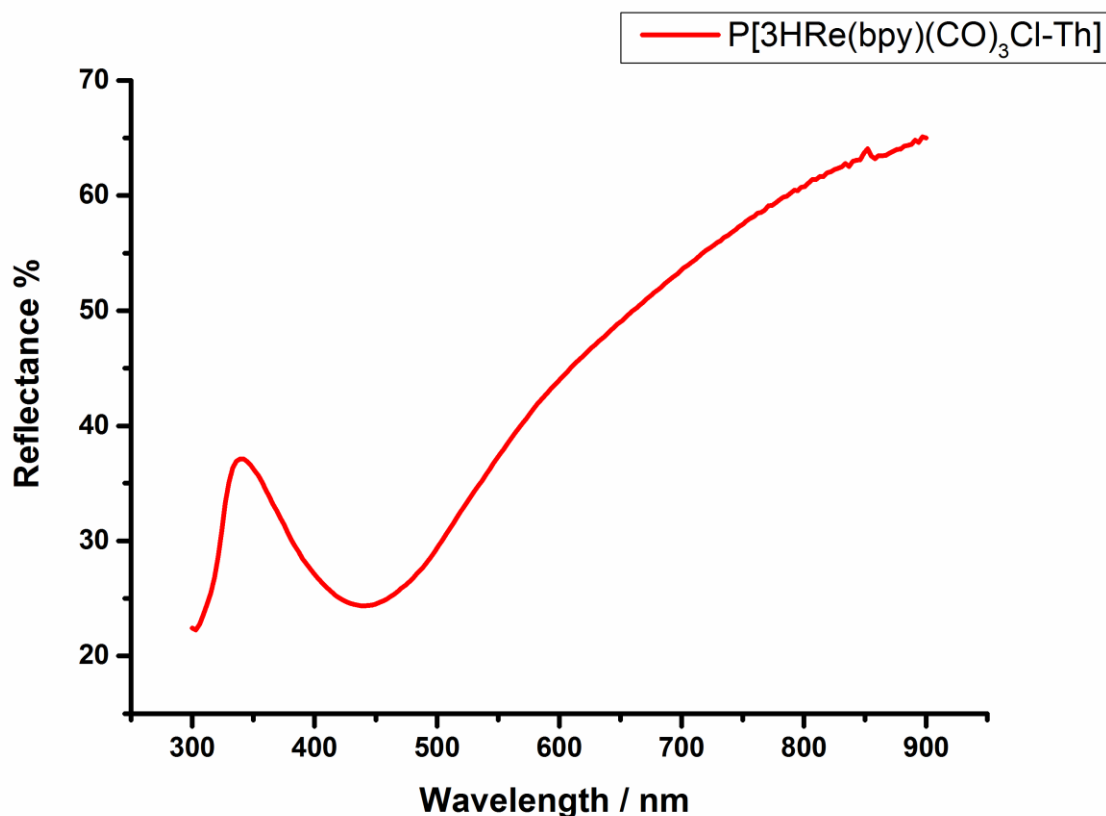


Figure 52. Reflectance spectrum of P[3HRe(bpy)(CO)₃Cl-Th]

Figure 53 shows the electrochemical behavior of the electrode in dark and under illumination. Illumination was achieved with a halogen lamp (Philipps GU 5.3 50W, 12V 36D). An IR glass filter was used in order to avoid the electrochemical cell medium to heat up. Intensity of the light in the vicinity of the photocathode was determined to be 60 mW cm⁻² using a calibrated Si diode.

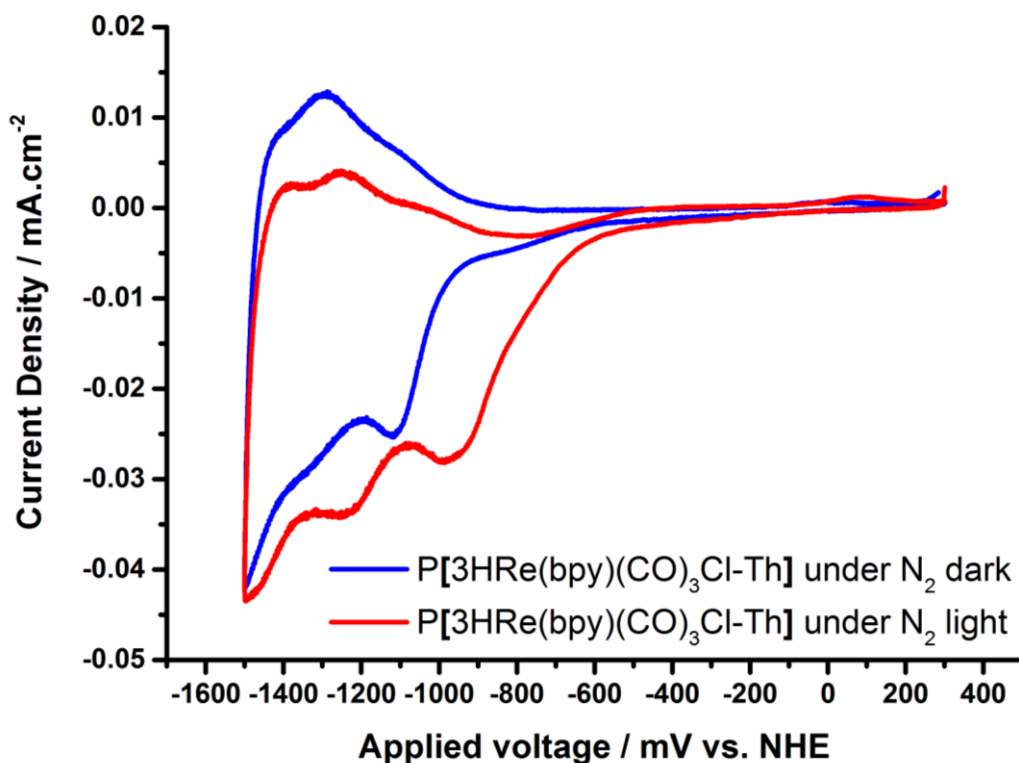


Figure 53. Electrochemical behavior of P[3HRe(bpy)(CO)₃Cl-Th] in dark and under illumination (60 mW/cm²).

The shift in the potential towards more positive values is a characteristic sign of photogenerated charge carriers. Under dark conditions a junction is formed by bringing the electrode into the electrolyte solution. This causes accumulation of charge carriers around the interface which can be expressed by the following formula:

$$n_{\text{carrier at the interface}} = N_{\text{total carrier}} \exp\left(\frac{E_f - E_{\text{redox}}}{KT}\right)$$

where E_f is the Fermi energy level of the semiconductor, E_{redox} is the electrolyte potential forming the junction, and $(E_f - E_{\text{redox}})$ is the magnitude of the contact potential. When electrode surface is illuminated the carrier concentration at the interface is altered by the generation of minority carriers (electrons in this case). As a result of this a new Fermi energy level (E_f^*) is formed. Ideally E_{redox} is not changed since the illumination has no impact on the electrolyte solution. Then we can redefine the equation as:

$$(n_{\text{light}}) - (n_{\text{dark}}) = \{N_{\text{illumn}} - N_{\text{dark}}\} \exp \left[\frac{(E_f^* - E_{\text{redox}}) - (E_f - E_{\text{redox}})}{KT} \right]$$

where n_{light} and n_{dark} is the total carrier concentration under illumination and in dark, respectively. This difference is equal to the energy gained by the carriers and it can be rewritten as $(E_f^* - E_{\text{redox}}) - (E_f - E_{\text{redox}}) = (E_f^* - E_f)$. With this rearrangement we obtain a much simpler form of both formulas:

$$\delta n = N_c \exp \left(\frac{E_f^* - E_f}{KT} \right)$$

where δn is the number of photogenerated carriers produced at the interface and N_c is the difference in the total concentration of all carriers generated within in the system. The magnitude $(E_f^* - E_f)$ is the magnitude of the photopotential originating from the illumination of the interface. In other words, this magnitude is equal to the change in the contact potential of the junction⁸⁴.

This phenomenon allows one to use a p-type semiconductor in an n-type process like CO₂ reduction. Vice versa is also true for n-type semiconductors and p-type electrochemical processes.

The working principle can be explained as follows: The illumination leads to the formation of an electron-hole pair, also known as exciton. The exciton then travels to the electrode-electrolyte interface in ideal case (or can recombine non-radiatively). When the driving force is strong enough, the exciton dissociates allowing electrons to be transferred to the catalyst to initiate / facilitate reduction of carbon dioxide. The remaining hole is then recombined with the electrons from the negatively biased electrons (**Figure 54**).

To assess the electrochemical activity of P[3HRe(bpy)(CO)₃Cl-Th] towards CO₂ the electrode covered with polymer film was immersed in 0.1M TBAPF₆ solution in acetonitrile. The electrochemical cell used in catalytic experiments was in H-Cell configuration to prevent the re-oxidation of products evolved in cathode chamber. An Ag/AgCl quasi-reference electrode was immersed alongside the polymer electrode (working electrode) in the cathode chamber. Pt plate was used as counter electrode in the anode chamber. Both chambers were sealed with air-tight caps having a septum in the middle allowing gas purging. The chambers of the H-Cell were purged with N₂ with a flow rate of 0.2 L/min for 45minutes to make sure that there is no residual oxygen.

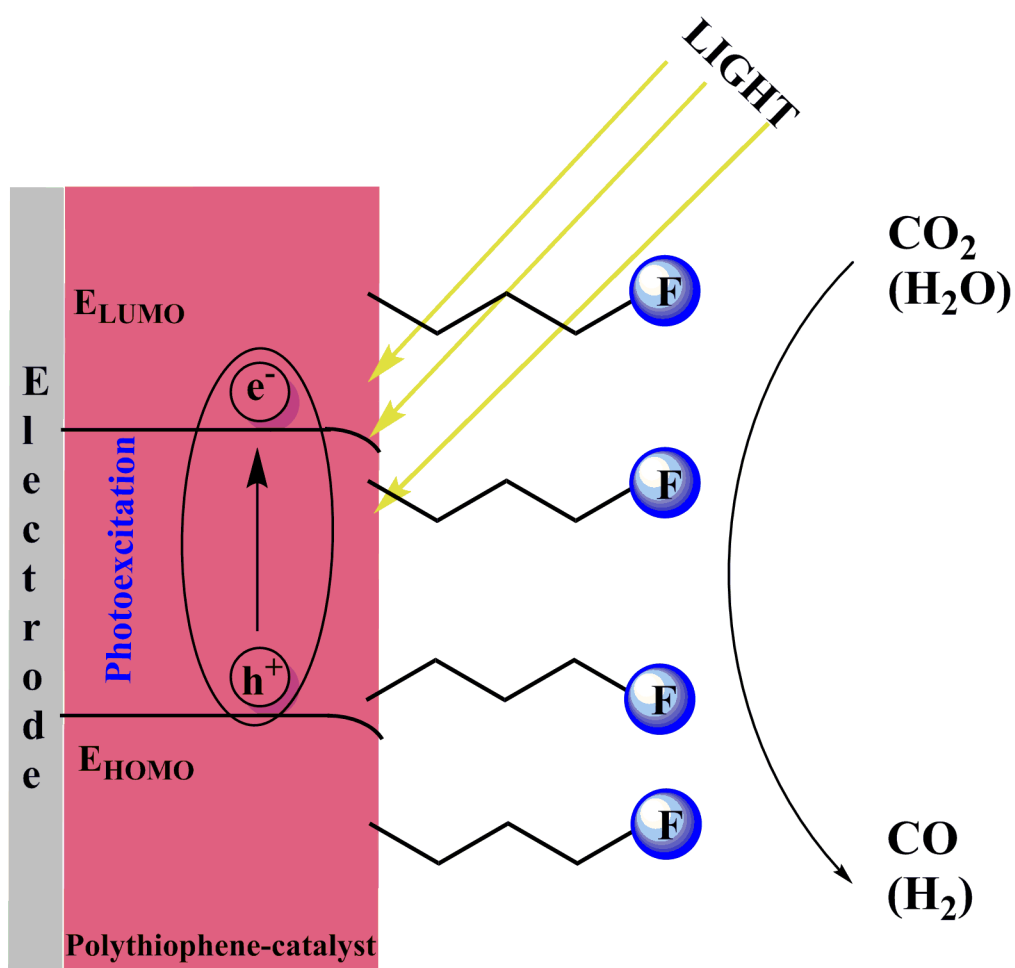


Figure 54. Working principle of the polymeric catalyst upon irradiation with light. H_2 can also be observed as a product when the electrolyte medium is protic.

When the electrolyte solution was purged with CO_2 for 45min with the same flow rate and cyclic voltammetry was recorded, an increase in current followed by a crossing in the curve was observed (**Figure 55**). These are the characteristic signs of electrochemical reduction of carbon dioxide^{157,158}.

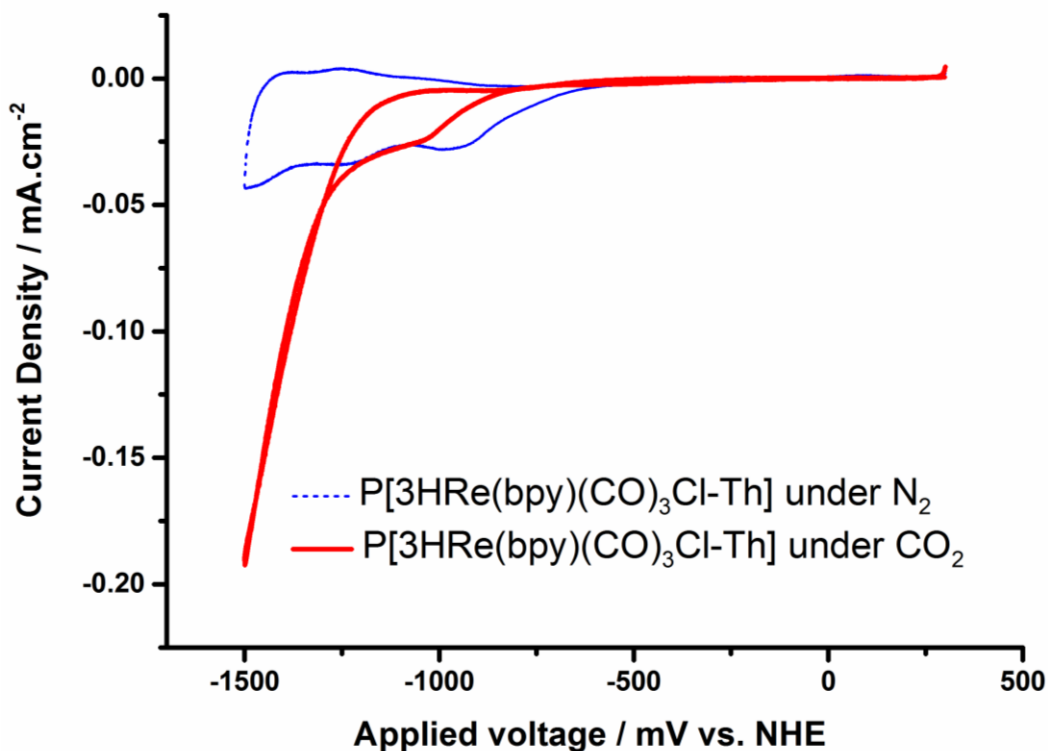


Figure 55. Current increase upon the saturation of electrolyte solution with CO₂

Finally, a constant potential electrolysis was conducted to assess the performance of the polymer electrode as catalyst. Electrolysis was conducted at -1500 mV vs. NHE for 2 hours and the products were analyzed using the gas chromatography. Lehn's catalyst is known to produce CO as the main product with a faradaic efficiency reaching unity⁶⁰. In this case, the faradaic efficiency was calculated as 2.5 %¹⁵⁹. This is indeed far from ideal, however this process shows that a functional side chain, when electronically decoupled from the π -system, can act as a catalyst and this method can be adapted to other catalytically active functional groups to transform them into heterogeneous catalysts.

P[3HPyr-Th] was also investigated for its catalytic activity. To this end, the electrode was dipped into 0.5 M KCl solution in water where the pH is adjusted to 5.5 in order to obtain pyridinium ion (protonated form of pyridine) functionalized polymer^{148,149}. No catalytic activity was observed in dark or under illumination in N₂ and CO₂-saturated conditions which indicates that the pyridine functional group is either not addressable or not active in the given potential window. The CV curves show similar behavior under N₂ and CO₂-saturated conditions with a current difference < 1 $\mu\text{A cm}^{-2}$ (**Figure 56**). This might originate from the change in the ionic strength of the solution upon purging with carbon dioxide. This supports the idea of pyridinium ion being an electron shuttle for driving the electrochemical reduction of CO₂ to methanol and heterogeneous approaches to this end is not profitable.

Our group also conducted research on the reproducibility of said pyridinium-catalyzed CO₂ reduction to methanol and investigated the effect of nitrogen atoms in the aromatic cycle¹⁶⁰.

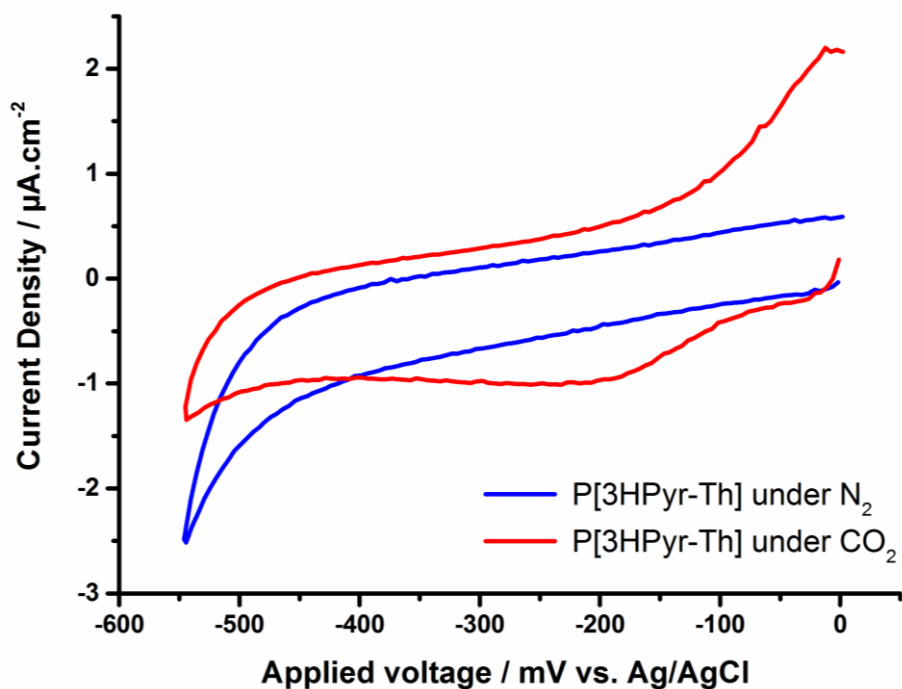


Figure 56. Electrochemical behavior of P[3HPyr-Th] under N_2 and CO_2 -saturated conditions upon illumination.

3.2.2. Photoelectrochemical Reduction of O_2

Here a photocathode comprised of a porphyrin derivative, 5-(4-carboxyphenyl)-10,15,20-triphenylporphyrinatocopper(II) (CuTPP-COOH), (**Figure 57**) coated on titanium dioxide nanotube arrays (TiO_2 NTs) is presented to drive the reduction of O_2 to H_2O_2 .

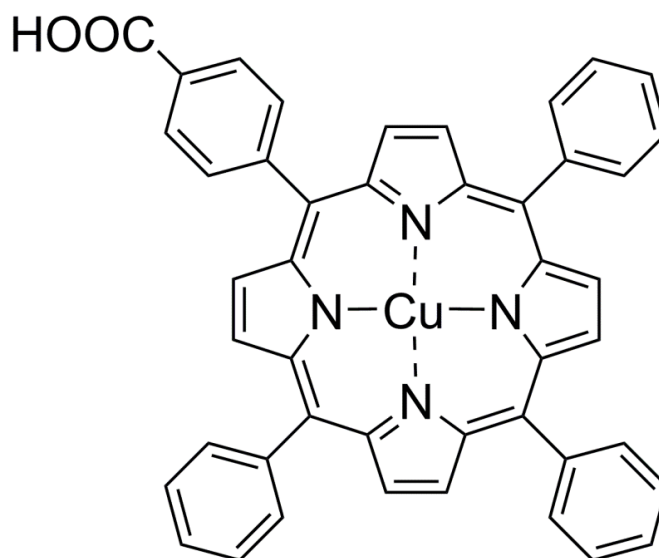


Figure 57. Chemical structure of CuTPP-COOH.

The carboxylic acid moiety enables the anchoring of photoactive porphyrin structure onto TiO₂ NTs¹⁶¹. CuTPP-COOH was chosen due to its suitable energy levels aligning with energy needed to reduce O₂ to H₂O₂ as well as its ease of synthesis. The molecule was kindly provided by my colleague, Assoc. Prof. Patchanita Thamyongkit at Chulalongkorn University in Thailand. The synthetic procedure can be seen **Scheme 2**.

The high surface area of TiO₂ NTs¹⁶² is beneficial for addressing many catalytically active sites. Also amorphous structure helps the attachment of CuTPP-COOH.

TiO₂ NTs bearing electrodes were prepared and provided by my colleague Dr. Engelbert Portenkircher at University of Innsbruck. The procedure for preparation of the electrodes can be found in literature¹⁶².

1 mg of CuTPP-COOH was dissolved in 500 μL of THF and then drop-casted on the TiO₂ NTs bearing electrodes. After drying the electrode looked pale brown (**Figure 58**).

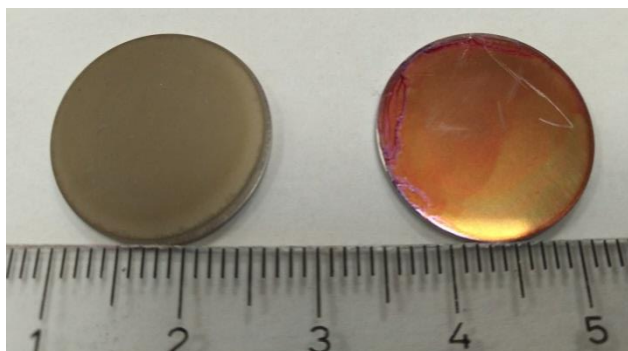
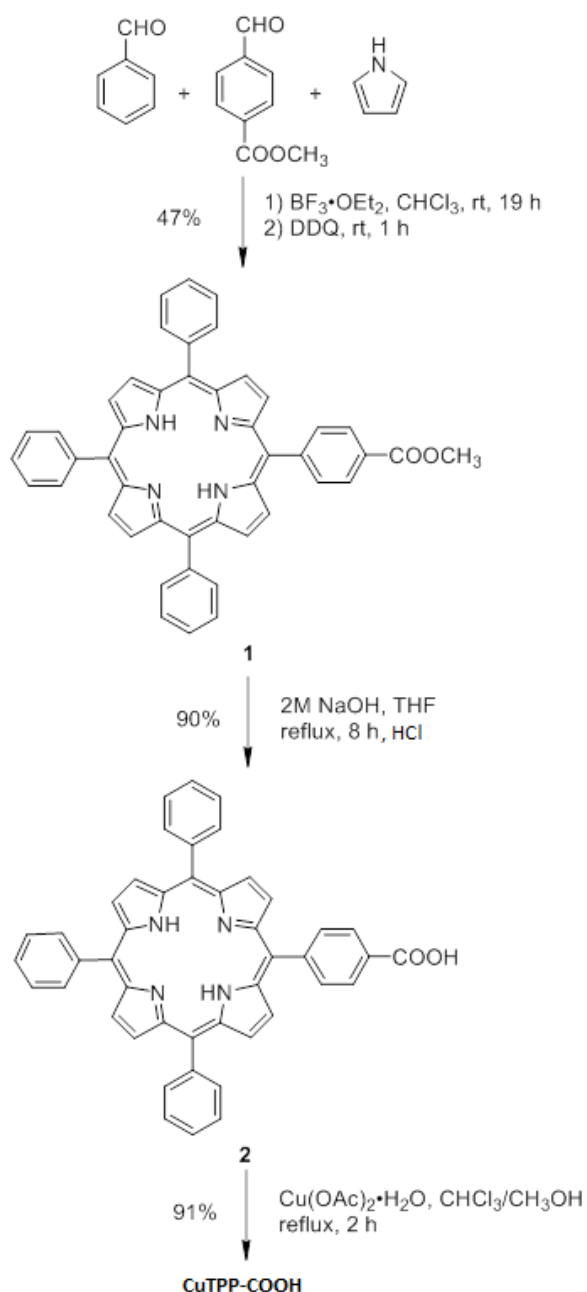


Figure 58. TiO₂ NTs bearing electrode before (on the left) and after coating with CuTPP-COOH (on the right).



Scheme 2. Synthetic pathway for CuTPP-COOH

SEM images of the electrodes were also taken prior to coating and afterwards. It can be seen from the images that the nanotubes have an average diameter of ~100 nm. Upon coating the surface with CuTPP-COOH a thin layer was formed indicating the coverage of the surface (**Figure 59**).

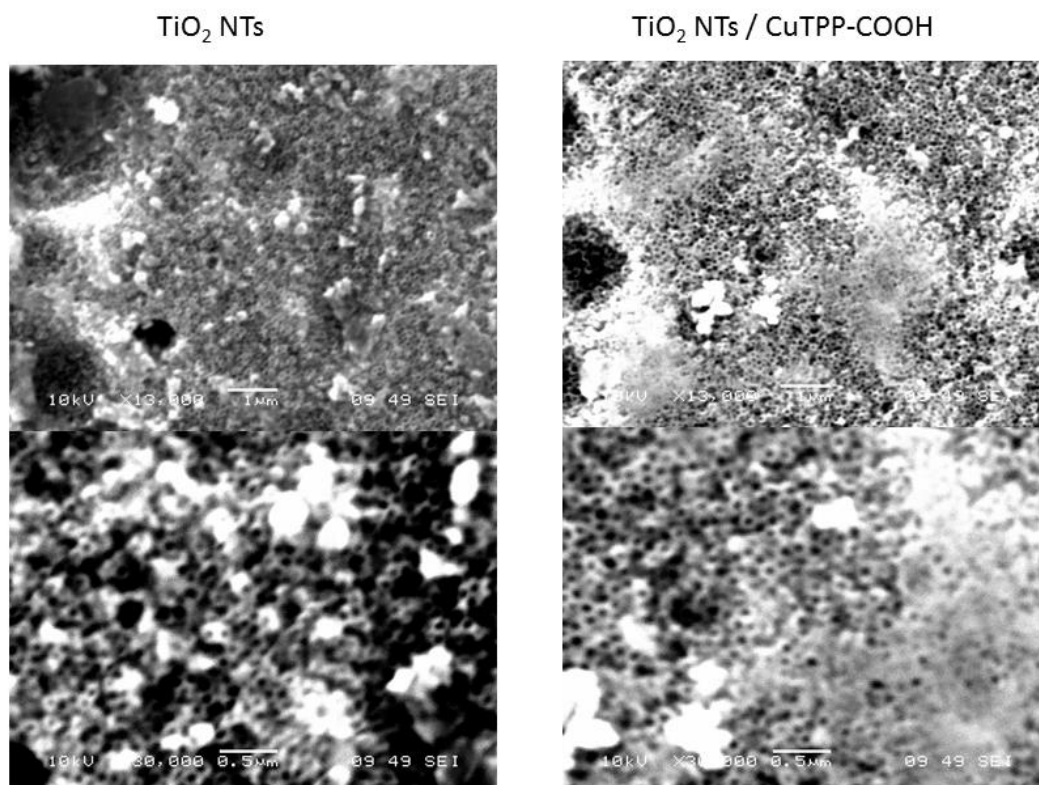


Figure 59. SEM images of TiO₂ NTs (on the left) and CuTPP-COOH coated TiO₂ NTs (on the right).

To make sure that the CuTPP-COOH is covalently bound on the surface an ATR-FTIR measurement was conducted where the disk electrodes were pressed on diamond reflection element and the measurement was conducted in ATR mode.

$-\Delta T/T$ corresponds to the absorption calculated from the ATR mode of FTIR. Spectrum below is calculated by taking the TiO₂ NTs as the baseline hence eliminating all the features which may arise from the bare electrode. In this case the peaks pointing upwards corresponds the evolving features and the peaks pointing downwards correspond to the peaks disappearing. The peak around 1685 cm⁻¹ corresponds to the ketone formed by anchoring of -COOH to the surface oxide. The peak at 1342 cm⁻¹ is indicating the aromatic C-N stretching.

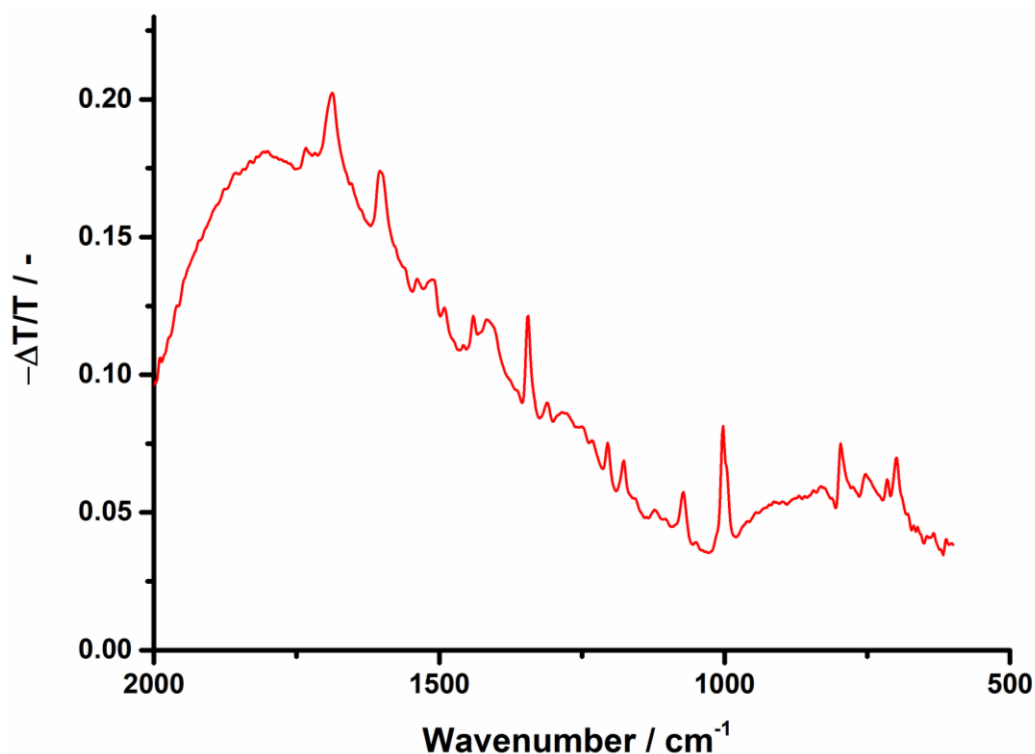


Figure 60. ATR-FTIR spectrum of the electrode TiO₂ NTs / CuTPP-COOH.

These peak assignments are in accordance with the structures reported in the literature¹⁶¹.

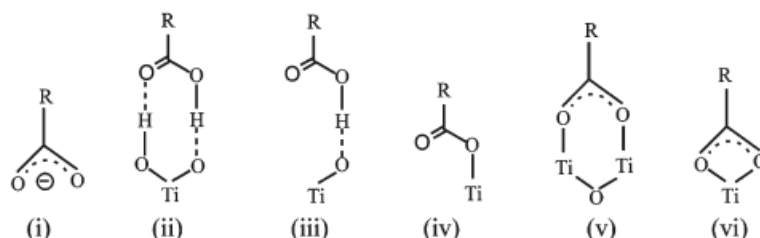


Figure 61. Possible binding modes of -COOH group on TiO₂. (Reproduced with permission)

However, certain configuration of the bonding is hard to pin down at this stage. The covalent nature of the bonding can also be deduced from the observation that upon vigorous washing with organic solvents like Toluene and THF it is not possible to remove the film from the surface.

After characterization of the electrode a series of chronoamperometric experiments were conducted to assess the activity of the electrode towards oxygen reduction in dark and under illumination. Electrode was immersed into an electrochemical cell equipped with a three-electrode setup. TiO₂ NTs / CuTPP-COOH served as the working electrode while an Ag/AgCl (3.5 M KCl) used as reference and a Pt plate was utilized as the counter electrode in 0.1 M Na₂SO₄ solution in water at pH 7.

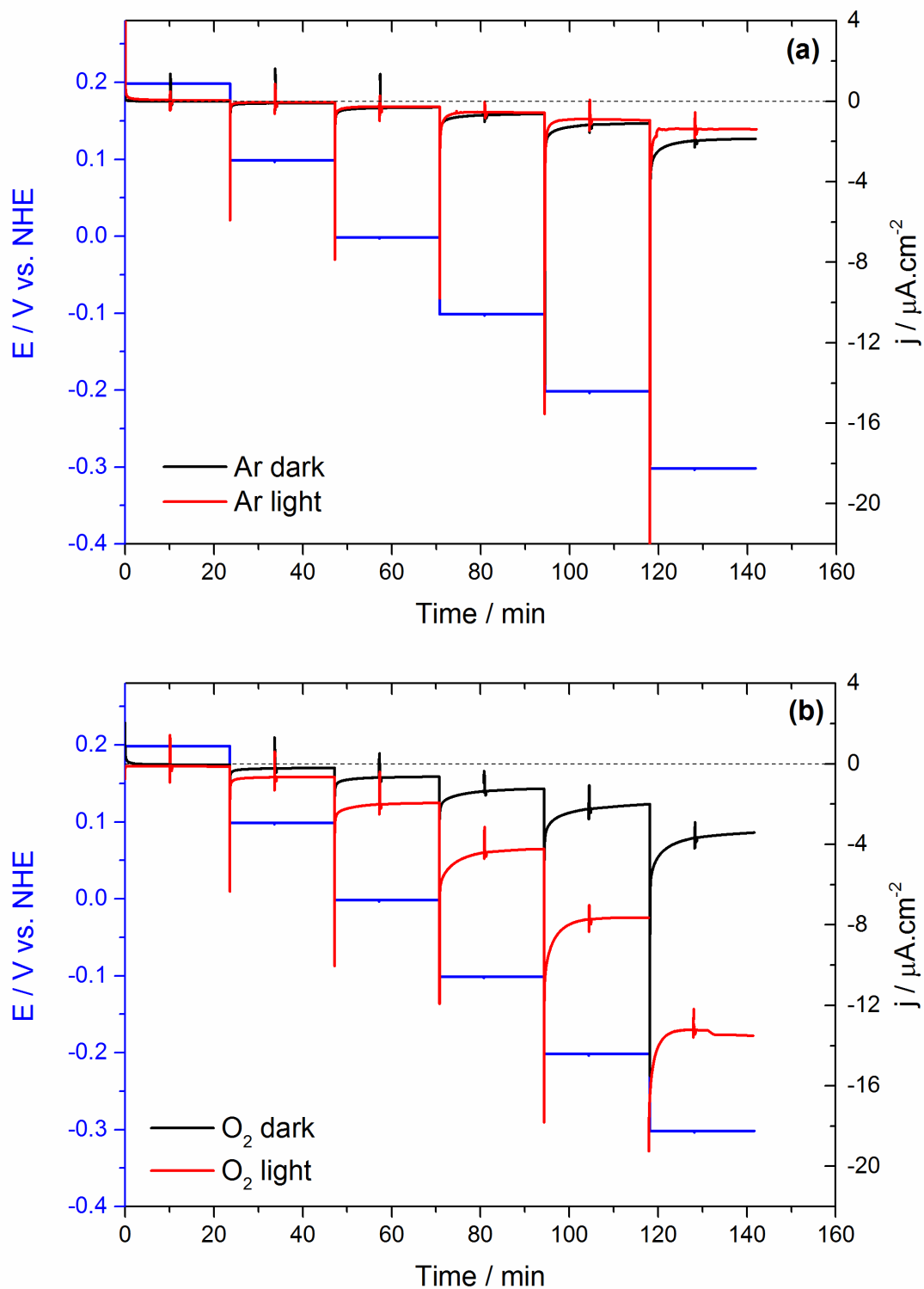


Figure 62. Chronoamperometry experiments conducted on TiO_2 NTs / CuTPP-COOH under Argon (a) and under O_2 -saturated conditions.

Above figure shows the current behavior of the electrode under certain potentials (from 0.2 V to -0.3 V vs. NHE). Under Ar-saturated conditions the illumination does not induce a recognizable

current increase. When the solution was saturated with O₂ by purging it for 10 min the illumination induced a 4-fold current increase. The current density under illuminated conditions reached a maximum of 13 μA cm⁻² at -0.3 V implying the reduction of dissolved O₂. Each potential step was applied for 20 min in order to maintain the steady state. This also shows the stability of the electrode itself in photoelectrochemical operation conditions.

After chronoamperometry experiments, a series of constant potential electrolysis experiments was carried out in order to enhance the formation of H₂O₂ and its quantification. One of the efficient and rapid ways for detection of hydrogen peroxide is the indirect spectrophotometric quantification method. This method relies on stoichiometric reaction of arylboronic acids with H₂O₂ under mildly basic conditions to yield the respective photoactive phenolates^{163,164}. To this end, *p*-nitrophenylboronic acid (*p*-NPBA) was utilized in a solution with pH 9, where with the help of H₂O₂, it is converted to *p*-nitrophenol (*p*-NP). The absorption of *p*-NP can be observed with UV-Vis spectrophotometry at 405 nm. The amount of H₂O₂ in the reaction vessel can then be determined using a calibration curve.

In this study, a calibration curve for quantitative determination of H₂O₂ evolved during the photoelectrochemical reduction of O₂ was used. The calibration curve ranged from 0.5 μM to 20 μM.

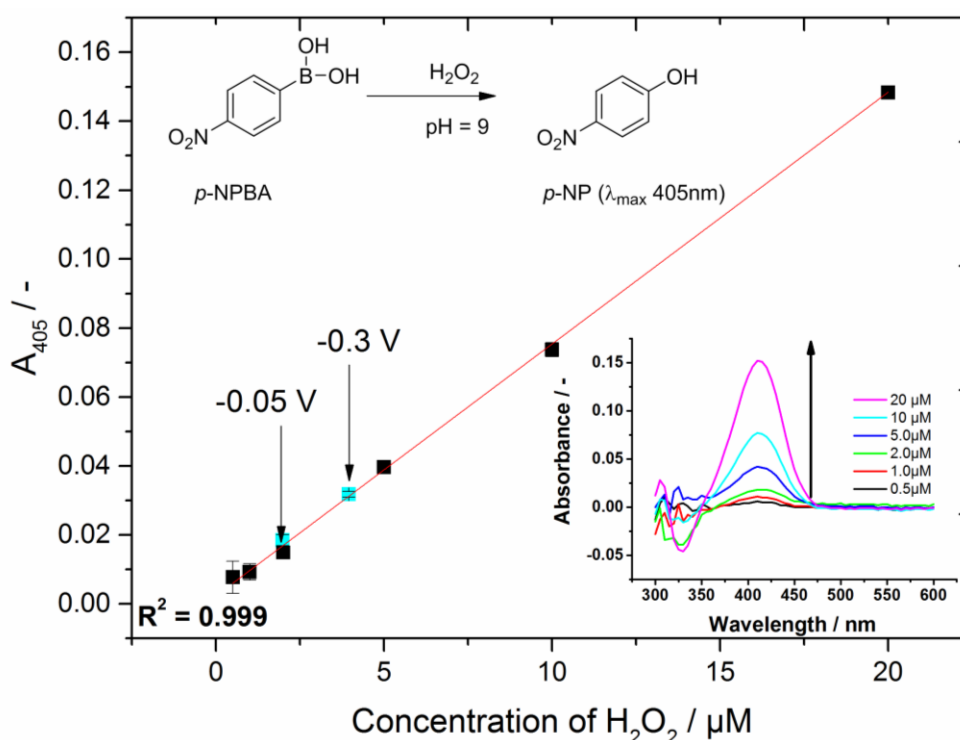


Figure 63. Calibration curve used for quantifying the produced H₂O₂. Reaction leading to *p*-NP formation (upper left inset). Increase in absorbance with increasing concentration of H₂O₂ (lower right inset). Points with turquoise color are the concentrations of H₂O₂ obtained from electrolysis at constant potentials of -0.05 V and -0.3 V vs. NHE.

At the end of each constant potential electrolysis experiment, an aliquot of 100 μL was taken from the electrochemical cell and then added into a vial containing the *p*-NPBA and carbonate buffer (to maintain a pH value of 9). Concentrations ranging from 1.9 μM to 3.9 μM were obtained for potentials -0.05 V and -0.3 V respectively. The figure of merit for the comparison of hydrogen peroxide formation catalysts is the formation rate which is given in $\mu\text{g H}_2\text{O}_2 / \text{mg catalyst} / \text{h}$. CuTPP-COOH supported on TiO_2 NTs achieved formation rates of 2.2 $\mu\text{g H}_2\text{O}_2 / \text{mg catalyst} / \text{h}$ and 13.4 $\mu\text{g H}_2\text{O}_2 / \text{mg catalyst} / \text{h}$ for the applied potentials of -0.05 V and -0.3 V, respectively. This system is comparable to well-known semiconductors like ZnO (21 $\mu\text{g} / \text{mg ZnO} / \text{h}$) and g- C_3N_4 (4.25 $\mu\text{g} / \text{mg g-C}_3\text{N}_4 / \text{h}$)^{54,55}.

To gain more insights in the electrochemical characteristics of the electrode, potential-dependent electrochemical impedance spectroscopy (PEIS) was conducted. The spectra were recorded in the same potential range as the chronoamperometry measurements with a step size of 0.1 V. Each potential was kept constant to maintain steady-state conditions prior to the impedance measurements. The frequency range varied from 100 kHz to 20 mHz with a peak amplitude of ± 10 mV. Two sets of measurements were carried out under Ar and O_2 -saturated solutions in dark and under illumination.

Detailed analysis of Nyquist plots under O_2 -rich conditions shows the presence of three, not fully developed semi-circles. The first semi-circle (I) at high frequencies between 4.5 kHz and 200 Hz was observable in all spectra and may describe the interfacial $\text{TiO}_2/\text{CuTPP-COOH}$ charge transfer. A second semi-circle (II) at medium frequencies between 65 Hz and 1.4 Hz is also observable in all spectra and may represent the resistance for electron transport along the TiO_2 NTs and the corresponding surface capacitance¹⁶⁵. The development of an additional semi-circle (III) at potentials below 0.0 V and lower frequencies between 0.94 Hz and 20 mHz is observable only when the electrolyte is saturated with O_2 . This may correspond to the charge transfer resistance of the O_2 reduction reaction. A two-step reaction process is expected to be the reason for the occurrence of semi-circle (III), for example an intermediate state that is involved¹⁶⁶.

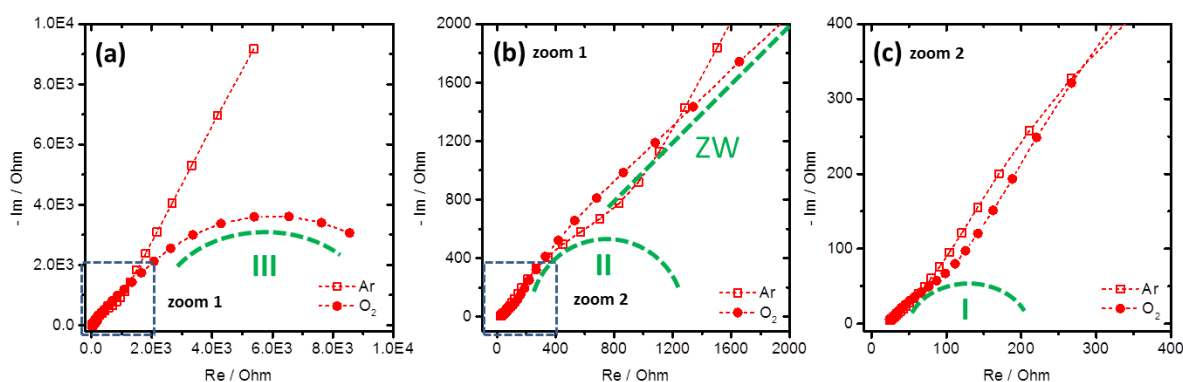


Figure 64. Nyquist plots for illuminated, porphyrin covered TiO_2 NTs at -0.2 V vs. NHE under Ar (squares) and O_2 (circles) saturation in 0.1 M Na_2SO_4 . Symbols represent the experimental data and the dashed lines are only a guide for the eye with no physical meaning. (a) Illustration of the semi-circle (III) at low frequencies between 0.94 Hz and 20 mHz, which is only observable when the electrolyte is saturated with O_2 , (b) magnification of the high frequency domain in (a), highlighted with the blue dashed square, to illustrate the second semi-circle (II) at medium frequencies between 65 Hz and 1.4 Hz; The finite length Warburg impedance (ZW) under O_2 (circles) saturation is indicated by a

green dashed line with a slope of 45°. (c) Magnification of the high frequency domain in (b), highlighted with the blue dashed square therein, to illustrate the onset of semi-circle (I) at high frequencies between 4.5 kHz and 200 Hz.

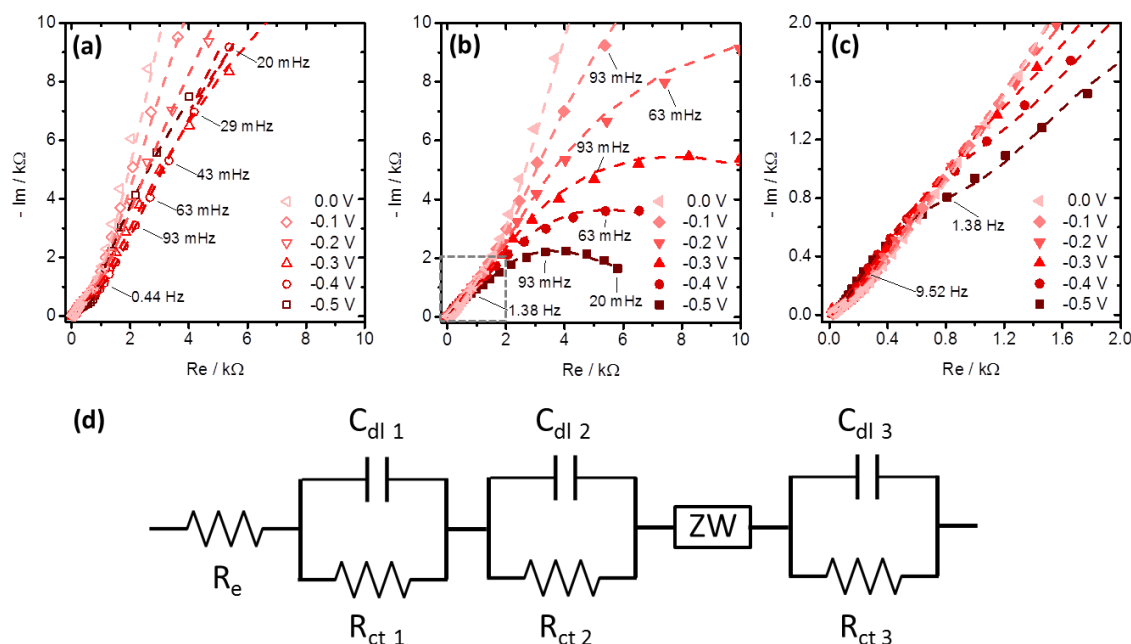


Figure 65. Nyquist plots at different potentials for TiO₂ NTs / CuTPP-COOH electrode (illuminated) under (a) Ar and (b) O₂-saturated conditions. Symbols represent the experimental data and the lines the best fit. (c) Enlarged view of the high frequency domain of (b) indicated therein with a grey, dashed square. (d) Equivalent electric circuit used for fitting the EIS data. R_s : solution resistance, R_f and C_f : interfacial TiO₂ NTs / CuTPP-COOH electron charge transfer resistance and the corresponding capacitance, R_{tr} and CPE_{nt} : resistance for electron transport along the TiO₂ NTs and the corresponding capacitance (modelled with a CPE), ZW : Warburg element for semi-infinite diffusion, R_r and CPE_r : charge transfer resistance for the O₂ reduction and corresponding capacitance (modelled with a CPE).

For further understanding of the EIS data, corresponding electronic elements were determined by fitting the experimental spectra to the proposed equivalent circuit depicted in the above figure part d. The equivalent circuit proposed here is a modified version of the equivalent circuit reported by Köleli *et.al.* for CO₂ reduction on polyaniline-coated electrodes¹⁶⁶. At high frequencies an additional R/C element was added to account for nanotube-porphyrin interface. This was partly adopted from the transmission line model which was originally introduced for nanostructured TiO₂ hybrid solar cells¹⁶⁵. The real capacitors C_{nt} and C_r were used with CPEs in modeling to account for the non-ideal behavior, that is depressed semi-circle, of the capacitive part at medium and low frequencies¹⁶⁷. The finite length Warburg impedance ZW was used to describe the transport of O₂ into the CuTPP-COOH film and the transport of reduction products (*i.e.* H₂O₂) out of the film. The parallel configuration of the R_{tr} / CPE_{nt} and R_r / CPE_r elements might be rationalized due to the porosity of the porphyrin covered TiO₂ NTs. It can be concluded from EIS that the R_s is almost constant at all potentials, fluctuating slightly between 17 and 20 Ω. The R_f was relatively high at positive potentials with 111.6 kΩ at 0.2 V and decreased significantly to 3.1 kΩ at -0.3 V. This signals the enhanced charge transfer over the TiO₂ NTs / CuTPP-COOH interface with increasing negative potentials. The resistance for electron transport along the TiO₂ NTs, R_{tr} , decreased slightly upon applied potential from 2.4 kΩ at 0.2 V to 158 Ω at -0.3 V. It was not possible to determine the charge transfer resistance related to the ORR (R_r) at positive potentials of 0.2 V and 0.1 V, respectively. This is due to the corresponding

non-developed semi-circle within the measured frequency limit (20 mHz). Accordingly, it was reasonable to fit the EIS data at 0.2 V and 0.1 V without using the electronic elements (ZW , R_r and CPE_r) for describing the O_2 and ORR. At 0.0 V the semicircle (III) became detectable and R_r was determined as 214 k Ω . R_r then decreased significantly to about 2.3 k Ω at - 0.3 V, suggesting enhanced ORR at lower potentials. This is in agreement with the observed characteristics from chronoamperometry experiments. In long term explanation the proposed equivalent circuit might not be ideal and may not adhere well with the complexity of the system investigated here. It was introduced only to give an initial explanation to describe the EIS data. It is also important to point out that the EIS measurements were not performed under diffusion controlled conditions (i.e. by a rotating disk electrode). This further makes the interpretation challenging. Nevertheless, the proposed equivalent circuit yielded a good fitting in the Nyquist and Bode plots (**Figure 65** and **Figure 66**).

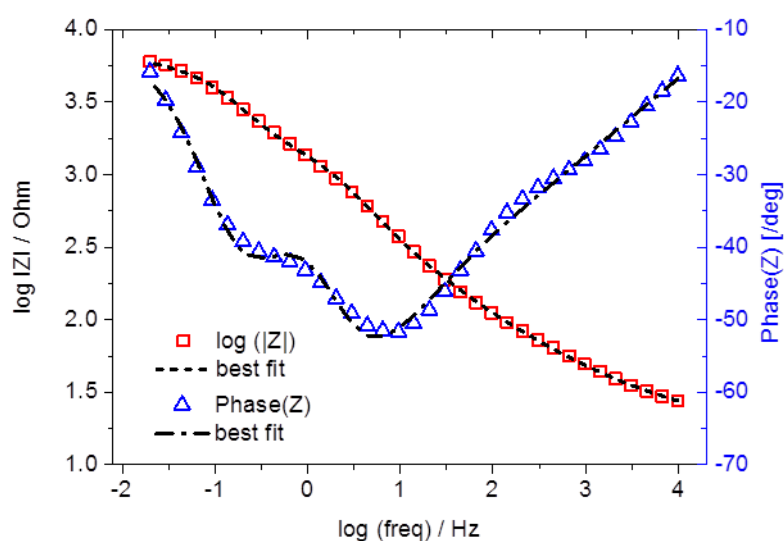


Figure 66. Bode plot at -0.3 V vs. NHE for illuminated, porphyrin covered TiO₂ NTs under O₂-saturated conditions. Symbols represent the experimental data and the dashed lines the corresponding best fit in the frequency range from 10 kHz to 20 mHz.

4. Conclusions and Outlook

4.1. Conclusions

This thesis aimed to utilize organic semiconductors as a new class of materials for catalytic applications with the aim of “saving” them from their long time belief of being unstable and inefficient.

All of the catalytically chemical compounds used in this thesis namely, polythiophene, Lehn’s catalyst, copper porphyrin, indigo, quinacridone and naphthalenebisimide are like “usual suspects” in a well-known movie. They are well-known in their own fields like organic chemistry, conducting polymers, vat-dyeing but there was a little crossing of borders. This thesis aimed to bring different fields together to introduce a synergistic approach to an existing, well-known problem of depletion of carbon-based fuels.

Heterogeneous approaches were the driving force of this thesis since homogeneous approaches lack advantages require the relocation of electrochemically/photochemically or photoelectrochemically-activated catalyst to the molecule of interest. Heterogeneous catalysis eliminates this step, which is prolific to side reactions and inhibition mechanisms, by activating the catalyst directly on the surface. In such case only the molecule of interest (CO_2 or O_2 in the case of this study) needs to travel to the electrode surface.

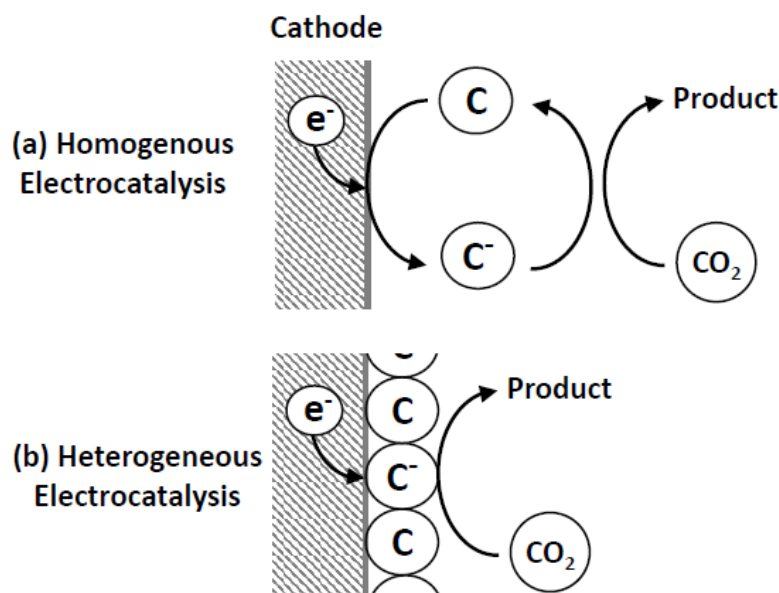


Figure 67. Homogeneous vs. Heterogeneous catalysis.

Another which drove this thesis is the need for realizing such reactions in energy-efficient and eco-friendly conditions. Many reactions mentioned in this thesis, especially industrial techniques for CO_2 capturing, require high temperatures and pressures to be efficient or even to be activated for that matter. As the climate change is affecting our daily lives solutions where less carbon-based energy sources are used are of essence. Maybe total reduction in the use of fossil fuels is a far away dream but achieving a carbon-neutral cycle is not improbable (keeping the

thermodynamic constraints in mind). Such cycle can only be achieved if the driving force behind the catalytic reactions is renewable energy forces like wind and solar energy.

With these motivations in mind the first chapter of investigates the catalytic abilities of a modified polythiophene derivative namely, P[3HRe(bpy)(CO)₃Cl-Th] for photoelectrochemical reduction of carbon dioxide. The molecule without having a direct conjugation to the catalytically active part seems to be improbable to work at a first glance but experiments showed that the addressing of the Lehn's catalyst attached to polythiophene backbone is possible. The catalytic reaction takes place in much lower potential of -1.5 V vs. NHE¹⁵⁹ compared to its homogeneous counterpart which takes place at a potential of -1.8 V vs. NHE⁹⁰. However, the method suffers from low faradaic yields which might be improved by direct conjugation of the catalytically active part to the p-type backbone as reported previously^{113,168}.

The second part of the first chapter continues with another known molecule, copper porphyrin. In this study, a carboxylic acid-modified copper porphyrin was fixed on nanostructured TiO₂ as a catalytically active species for O₂ reduction. The electrode is resistant to solvents and electrochemical treatment once it is attached covalently into the TiO₂ NTs and onto the surface which makes enables its repetitive use. This study tackles another problem of ORR which is the harsh reaction conditions. ORR works best in acidic or basic conditions. 2-electron reduction of oxygen in acidic conditions leads to the formation of H₂O₂ which is an important molecule for plethora of reactions. CuTPP-COOH catalyst supported on TiO₂ NTs achieved a ORR reaction rate of 13.4 μg_{H₂O₂} / g_{CuTPP-COOH} / h which is comparable to well established ZnO (~21 μg_{H₂O₂} / g_{ZnO} / h)¹⁶⁹ and is better than another well-established catalyst g-C₃N₄ (~4 μg_{H₂O₂} / g_{gC₃N₄} / h)^{54,55}.

The second chapter of the thesis focuses on a more fundamental problem of fixation of carbon dioxide on the surface. This goes one step further than heterogeneous catalysis and aims to bring the target molecule CO₂ closer to the electrode surface by anchoring it. This opens another avenue by breaking the linear symmetry of carbon dioxide and changing its hybridization from sp to sp² and activating it chemically. For this purpose H-bonded carbonyl pigment family member Quinacridone was coated on a glass ITO electrodes to capture and release carbon dioxide electrochemically. Electrochemical capture and release of carbon dioxide is significant because existing techniques require either temperature or pressure swinging to release the captured CO₂ as well as capture it. Quinacridone achieves this task at moderately negative potentials between -1.7 to -1.8 V vs. Fc/Fc⁺ with an uptake capacity of 4.6 mmol CO₂ / g QNC which is very close to its industrial counterpart monoethanolamine (8 mmol CO₂ / g)¹²⁴. QNC is able to hold on to the captured carbon dioxide for hours and releasing can be achieved by simply oxidizing the molecule. However, this process was achieved in an organic solvent, acetonitrile, which might not be suitable for daily industrial applications. For that reason a naphthalene bisimide derivative was designed to operate in aqueous environments. The molecule NBIT was equipped with electron-deficient units in order to lower the reduction potential while alkyl side chains introduced resistance to solubility in water. NBIT showed an uptake capacity of 2.3 mmol CO₂ / g NBIT in water at pH 7 under ambient temperature and pressure which makes it one and only of its kind. Furthermore, the mechanism behind the process was proved by employing the powerful technique of *in-situ* ATR-FTIR spectroelectrochemistry. Further studies focused on the reduction of captured carbon dioxide to higher hydrocarbons but it seems that addressing of captured carbon dioxide on the surface is not possible at this moment.

4.2. Outlook

Over the course of this thesis many different techniques, experiences and experiments showed that yet another synergetic approach is necessary for furthering the electrochemical catalytic applications of organic semiconductors and that is the synergy of organic semiconductors and biological molecules. Except the few examples set by the very few researchers in the community where the enzymes are immobilized on electrodes to address the bioelectrochemical reduction of carbon dioxide¹⁷⁰⁻¹⁷³, the field of bioelectrochemical catalysis requires a mediator to address the biocatalyst⁸⁸. Nature always uses electron shuttles while addressing its bioactive catalysts. Conjugated organic semiconductors can play the role of being the electroactive (as it is evident by this thesis and many other studies) molecule and the host for biocatalysts like enzymes, proteins, bacteria etc. the biomolecules can drive the selective catalytic reactions. Organic nature of the conjugated semiconductors will allow the biomolecules to be hosted on the surface via covalent bonding or intermolecular interactions like H-bonding or Van der Waals interactions and will facilitate the transfer of electrons through their backbone to the biological catalysts. This can be both electrochemical, photochemical or photoelectrochemical. This is an apparent need of the field of catalysis.

5. References

- (1) Baede, A.; van der Linden, P.; Verbruggen, A. *Annex to IPCC Fourth Assessment Report*; 2007.
- (2) Treut, L.; Somerville, R.; Cubasch, U.; Ding, Y.; Mauritzen, C.; Mokssit, a; Peterson, T.; Prather, M.; Qin, D.; Manning, M.; Chen, Z.; Marquis, M.; Averyt, K. B.; Tignor, M. Historical Overview of Climate Change Science. *Earth* **2007**, *Chapter 1* (October), 93–127.
- (3) EPA. Climate Change <https://www.epa.gov/climate-indicators/climate-change-indicators-atmospheric-concentrations-greenhouse-gases>.
- (4) Aresta, M.; Dibenedetto, A. Utilisation of CO₂ as a Chemical Feedstock: Opportunities and Challenges. *Dalton transactions (Cambridge, England : 2003)* **2007**, No. 28, 2975–2992.
- (5) Müller, K.; Mokrushina, L.; Arlt, W. Thermodynamic Constraints for the Utilization of CO₂. *Chemie-Ingenieur-Technik* **2014**, *86* (4), 497–503.
- (6) Appel, A. M.; Bercaw, J. E.; Bocarsly, A. B.; Dobbek, H.; Dubois, D. L.; Dupuis, M.; Ferry, J. G.; Fujita, E.; Hille, R.; Kenis, P. J. A.; Kerfeld, C. A.; Morris, R. H.; Peden, C. H. F.; Portis, A. R.; Ragsdale, S. W.; Rauchfuss, T. B.; Reek, J. N. H.; Seefeldt, L. C.; Thauer, R. K.; Waldrop, G. L. Frontiers, Opportunities, and Challenges in Biochemical and Chemical Catalysis of CO₂ Fixation. *Chemical Reviews* **2013**, *113* (8), 6621–6658.
- (7) Pegis, M. L.; Roberts, J. A. S.; Wasylenko, D. J.; Mader, E. A.; Appel, A. M.; Mayer, J. M. Standard Reduction Potentials for Oxygen and Carbon Dioxide Couples in Acetonitrile and N,N-Dimethylformamide. *Inorganic Chemistry* **2015**, *54* (24), 11883–11888.
- (8) Metz, B.; Davidson, O.; de Coninck, H.; Loos, M.; Meyer, L. *Carbon Dioxide Capture and Storage*; 2005.
- (9) Sanz-Perez, E. S.; Murdock, C. R.; Didas, S. A.; Jones, C. W. Direct Capture of CO₂ from Ambient Air. *Chemical Reviews* **2016**, *116* (19), 11840–11876.
- (10) Goor, G.; Glenneberg, J.; Jacobi, S. *Ullman's Encyclopedia of Industrial Chemistry*; Wiley-VCH, 2012.
- (11) Weissermel, K.; Arpe, H. J. *Industrial Organic Chemistry*, 4th ed.; Wiley-VCH: Weinheim, 2003.
- (12) Company, U. A. H. Low cost removal of CO₂ and H₂S from natural and synthesis gas <https://www.uop.com/?document=benfield-process-datasheet&download=1> (accessed Jan 8, 2018).
- (13) D'Alessandro, D. M.; Smit, B.; Long, J. R. Carbon Dioxide Capture: Prospects for New Materials. *Angewandte Chemie - International Edition* **2010**, *49* (35), 6058–6082.
- (14) Rheinhardt, J. H.; Singh, P.; Tarakeshwar, P.; Buttry, D. A. Electrochemical Capture and Release of Carbon Dioxide. *ACS Energy Letters* **2017**, *2* (2), 454–461.
- (15) Meng, L. Y.; Park, S. J. Effect of Heat Treatment on CO₂ Adsorption of KOH-Activated Graphite Nanofibers. *Journal of Colloid and Interface Science* **2010**, *352* (2), 498–503.
- (16) Mishra, A. K.; Ramaprabhu, S. Carbon Dioxide Adsorption in Graphene Sheets Carbon Dioxide Adsorption in Graphene Sheets. *AIP Advances* **2011**, *32152*, 0321521–032156.
- (17) Presser, V.; McDonough, J.; Yeon, S.-H.; Gogotsi, Y. Effect of Pore Size on Carbon Dioxide Sorption by Carbide Derived Carbon. *Energy & Environmental Science* **2011**, *4* (8), 3059–3066.
- (18) Sevilla, M.; Fuertes, A. B. CO₂ Adsorption by Activated Templated Carbons. *Journal of Colloid and Interface Science* **2012**, *366* (1), 147–154.
- (19) Drage, T. C.; Arenillas, A.; Smith, K. M.; Pevida, C.; Piippo, S.; Snape, C. E. Preparation of Carbon Dioxide Adsorbents from the Chemical Activation of Urea–formaldehyde and Melamine–formaldehyde Resins. *Fuel* **2007**, *86*, 22–31.
- (20) Pevida, C.; Drage, T. C.; Snape, C. E. Silica-Templated Melamine–formaldehyde Resin Derived Adsorbents for CO₂ Capture. *Carbon* **2008**, *46* (11), 1464–1474.
- (21) Hao, G.-P.; Li, W.-C.; Qian, D.; Wang, G.-H.; Zhang, W.-P.; Zhang, T.; Wang, A.-Q.; Schüth, F.; Bongard, H.-J.; Lu, A.-H. Structurally Designed Synthesis of Mechanically Stable Poly(benzoxazine-Co-Resol)-Based Porous Carbon Monoliths and Their Application as High-Performance CO₂ Capture Sorbents. *Journal of the American Chemical Society* **2011**, *133* (29), 11378–11388.
- (22) Sumida, K.; Rogow, D. L.; Mason, J. A.; McDonald, T. M.; Bloch, E. D.; Herm, Z. R.; Bae, T. H.; Long, J. R. Carbon Dioxide Capture in Metal-Organic Frameworks. *Chemical*

- Reviews* **2012**, 112 (2), 724–781.
- (23) Bae, Y. S.; Mulfort, K. L.; Frost, H.; Ryan, P.; Punnathanam, S.; Broadbelt, L. J.; Hupp, J. T.; Snurr, R. Q. Separation of CO₂ from CH₄ Using Mixed-Ligand Metal-Organic Frameworks. *Langmuir* **2008**, 24 (16), 8592–8598.
 - (24) Millward, A. R.; Yaghi, O. M. Metal Organic Frameworks with Exceptionally High Capacity for Storage of Carbon Dioxide at Room Temperature. *Journal of the American Chemical Society* **2005**, 127 (51), 17998–17999.
 - (25) Bourrelly, S.; Llewellyn, P. L.; Serre, C.; Millange, F.; Loiseau, T. Different Adsorption Behaviors of Methane and Carbon Dioxide in the Isotypic Nanoporous Metal Terephthalates MIL-53 and MIL-47. **2005**, 13519–13521.
 - (26) Weinberg, N. L.; Kentaro Hoffmann, A.; Reddy, T. B. The Electrochemical Reductive Carboxylation of Benzalaniline in Molten Tetraethyl Ammonium P-Toluenesulfonate. *Tetrahedron Letters* **1971**, 12 (25), 2271–2274.
 - (27) Harada, J.; Sakakibara, Y.; Kunai, A.; Sasaki, K. Electrochemical Carboxylation of A,b-Unsaturated Ketones with Carbon Dioxide. *Bulletin of the Chemical Society of Japan*. 1984, pp 611–612.
 - (28) DuBois, D. L.; Miedaner, A.; Bell, W.; Smart, J. C. *Electrochem. Electrocat. React. Carbon Dioxide*; Sullivan, B. P., Krist, K., Guard, H. E., Eds.; Elsevier B.V.: New, 1993.
 - (29) Scovazzo, P.; Poshusta, J.; DuBois, D.; Koval, C.; Noble, R. Electrochemical Separation and Concentration of 1% Carbon Dioxide from Nitrogen. *Journal of The Electrochemical Society* **2003**, 150 (5), D91.
 - (30) Mizen, M. B.; Wrighton, M. S. Reductive Addition of CO₂ to 9,10-Phenanthrenequinone. *Journal of the Electrochemical Society* **1989**, 136 (4), 941–946.
 - (31) Stern, M. C.; Simeon, F.; Hammer, T.; Landes, H.; Herzog, H. J.; Hatton, T. A. Electrochemically Mediated Separation for Carbon Capture. *Energy Procedia* **2011**, 4, 860–867.
 - (32) Ranjan, R.; Olson, J.; Singh, P.; Lorance, E. D.; Buttry, D. A.; Gould, I. R. Reversible Electrochemical Trapping of Carbon Dioxide Using 4,4'-Bipyridine That Does Not Require Thermal Activation. *Journal of Physical Chemistry Letters* **2015**, 6 (24), 4943–4946.
 - (33) Singh, P.; Rheinhardt, J. H.; Olson, J. Z.; Tarakeshwar, P.; Mujica, V.; Buttry, D. A.; Singh, P.; Rheinhardt, J. H.; Olson, J. Z.; Tarakeshwar, P.; Mujica, V. Electrochemical Capture and Release of Carbon Dioxide Using a Disulfide-Thiocarbonate Redox Cycle Electrochemical Capture and Release of Carbon Dioxide Using a Disulfide-Thiocarbonate Redox Cycle. **2017**.
 - (34) Disselkamp, R. S. Energy Storage Using Aqueous Hydrogen Peroxide. *Energy & Fuels* **2008**, 22 (4), 2771–2774.
 - (35) Wernimont, E.; Ventura, M. Past and Present Uses of Rocket Grade Hydrogen Peroxide. *General Kinetics, LLC ...* **1999**, 1–15.
 - (36) Cervone, A.; Torre, L.; D'Agostino, L.; Musker, A. J.; Roberts, G. T.; Bramanti, C.; Saccoccia, G. Development of Hydrogen Peroxide Monopropellant Rockets. *AIAA/ASME/SAE/ASEE Joint Propulsion Conference & Exhibit* **2006**, 42 (July), 1–11.
 - (37) Military. Performance Specification Sheet. 1968, pp 1–13.
 - (38) Kirchner, J. R. *Kirk-Othmer Encyclopedia of Chemical Technology*, 3rd ed.; Grayson, M., Eckroth, D., Eds.; Wiley, 1979; Vol. 13.
 - (39) Campos-Martin, J. M.; Blanco-Brieva, G.; Fierro, J. L. G. Hydrogen Peroxide Synthesis: An Outlook beyond the Anthraquinone Process. *Angewandte Chemie - International Edition* **2006**, 45 (42), 6962–6984.
 - (40) Bard, A. J.; Faulkner, L. R. *Electrochemical Methods: Fundamentals and Applications, 2nd Edition*, 2nd ed.; Harris, D., Swain, E., Eds.; 2001.
 - (41) Kato, S.; Jung, J.; Suenobu, T.; Fukuzumi, S. Production of Hydrogen Peroxide as a Sustainable Solar Fuel from Water and Dioxygen. *Energy & Environmental Science* **2013**, 6 (12), 3756.
 - (42) Mase, K.; Yoneda, M.; Yamada, Y.; Fukuzumi, S. Seawater Usable for Production and Consumption of Hydrogen Peroxide as a Solar Fuel. *Nature Communications* **2016**, 7 (May), 11470.
 - (43) Mase, K.; Yoneda, M.; Yamada, Y.; Fukuzumi, S. Efficient Photocatalytic Production of Hydrogen Peroxide from Water and Dioxygen with Bismuth Vanadate and a Cobalt(II) Chlorine Complex. *ACS Energy Letters* **2016**, 1 (5), 913–919.
 - (44) Choudhary, V. R.; Sansare, S. D.; Gaikwad, A. G. Direct Oxidation of H₂ to H₂O₂ and Decomposition of H₂O₂ over Oxidized and Reduced Pd-Containing Zeolite Catalysts in

- Acidic Medium. *Catalysis Letters* **2002**, *84* (1–2), 81–87.
- (45) Lunsford, J. H. The Direct Formation of H₂O₂ from H₂ and O₂ over Palladium Catalysts. *Journal of Catalysis* **2003**, *216* (1–2), 455–460.
- (46) Chinta, S.; Lunsford, J. H. A Mechanistic Study of H₂O₂ and H₂O Formation from H₂ and O₂ Catalyzed by Palladium in an Aqueous Medium. *Journal of Catalysis* **2004**, *225* (1), 249–255.
- (47) Landon, P.; Collier, P. J.; Papworth, A. J.; Kiely, J.; Hutchings, G. J. Direct Formation of Hydrogen Peroxide from H₂ / O₂ Using a Gold Catalyst. *Chemical Communications* **2002**, 2058–2059.
- (48) Li, G.; Edwards, J.; Carley, A. F.; Hutchings, G. J. Direct Synthesis of Hydrogen Peroxide from H₂ and O₂ and in Situ Oxidation Using Zeolite-Supported Catalysts. *Catalysis Communications* **2007**, *8* (3), 247–250.
- (49) Yi, Y.; Wang, L.; Li, G.; Guo, H. A Review on Research Progress in the Direct Synthesis of Hydrogen Peroxide from Hydrogen and Oxygen: Noble-Metal Catalytic Method, Fuel-Cell Method and Plasma Method. *Catal. Sci. Technol.* **2016**, *6*, 1593–1610.
- (50) Stephens, R. E.; Ke, B.; Trivich, D. The Efficiencies of Some Solids as Catalysts for the Photosynthesis of Hydrogen Peroxide. *The Journal of Physical Chemistry* **1955**, *59*, 966–969.
- (51) Freund, T.; Gomes, W. P. Electrochemical Methods for Investigating Catalysis by Semiconductors. *Catalysis Reviews: Science and Engineering* **1970**, *3*, 1–36.
- (52) Shao, M.; Chang, Q.; Dodelet, J.-P.; Chenitz, R. Recent Advances in Electrocatalysts for Oxygen Reduction Reaction. *Chemical Reviews* **2016**, *116* (6), 3594–3657.
- (53) Rubin, T. R.; Calvert, J. G.; Rankin, G. T.; MacNevin, W. Photochemical Synthesis of Hydrogen Peroxide at Zinc Oxide Surfaces 1. *Journal of the American Chemical Society* **1953**, *75* (12), 2850–2853.
- (54) Shiraishi, Y.; Kanazawa, S.; Kofuji, Y.; Sakamoto, H.; Ichikawa, S.; Tanaka, S.; Hirai, T. Sunlight-Driven Hydrogen Peroxide Production from Water and Molecular Oxygen by Metal-Free Photocatalysts. *Angewandte Chemie - International Edition* **2014**, *53* (49), 13454–13459.
- (55) Shiraishi, Y.; Kanazawa, S.; Sugano, Y.; Tsukamoto, D.; Sakamoto, H.; Ichikawa, S.; Hirai, T. Highly Selective Production of Hydrogen Peroxide on Graphitic Carbon Nitride (G-C₃N₄) Photocatalyst Activated by Visible Light. *ACS Catalysis* **2014**, *4* (3), 774–780.
- (56) Jakesova, M.; Apaydin, D. H.; Sytnyk, M.; Oppelt, K.; Heiss, W.; Sariciftci, N. S.; Glowacki, E. D. Hydrogen-Bonded Organic Semiconductors as Stable Photoelectrocatalysts for Efficient Hydrogen Peroxide Photosynthesis. *Advanced Functional Materials* **2016**, *26* (29), 5248–5254.
- (57) Węclawski, M. K.; Jakešová, M.; Charyton, M.; Demitri, N.; Koszarna, B.; Oppelt, K.; Sariciftci, S.; Gryko, D. T.; Głowacki, E. D. Biscoumarin-Containing Acenes as Stable Organic Semiconductors for Photocatalytic Oxygen Reduction to Hydrogen Peroxide. *J. Mater. Chem. A* **2017**, 20780–20788.
- (58) Song, C.; Zhang, L.; Zhang, J.; Wilkinson, D. P.; Baker, R. Temperature Dependence of Oxygen Reduction Catalyzed by Cobalt Fluoro-Phthalocyanine Adsorbed on a Graphite Electrode. *Fuel Cells* **2007**, *7* (1), 9–15.
- (59) *Encyclopedia of Inorganic Chemistry*; Ma, Z., Zaera, F., Eds.; John Wiley: New-York, 2006.
- (60) Hawecker, J.; Lehn, J.-M.; Ziessel, R. Electrocatalytic Reduction of Carbon Dioxide Mediated by Re(bipy)(CO)₃Cl (Bipy = 2,2'-Bipyridine). *Journal of the Chemical Society, Chemical Communications* **1984**, 984 (6), 328.
- (61) O'Toole, T. R.; Sullivan, B. P.; Bruce, M. R. M.; Margerum, L. D.; Murray, R. W.; Meyer, T. J. Electrocatalytic Reduction of CO₂ by a Complex of Rhenium in Thin Polymeric Films. *Journal of Electroanalytical Chemistry* **1989**, *259* (1–2), 217–239.
- (62) Windle, C. D.; Pastor, E.; Reynal, A.; Whitwood, A. C.; Vaynzof, Y.; Durrant, J. R.; Perutz, R. N.; Reisner, E. Improving the Photocatalytic Reduction of CO₂ to CO through Immobilisation of a Molecular Re Catalyst on TiO₂. *Chemistry - A European Journal* **2015**, *21* (9), 3746–3754.
- (63) Knözinger, H.; Kochloefl, K.; Turek, T. Heterogeneous Catalysis and Solid Catalysts. In *Ullmann's Encyclopedia of Industrial Chemistry*; 2009; Vol. 1, pp 2–110.
- (64) Letheby, H. On the Physiological Properties of Nitro-Benzole and Aniline. *The New England Journal of Medicine* **1862**, *69* (16), 313–320.
- (65) Kallmann, H.; Pope, M. Bulk Conductivity in Organic Crystals. *Nature* **1960**, *185* (4715),

- 753.
- (66) Kallmann, H.; Pope, M. Positive Hole Injection into Organic Crystals. *The Journal of Chemical Physics* **1960**, *32* (1), 300–301.
- (67) Thejo Kalyani, N.; Dhoble, S. J. Organic Light Emitting Diodes: Energy Saving Lighting Technology - A Review. *Renewable and Sustainable Energy Reviews* **2012**, *16* (5), 2696–2723.
- (68) Günes, S.; Neugebauer, H.; Sariciftci, N. S. Conjugated Polymer-Based Organic Solar Cells. *Chemical Reviews* **2007**, *107* (4), 1324–1338.
- (69) Sirringhaus, H. 25th Anniversary Article: Organic Field-Effect Transistors: The Path beyond Amorphous Silicon. *Advanced Materials* **2014**, *26* (9), 1319–1335.
- (70) Tang, C. W. Organic Photovoltaic Cell. *Applied Physics Letters* **1986**, *48*, 183–185.
- (71) Tang, C. W.; Vanslyke, S. A. Organic Electroluminescent Diodes Organic Electroluminescent Diodes. *Applied Physics Letter* **1987**, *51*, 913–915.
- (72) Coropceanu, V.; Cornil, J.; da Silva Filho, D. A.; Olivier, Y.; Silbey, R.; Brédas, J. L. Charge Transport in Organic Semiconductors. *Chemical Reviews* **2007**, *107* (4), 926–952.
- (73) Hains, A. W.; Liang, Z.; Woodhouse, M. A.; Gregg, B. A. Molecular Semiconductors in Organic Photovoltaic Cells. *Chemical Reviews* **2010**, *110* (11), 6689–6735.
- (74) Forrest, S. R.; Thompson, M. E. Introduction: Organic Electronics and Optoelectronics. *Chemical Reviews* **2007**, *107* (4), 923–925.
- (75) Skotheim, T. A.; Reynolds, J. R. *Handbook of Conducting Polymers: Theory, Synthesis, Properties and Characterization*; CRC Press: Florida, 2006.
- (76) Skotheim, T. A.; Reynolds, J. R. *Handbook of Conducting Polymers: Processing and Applications*; CRC Press: Florida, 2007.
- (77) Brabec, C. J.; Dyakonov, V.; Parisi, J.; Sariciftci, N. S. *Organic Photovoltaics: Concepts and Realization*; Springer: New York, 2003.
- (78) Bao, Z.; Locklin, J. *Organic Field-Effect Transistors*; CRC Press: Florida, 2007.
- (79) Sun, S.-S.; Sariciftci, N. S. *Organic Photovoltaics: Mechanism, Materials and Devices*; CRC Press: Florida, 2005.
- (80) Krebs, F. C. *Polymer Photovoltaics - A Practical Approach*; SPIE Press: Washington, 2008.
- (81) Gerischer, H. Electrochemical Photo and Solar Cells Principles and Some Experiments. *Journal of Electroanalytical Chemistry* **1975**, *58* (1), 263–274.
- (82) Genscher, H. Electrochemical Behavior of Semiconductors under Illumination. *Journal of The Electrochemical Society* **1966**, *113* (11), 1174.
- (83) Memming, R. *Semiconductor Electrochemistry*; WILEY-VCH: Weinheim, 2007.
- (84) Sharon, M. *An Introduction to the Physics and Electrochemistry of Semiconductors*; WILEY-VCH: New-York, 2016.
- (85) Elgrishi, N.; Chambers, M. B.; Wang, X.; Fontecave, M. Molecular Polypyridine-Based Metal Complexes as Catalysts for the Reduction of CO₂. *Chemical Society Reviews* **2017**, *46*, 761–796.
- (86) Lehn, J. M.; Zissel, R. Photochemical Generation of Carbon Monoxide and Hydrogen by Reduction of Carbon Dioxide and Water under Visible Light Irradiation. *Proceedings of the National Academy of Sciences of the United States of America* **1982**, *79* (2), 701–704.
- (87) Sullivan, B. P.; Bolinger, C. M.; Conrad, D.; Vining, W. J.; Meyer, T. J. One- and Two-Electron Pathways in the Electrocatalytic Reduction of COP by Fac-Re(bpy)(CO)&I (Bpy = 2,2'-Bipyridine). *J. Chem. Soc., Chem Commun.* **1985**, *864*, 1414–1416.
- (88) Apaydin, D. H.; Schlager, S.; Portenkirchner, E.; Sariciftci, N. S. Organic, Organometallic and Bioorganic Catalysts for Electrochemical Reduction of CO₂. *ChemPhysChem* **2017**.
- (89) Apaydin, D. H.; Schlager, S.; Portenkirchner, E.; Sariciftci, N. S. Organic, Organometallic and Bioorganic Catalysts for Electrochemical Reduction of CO₂. *ChemPhysChem* **2017**, *1–24*.
- (90) Portenkirchner, E.; Oppelt, K.; Ulbricht, C.; Egbe, D. a M.; Neugebauer, H.; Knör, G.; Sariciftci, N. S. Electrocatalytic and Photocatalytic Reduction of Carbon Dioxide to Carbon Monoxide Using the Alkynyl-Substituted rhenium(I) Complex (5,5'- Bisphenylethynyl-2,2'-bipyridyl)Re(CO) 3Cl. *Journal of Organometallic Chemistry* **2012**, *716*, 19–25.
- (91) Smieja, J. M.; Kubiak, C. P. Re (Bipy-tBu) (CO) 3 Cl - Improved Catalytic Activity for Reduction of Carbon Dioxide : IR-Spectroelectrochemical and Mechanistic Studies. **2010**, No. 21, 9283–9289.
- (92) Christensen, P.; Hamnett, A.; Muir, A. V. G.; Timney, J. A. An In Situ Infrared Study of

- CO, Reduction Catalysed by Rhenium Tricarbonyl Bipyridyl Derivatives Paul. *J. Chem. Soc. Dalton Trans.* **1992**, 9 (9), 1455–1463.
- (93) Stor, G. J.; van Outersterp, J. W. M.; Stufkens, D. J. Spectroelectrochemical (IR, W/Vis) Determination of the Reduction Pathways for a Series of $[\text{Re}(\text{CO})_3(\text{a}=\text{diimine})\text{L}']\text{O}^+$ ($\text{L}' = \text{Halide, Otf, THF, MeCN, N-PrCN, PPh}_3, \text{P}(\text{OMe})_3$) Complexes. *Organometallics* **1995**, 54 (14), 1115–1131.
- (94) Johnson, F. P. A.; George, M. W.; Hartl, F.; Turner, J. J. Electrocatalytic Reduction of CO_2 Using the Complexes $[\text{Re}(\text{Bpy})(\text{CO})_3\text{L}]\text{N}(\text{N}) + 1, \text{L})\text{P}(\text{OEt})_3, \text{CH}_3\text{CN}; \text{N})_0$, Catalyst Precursors: Infrared Spectroelectrochemical Investigation. *Organometallics* **1996**, 15 (15), 3374–3387.
- (95) Fujita, E. Photochemical Carbon Dioxide Reduction with Metal Complexes. *Coordination Chemistry Reviews* **1999**, 185–186, 373–384.
- (96) White, J. L.; Baruch, M. F.; Pander III, J. E.; Hu, Y.; Fortmeyer, I. C.; Park, J. E.; Zhang, T.; Liao, K.; Gu, J.; Yan, Y.; Shaw, T. W.; Abelev, E.; Bocarsly, A. B. Light-Driven Heterogeneous Reduction of Carbon Dioxide: Photocatalysts and Photoelectrodes. *Chemical Reviews* **2015**, 115 (23), 12888–12935.
- (97) Ryeol Whang, D.; Apaydin, D. H. Artificial Photosynthesis: Learning from Nature Learning from Nature. *ChemPhot* **2017**.
- (98) Li, K.; Peng, B.; Peng, T. Recent Advances in Heterogeneous Photocatalytic CO_2 Conversion to Solar Fuels. *ACS Catalysis* **2016**, 6 (11), 7485–7527.
- (99) Halmann, M. Photoelectrochemical Reduction of Aqueous Carbon Dioxide on P-Type Gallium Phosphide in Liquid Junction Solar Cells. *Nature*. 1978, pp 115–116.
- (100) Aurian-Blajeni, B.; Halmann, M.; Manassen, J. Electrochemical Measurement on the Photoelectrochemical Reduction of Aqueous Carbon Dioxide on P-Gallium Phosphide and P-Gallium Arsenide Semiconductor Electrodes. *Solar Energy Materials* **1983**, 8 (4), 425–440.
- (101) Canfield, D.; Frese Jr., K. W. Reduction of Carbon Dioxide to Methanol on N- and P-Gallium Arsenide and P-Indium Phosphide. Effect of Crystal Face, Electrolyte and Current Density. *Journal of the Electrochemical Society* **1983**, 130 (8), 1772–1773.
- (102) Barton, E. E.; Rampulla, D. M.; Bocarsly, A. B. Selective Solar-Driven Reduction of CO_2 to Methanol Using a Catalyzed. *J. Am. Chem. Soc* **2008**, 130, 6342–6344.
- (103) Kumar, B.; Smieja, J. M.; Sasayama, A. F.; Kubiak, C. P. Tunable, Light-Assisted Co-Generation of CO and H_2 from CO_2 and H_2O by $\text{Re}(\text{bipy-tbu})(\text{CO})_3\text{Cl}$ and P-Si in Non-Aqueous Medium. *Chemical Communications* **2012**, 48 (2), 272.
- (104) Zhang, L.; Zhu, D.; Nathanson, G. M.; Hamers, R. J. Selective Photoelectrochemical Reduction of Aqueous CO_2 to CO by Solvated Electrons. *Angewandte Chemie - International Edition* **2014**, 53 (37), 9746–9750.
- (105) Lessio, M.; Carter, E. A. What Is the Role of Pyridinium in Pyridine-Catalyzed CO_2 Reduction on P - GaP Photocathodes? *J. Am. Chem. Soc* **2015**, 137, 13248–13251.
- (106) Kumar, B.; Smieja, J. M.; Kubiak, C. P. Photoreduction of CO_2 on P-Type Silicon Using $\text{Re}(\text{Bipy-Bu T})(\text{CO})_3\text{Cl}$: Photovoltages Exceeding 600 mV for the Selective Reduction of CO_2 to CO. *J. Phys. Chem. C* **2010**, 114, 14220–14223.
- (107) Ghosh, P.; Spiro, T. G. Photoelectrochemistry of tris(bipyridyl)ruthenium(II) Covalently Attached to N-Type tin(IV) Oxide. *Journal of the American Chemical Society* **1980**, 102 (17), 5543–5549.
- (108) Windle, C. D.; Reisner, E. Heterogenised Molecular Catalysts for the Reduction of CO_2 to Fuels. *CHIMIA International Journal for Chemistry* **2015**, 69 (7–8), 435–441.
- (109) Rosser, T. E.; Windle, C. D.; Reisner, E. Electrocatalytic and Solar-Driven CO_2 Reduction to CO with a Molecular Manganese Catalyst Immobilized on Mesoporous TiO_2 . *Angewandte Chemie International Edition* **2016**, 1–6.
- (110) Toole, T. R. O.; Margerum, L. D.; Westmoreland, T. D.; Vining, W. J.; Murray, R. W.; Meyer, T. J. Electrocatalytic Reduction of COs at a Chemically Modified Electrode. **1985**, No. 1416, 1416–1417.
- (111) Cosnier, S.; Deronzier, A.; Moutet, J.-C. ELECTROCHEMICAL COATING OF A PLATINUM ELECTRODE BY A POLY(PYRROLE) FILM CONTAINING THE Fac-Re(2,2'-BIPYRIDINE)(CO) $_3$ Cl SYSTEM. *Journal of Electroanalytical Chemistry* **1986**, 207, 315–321.
- (112) Portenkirchner, E.; Gasiorowski, J.; Oppelt, K.; Schlager, S.; Schwarzinger, C.; Neugebauer, H.; Knör, G.; Sariciftci, N. S. Electrocatalytic Reduction of Carbon Dioxide to Carbon Monoxide by a Polymerized Film of an Alkynyl-Substituted Rhenium(I) Complex.

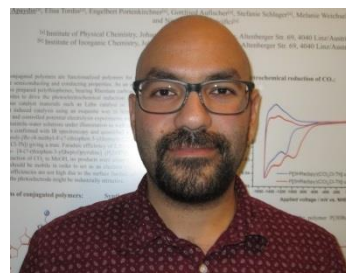
- ChemCatChem* **2013**, 5 (7), 1790–1796.
- (113) Nervi, C.; Sun, C.; Prosperini, S.; Quagliotto, P.; Viscardi, G.; Yoon, S.; Gobetto, R. Electrocatalytic Reduction of CO₂ by Thiophene-Substituted Rhenium(I) Complexes and by Their Polymerized Films. *Dalton Trans.* **2016**, 45, 14678–14688.
- (114) Hassel, A. W.; Fushimi, K.; Seo, M. An Agar-Based Silver-Silver Chloride Reference Electrode for Use in Micro-Electrochemistry. *Electrochemistry Communications* **1999**, 1, 180–183.
- (115) Sandroni, M.; Volpi, G.; Fiedler, J.; Buscaino, R.; Viscardi, G.; Milone, L.; Gobetto, R.; Nervi, C. Iridium and Ruthenium Complexes Covalently Bonded to Carbon Surfaces by Means of Electrochemical Oxidation of Aromatic Amines. *Catalysis Today* **2010**, 158 (1–2), 22–28.
- (116) Pinson, J. Electrochemical Bonding of Amines to Carbon Fiber Surfaces. **1990**, 137 (6).
- (117) Harris, D. C.; Bertolucci, M. D. *Symmetry and Spectroscopy: An Introduction to Vibrational and Electronic Spectroscopy*; Dover Publishing, 1978.
- (118) Gamry. Basics of Electrochemical Impedance Spectroscopy.
- (119) Aaron, D. S. Transport in Fuel Cells : Electrochemical Impedance Spectroscopy and Neutron Imaging Studies Transport in Fuel Cells : Electrochemical Impedance Spectroscopy, Georgia Institute of Technology, 2010.
- (120) Ali, M. Studies of the Use of Electrochemical Impedance Spectroscopy to Characterize and Assess the Performance of Lacquers Used to Protect Aluminum Sheet and Can Ends, University of Ottawa, 2013.
- (121) Głowacki, E. D.; Irimia-Vladu, M.; Kaltenbrunner, M.; Gąsiorowski, J.; White, M. S.; Monkowius, U.; Romanazzi, G.; Suranna, G. P.; Mastroianni, P.; Sekitani, T.; Bauer, S.; Someya, T.; Torsi, L.; Sariciftci, N. S. Hydrogen-Bonded Semiconducting Pigments for Air-Stable Field-Effect Transistors. *Advanced Materials* **2013**, 25 (11), 1563–1569.
- (122) Akita, M.; Osaka, I.; Takimiya, K. Quinacridone-Diketopyrrolopyrrole-Based Polymers for Organic Field-Effect Transistors. *Materials* **2013**, 6 (3), 1061–1071.
- (123) Labana, S. S.; Labana, L. L. Chemical Reviews. *Nature* **1970**, 227 (1), 419–419.
- (124) Apaydin, D. H.; Głowacki, E. D.; Portenkirchner, E. Direct Electrochemical Capture and Release of Carbon Dioxide Using an Industrial Organic Pigment : Quinacridone **
Angewandte. Angewandte Chemie - International Edition **2014**, 53, 6819–6822.
- (125) Apaydin, D. H.; Głowacki, E. D.; Portenkirchner, E.; Sariciftci, N. S. Direkte Elektrochemische Speicherung Und Freisetzung von Kohlendioxid Unter Der Verwendung Eines Industripigments: Chinacridon. *Angewandte Chemie* **2014**, 126, 6937–6940.
- (126) Głowacki, E. D.; Apaydin, D. H.; Bozkurt, Z.; Monkowius, U.; Demirak, K.; Tordin, E.; Himmelsbach, M.; Schwarzinger, C.; Burian, M.; Lechner, R. T.; Demitri, N.; Voss, G.; Sariciftci, N. S. Air-Stable Organic Semiconductors Based on 6,6'-Dithienylindigo and Polymers Thereof. *Journal of Materials Chemistry C* **2014**, 2 (38), 8089–8097.
- (127) Nagaoka, T.; Nishii, N.; Fujii, K.; Ogura, K. Mechanisms of Reductive Addition of CO₂ to Quinones in Acetonitrile. *Journal of Electroanalytical Chemistry* **1992**, 322 (1–2), 383–389.
- (128) Głowacki, E. D.; Voss, G.; Demirak, K.; Havlicek, M.; Sünger, N.; Okur, A. C.; Monkowius, U.; Gąsiorowski, J.; Leonat, L.; Sariciftci, N. S. A Facile Protection-Deprotection Route for Obtaining Indigo Pigments as Thin Films and Their Applications in Organic Bulk Heterojunctions. *Chemical communications (Cambridge, England)* **2013**, 49, 6063–6065.
- (129) Glowacki, E. D.; Leonat, L.; Voss, G.; Bodea, M.; Bozkurt, Z.; Irimia-Vladu, M.; Bauer, S.; Sariciftci, N. S. Natural and Nature-Inspired Semiconductors for Organic Electronics. *Organic Semiconductors in Sensors and Bioelectronics IV* **2011**, 8118, 81180M–81180M–10.
- (130) Glowacki, E. D.; Voss, G.; Leonat, L.; Irimia-Vladu, M.; Bauer, S.; Sariciftci, N. S. Indigo and Tyrian Purple - From Ancient Natural Dyes to Modern Organic Semiconductors. *Israel Journal of Chemistry* **2012**, 52 (6), 540–551.
- (131) Deblase, C. R.; Hernández-Burgos, K.; Rotter, J. M.; Fortman, D. J.; Dos S. Abreu, D.; Timm, R. A.; Diógenes, I. C. N.; Kubota, L. T.; Abruña, H. D.; Dichtel, W. R. Cation-Dependent Stabilization of Electrogenerated Naphthalene Diimide Dianions in Porous Polymer Thin Films and Their Application to Electrical Energy Storage. *Angewandte Chemie - International Edition* **2015**, 54 (45), 13225–13229.
- (132) Vadehra, G. S.; Maloney, R. P.; Garcia-garibay, M. A.; Dunn, B.; Vadehra, G. S.; Maloney, R. P.; Garibay, M. A. G.; Dunn, B. Naphthalene Diimide Based Materials with Adjustable Redox Potentials : Evaluation for Organic Lithium-Ion Batteries Naphthalene

- Diimide Based Materials with Adjustable Redox Potentials: Evaluation for Organic Lithium-Ion Batteries. **2014**.
- (133) Andric, G.; Boas, J. F.; Bond, A. M.; Fallon, G. D.; Ghiggino, K. P.; Hogan, C. F.; Hutchison, J. A.; Lee, M. A. P.; Langford, S. J.; Pilbrow, J. R.; Troup, G. J.; Woodward, C. P. Spectroscopy of Naphthalene Diimides and Their Anion Radicals. *Australian Journal of Chemistry* **2004**, *57* (10), 1011–1019.
- (134) Nyquist, R. A.; Potts, W. J. Infrared Absorptions Characteristic of Organic Carbonate Derivatives and Related Compounds. *Spectrochimica Acta* **1961**, *17* (1957), 679–697.
- (135) Apaydin, D. H.; Gora, M.; Portenkirchner, E.; Oppelt, K. T.; Neugebauer, H.; Jakesova, M.; Eric, D. G.; Kunze-liebha, J. Electrochemical Capture and Release of CO₂ in Aqueous Electrolytes Using an Organic Semiconductor Electrode. **2017**.
- (136) Barbier, B. Electrochemical Bonding of Amines to Carbon Fiber Surfaces Toward Improved Carbon-Epoxy Composites. *Journal of The Electrochemical Society* **1990**, *137* (6), 1757.
- (137) Shu, C. F.; Wrighton, M. S. Synthesis and Charge-Transport Properties of Polymers Derived from the Oxidation of 1-Hydroxy-1'-(6-(Pyrrol-1-Yl)hexyl)-4,4'-bipyridinium Bis(hexafluorophosphate) and Demonstration of a pH-Sensitive Microelectrochemical Transistor Derived from the Redox pro. *The Journal of Physical Chemistry* **1988**, *92* (18), 5221–5229.
- (138) Sariciftci, N. S.; Mehring, M.; Gaudl, K. U.; Bauerle, P.; Neugebauer, H.; Neckel, A. 3rd-Generation of Conducting Polymers - Spectroelectrochemical Investigations on Viologen Functionalized Poly (3-Alkylthiophenes). *Journal of Chemical Physics* **1992**, *96* (9), 7164–7170.
- (139) Deronzier, A.; Moutet, J. C. Functionalized Polypyrroles. New Molecular Materials for Electrocatalysis and Related Applications. *Accounts of Chemical Research* **1989**, *22* (7), 249–255.
- (140) Roncali, J.; Garreau, R.; Delabouglise, D.; Garnier, F.; Lemaire, M. A Molecular Approach of Poly(thiophene) Functionalization. *Synthetic Metals* **1989**, *28* (1–2), 341–348.
- (141) Bäuerle, P.; Gaudl, K. -U. Synthesis and Properties of Viologen Functionalized poly(3-alkylthienylenes). *Advanced Materials* **1990**, *2* (4), 185–188.
- (142) Inagaki, T.; Skotheim, T. A.; Lee, H. S.; Okamoto, Y.; Samuelson, L.; Tripathy, S. Chemically Modified Polypyrrole. *Synthetic Metals* **1989**, *28*, 245–250.
- (143) Bauerle, P.; Gaudl, K. U. New Functionalized Polythiophenes. *Synthetic metals* **1991**, *43*, 3037–3042.
- (144) Windle, C. D.; Pastor, E.; Reynal, A.; Whitwood, A. C.; Vaynzof, Y.; Durrant, J. R.; Perutz, R. N.; Reisner, E. Improving the Photocatalytic Reduction of CO₂ to CO through Immobilisation of a Molecular Re Catalyst on TiO₂. *Chemistry - A European Journal* **2015**, *21* (9), 3746–3754.
- (145) Yoshida, T.; Koji, T.; Shousuke, T.; Katsutoshi, Y.; Masao, K. Electrocatalytic Reduction of CO₂ in Water by [Re(bpy)(CO)3Br] and [Re(terpy)(CO)3Br] Complexes Incorporated into Coated Nafion Membrane (Bpy = 2,2'-bipyridine; Terpy = 2,2' : 6',2"-Terpyridine). *J. Chem. Soc., Chem Commun.* **1993**, No. 7, 631–633.
- (146) Yoshida, T.; Kamato, K.; Tsukamoto, M.; Iida, T.; Schlettwein, D.; Wöhrle, D.; Kaneko, M. Selective Electrocatalysis for CO₂ Reduction in the Aqueous Phase Using Cobalt Phthalocyanine/poly-4-Vinylpyridine Modified Electrodes. *Journal of Electroanalytical Chemistry* **1995**, *385* (2), 209–225.
- (147) Christensen, P.; Hamnett, A.; Muir, A. V. G.; Timney, J. a.; Higgins, S. Growth and Electrochemical Behaviour of a Poly [Tricarbonyl(vinylbipyridyl)rhenium Chloride] Film. Heterogeneous Reduction of CO₂. *Journal of the Chemical Society, Faraday Transactions* **1994**, *90* (3), 459–469.
- (148) Seshadri, G.; Lin, C.; Bocarsly, A. B. A New Homogeneous Electrocatalyst to Methanol at Low Overpotential for the Reduction of Carbon Dioxide. *Journal of Electroanalytical Chemistry* **1994**, *372*, 145–150.
- (149) Cole, E. B.; Lakkaraju, P. S.; Rampulla, D. M.; Morris, A. J.; Abelev, E.; Bocarsly, A. B. Using a One Electron Shuttle for the Multi- Electron Reduction of CO₂ to Methanol. *Journal of American Chemical Society* **2010**, No. 12, 11539–11551.
- (150) Ertem, M. Z.; Konezny, S. J.; Araujo, C. M.; Batista, V. S. Functional Role of Pyridinium during Aqueous Electrochemical Reduction of CO₂ on Pt(111). *J. Phys. Chem. Lett.* **2013**, *4* (5), 745–748.
- (151) Morris, A. J.; McGibbon, R. T.; Bocarsly, A. B. Electrocatalytic Carbon Dioxide Activation:

- The Rate-Determining Step of Pyridinium-Catalyzed CO₂ Reduction. *ChemSusChem* **2011**, 4 (2), 191–196.
- (152) Tossell, J. A. Calculation of the Properties of Molecules in the Pyridine Catalyst System for the Photochemical Conversion of CO₂ to Methanol. *Computational and Theoretical Chemistry* **2011**, 977 (1–3), 123–127.
- (153) Lucio, A. J.; Shaw, S. K. Pyridine and Pyridinium Electrochemistry on Polycrystalline Gold Electrodes and Implications for CO₂ Reduction. *Journal of Physical Chemistry C* **2015**, 119 (22), 12523–12530.
- (154) Rybchenko, S. I.; Touhami, D.; Wadhawan, J. D.; Haywood, S. K. Study of Pyridine-Mediated Electrochemical Reduction of CO₂ to Methanol at High CO₂ Pressure. *ChemSusChem* **2016**, 1–11.
- (155) Portenkirchner, E.; Enengl, C.; Enengl, S.; Hinterberger, G.; Schlager, S.; Apaydin, D.; Neugebauer, H.; Knör, G.; Sariciftci, N. S. A Comparison of Pyridazine and Pyridine as Electrocatalysts for the Reduction of Carbon Dioxide to Methanol. *ChemElectroChem* **2014**, 1 (9).
- (156) Costentin, C.; Robert, M.; Savéant, J.-M. Catalysis of the Electrochemical Reduction of Carbon Dioxide. *Chem. Soc. Rev.* **2013**, 42 (6), 2423–2436.
- (157) Fox, M. A.; Akaba, R. Curve Crossing in the Cyclic Voltammetric Oxidation of 2-Phenylbornene. Evidence for an ECE Reaction Pathway. *Journal of the American Chemical Society* **1983**, 105 (11), 3460–3463.
- (158) Amatore, C.; Pinson, J.; Savéant, J. M.; Thiebault, A. Trace Crossings in Cyclic Voltammetry and Electrochemical Inducement of Chemical Reactions. Aromatic Nucleophilic Substitution. *Journal of Electroanalytical Chemistry* **1979**, 107 (1), 59–74.
- (159) Apaydin, D. H.; Tordin, E.; Portenkirchner, E.; Aufischer, G.; Schlager, S.; Weichselbaumer, M.; Oppelt, K.; Sariciftci, N. S. Photoelectrochemical Reduction of CO₂ Using Third-Generation Conjugated Polymers. *ChemistrySelect* **2016**, 1 (6), 1156–1162.
- (160) Portenkirchner, E.; Enengl, C.; Enengl, S.; Hinterberger, G.; Stefanie, S.; Apaydin, D.; Neugebauer, H.; Knör, G.; Sariciftci, N. S. A Comparison of Pyridazine and Pyridine as Electrocatalysts for the Reduction of Carbon Dioxide to Methanol. *ChemElectroChem* **2014**, 1, 1543–1548.
- (161) Qu, Q.; Geng, H.; Peng, R.; Cui, Q.; Gu, X.; Li, F.; Wang, M. Chemically Binding Carboxylic Acids onto TiO₂ Nanoparticles with Adjustable Coverage by Solvothermal Strategy. *Langmuir* **2010**, 26 (12), 9539–9546.
- (162) Auer, A.; Jonasson, N. S. W.; Apaydin, D. H.; Mardare, A. I.; Neri, G.; Lichtinger, J.; Gernhäuser, R.; Kunze-Liebhäuser, J.; Portenkirchner, E. Optimized Design Principles for Silicon-Coated Nanostructured Electrode Materials and Their Application in High-Capacity Lithium-Ion Batteries. *Energy Technology* **2017**, 5 (12), 2253–2264.
- (163) Kuivila, H. G. Electrophilic Displacement Reactions. III. Kinetics of the Reaction between Hydrogen Peroxide and Benzeneboronic Acid¹. *J. Am. Chem. Soc.* **1954**, 76 (8), 870–874.
- (164) Kuivila, H. G.; Armour, A. G. Electrophilic Displacement Reactions. IX. Effects of Substituents on Rates of Reactions between Hydrogen Peroxide and Benzeneboronic Acid. *Journal of the American Chemical Society* **1957**, 79 (21), 5659–5662.
- (165) Fabregat-Santiago, F.; Garcia-Belmonte, G.; Mora-Seró, I.; Bisquert, J. Characterization of Nanostructured Hybrid and Organic Solar Cells by Impedance Spectroscopy. *Physical Chemistry Chemical Physics* **2011**, 13 (20), 9083.
- (166) Köleli, F.; Röpke, T.; Hamann, C. H. Electrochemical Impedance Spectroscopic Investigation of CO₂ Reduction on Polyaniline in Methanol. *Electrochimica Acta* **2003**, 48 (11), 1595–1601.
- (167) Growcock, F. B.; Jasinski, R. J. Time-Resolved Impedance Spectroscopy of Mild Steel in Concentrated Hydrochloric Acid. *Journal of The Electrochemical Society* **1989**, 136 (8), 2310.
- (168) Portenkirchner, E.; Gasiorowski, J.; Oppelt, K.; Schlager, S.; Schwarzinger, C.; Neugebauer, H.; Knör, G.; Sariciftci, N. S. Electrocatalytic Reduction of Carbon Dioxide to Carbon Monoxide by a Polymerized Film of an Alkynyl-Substituted Rhenium(I) Complex. *ChemCatChem* **2013**, 5 (7), 1790–1796.
- (169) Hoffman, A. J.; Carraway, E. R.; Hoffmann, M. R. Photocatalytic Production of H₂O₂ and Organic Peroxides on Quantum-Sized Semiconductor Colloids. *Environmental Science and Technology* **1994**, 28 (5), 776–785.

- (170) Heichal-Segal, O.; Rappoport, S.; Braun, S. Immobilization in Alginate-Silicate Sol-Gel Matrix Protects β -Glucosidase Against Thermal and Chemical Denaturation. *Bio/Technology* **1995**, *13*, 798–800.
- (171) Reda, T.; Plugge, C. M.; Abram, N. J.; Hirst, J. Reversible Interconversion of Carbon Dioxide and Formate by an Electroactive Enzyme. *Proceedings of the National Academy of Sciences of the United States of America* **2008**, *105* (31), 10654–10658.
- (172) Schlager, S.; Neugebauer, H.; Haberbauer, M.; Hinterberger, G.; Sariciftci, N. S. Direct Electrochemical Addressing of Immobilized Alcohol Dehydrogenase for the Heterogeneous Bioelectrocatalytic Reduction of Butyraldehyde to Butanol. *ChemCatChem* **2015**, *7* (6), 967–971.
- (173) Schlager, S.; Dumitru, L. M.; Haberbauer, M.; Fuchsbauer, A.; Neugebauer, H.; Hiemetsberger, D.; Wagner, A.; Portenkirchner, E.; Sariciftci, N. S. Electrochemical Reduction of Carbon Dioxide to Methanol by Direct Injection of Electrons into Immobilized Enzymes on a Modified Electrode. *ChemSusChem* **2016**, *9* (6), 631–635.

6. Curriculum Vitae



Personal Information

Name / Surname	Dogukan Hazar Apaydin
Address	Linz Institute for Organic Solar Cells, Physical Chemistry Johannes Kepler University, Altenberger Straße, 69 4040-Linz / Austria
E-Mail	dogukan.apaydin@jku.at
Mobile	+43 664 485 83 41
Date of Birth	28.05.1988
Gender	Male

Publications

ISI h-index: 13

Google Scholar h-index: 13

2018

1. **D. H. Apaydin**, H. Seelajaroen, O. Pongsakul, P. Thamyongkit, N. S. Sariciftci, J. Kunze-Liebhäuser, E. Portenkirchner, *ChemCatChem* (in press)

2017

2. D. Solonenko, J. Gasiorowski, **D. H. Apaydin**, K. Oppelt, M. Nuss, W. Keawsongsaeng, G. Salvan, K. Hingerl, N. S. Sariciftci, D. RT Zahn, P. Thamyongkit *The Journal of Physical Chemistry C* 121 (2017) 24397-24407
3. **D. H. Apaydin**, M. Gora, E. Portenkirchner, K. T. Oppelt, H. Neugebauer, M. Jakesova, E. D. Głowacki, J. Kunze-Liebhäuser, M. Zagorska, J. Mieczkowski, N. S. Sariciftci *ACS Applied Materials and Interfaces* 9 (2017) 12919-12923
4. **D. H. Apaydin**, S. Schlager, E. Portenkirchner, N. S. Sariciftci *ChemPhysChem* 18 (2017) 3094-3116
5. R. Rybakiewicz, E. D. Głowacki, L. Skorcka, S. Pluczyk, P. Zassowski, **D. H. Apaydin**, M. Lapkowski, M. Zagorska, A. Pron *Chemistry-A European Journal* 23 (2017) 2839-2851

6. D.E. Yildiz, **D. H. Apaydin**, L. Toppare, A. Cirpan *Journal of Applied Polymer Science* (2017) 10.1002/app.44817
7. S. Tombe, G. Adam, H. Heilbrunner, **D. H. Apaydin**, C. Ulbricht, N. S. Sariciftci, C. J. Arendse, E. Iwuoha, M. C. Scharber *Journal of Materials Chemistry C* 5 (2017) 1714-1723.
8. A. Auer, N. S. W. Johanasson, **D. H. Apaydin**, A. I. Mardare, G. Neri, J. Lichtinger, R. Gernhäuser, J. Kunze-Liebhäuser, E. Portenkirchner *Energy Technology* 5 (2017) 2253-2264.
9. S. Demchyshyn, J. M. Roemer, H. Groß, H. Heilbrunner, C. Ulbricht, **D. Apaydin**, A. Böhm, U. Rütt, F. Bertram, G. Hesser, M. C. Scharber, N. S. Sariciftci, B. Nickel, S. Bauer, E. D. Głowacki, M. Kaltenbrunner *Science Advances* (2017) 10.1126/sciadv.1700738
10. M. Wang, V. Artero, L. Hammarström, J. Martinez, J. Karlsson, D. Gust, P. Summers, C. Machan, P. Brueggeller, C. D. Windle, Y. Kageshima, R. Cogdell, K. R. Tolod, A. Kibler, **D. H. Apaydin**, E. Fujita, J. Ehrmaier, S. Shima, E. Gibson, F. Karadas, A. Harriman, H. Inoue, A. Kudo, T. Takayama, M. Wasielewski, F. Cassiola, M. Yagi, H. Ishida, F. Franco, S. O. Kang, D. Nocera, C. Li, F. D. Fonzo, H. Park, L. Sun, T. Setoyama, Y. S. Kang, O. Ishitani, J. Shen, H. Son, S. Masaoka *Faraday Discussions* 198 (2017) 353-395
11. S. Schlager, A. Dibenedetto, M. Aresta, **D. H. Apaydin**, L. M. Dumitru, H. Neugebauer, N. S. Sariciftci *Energy Technology* 5 (2017) 812-821.
12. H. Kumagai, L. Hammarström, D. R. Whang, Y. Shinohara, J. Martinez, J. Karlsson, P. Summers, C. D. Windle, M. Kodera, R. Cogdell, K. R. Tolod, **D. H. Apaydin**, E. Fujita, A. Kibler, F. Fan, E. A. Gibson, H. Usami, A. Iwase, H. Inoue, A. Kudo, D. Gust, K. Domen, F. Cassiola, K. Takagi, S. O. Kang, A. Yamakata, C. Li, L. Sun, H. Park, Y. S. Kang, R. Li, F. D. Fonzo, T. Setoyama, O. Ishitani *Faraday Discussions* 198 (2017) 481-507

2016

13. A. Aljabour, **D. H. Apaydin**, H. Coskun, F. Ozel, M. Ersoz, P. Stadler, N. S. Sariciftci, M. Kus *ACS Applied Materials and Interfaces* 8 (2016) 31695-31701.
14. Y. Li, P. Bober, **D. H. Apaydin**, T. Syrový, N. S. Sariciftci, J. Hromadková, I. Sapurina, M. Trchova, J. Stejskal *Synthetic Metals* 221 (2016) 67-74.
15. G. Adam, M. Kaltenbrunner, E. D. Glowacki, **D. H. Apaydin**, M. S. White, H. Heilbrunner, S. Tombe, P. Stadler, B. Ernecker, C. W. Klampfl, N. S. Sariciftci, M. C. Scharber *Solar Energy Materials and Solar Cells* 157 (2016) 318-325.
16. W. Keawsongsaeng, J. Gasiorowski, P. Denk, K. Oppelt, **D. H. Apaydin**, R. Rojanathanes, K. Hingerl, M. Scharber, N. S. Sariciftci, P. Thamyongkit *Advanced Energy Materials* 6 (2016) 1600957
17. M. Jakesova, **D. H. Apaydin**, M. Sytnyk, K. Oppelt, W. Heiss, N. S. Sariciftci, and E. D. Glowacki, *Advanced Functional Materials* 26 (2016) 5248-5254.

18. **D. H. Apaydin**, E. Tordin, E. Portenkirchner, G. Aufischer, S. Schlager, M. Weichselbaumer K. Oppelt, N. S. Sariciftci, *ChemistrySelect*, 6 (2016) 1156-1162

2015

19. M. Kaltenbrunner, G. Adam, E. Glowacki, M. Drack, R. Schwödiauer, L. Leonat, **D. H. Apaydin**, H. Groiss, M.C. Scharber, M. S. White, N. S. Sariciftci and S. Bauer, *Nature Materials* 4 (2015), 1032-1039
20. E. Portenkirchner, S. Schlager, **D. H. Apaydin**, K. Oppelt, M. Himmelsbach, D. A. M. Egbe, H. Neugebauer, G. Knör, T. Yoshida, N. S. Sariciftci *Electrocatalysis* 6 (2015) 185-197

2014

21. E. D. Glowacki, **D. H. Apaydin**, Z. Bozkurt, U. Monkowius, K. Demirak, E. Tordin, M. Himmelsbach, C. Schwarzinger, M. Burian, R. T. Lechner, N. Demitri, G. Voss, N. S. Sariciftci *Journal of Materials Chemistry C* 2 (2014) 8089-8097.
22. E. Portenkirchner, **D.H. Apaydin**, G. Aufischer, M. Havlicek, M. Scharber, S. Sariciftci *ChemPhysChem*, 15 (2014), 3634-3638.
23. E. Portenkirchner, C. Enengl, S. Enengl, G. Hinterberger, S. Schlager, **D. H. Apaydin**, H. Neugebauer, G. Knör, N. S. Sariciftci *ChemElectroChem* 1 (2014) 1543-1548.
24. Y. Udum, P. Denk, G. Workneh, **D. H. Apaydin**, C. Teichert, M. White, S. Sariciftci, M. Scharber, *Organic Electronics*, 15 (2014) 997-1001.
25. **D. H. Apaydin**, E. Glowacki, E. Portenkirchner, S. Sariciftci, *Angew. Chem.* 126 (2014) 6937-6940.
26. **D. H. Apaydin**, E. Glowacki, E. Portenkirchner, S. Sariciftci, *Angew. Chem. Int. Ed.* 53 (2014) 6819-6822.

2013

27. D. Kozanoglu, **D. H. Apaydin**, A. Cirpan, E. N. Esenturk, *Organic Electronics*, 13 (2013) 1720-1727.
28. **D. H. Apaydin**, D. E. Yildiz, A. Cirpan, L. Toppare, *Solar Energy Materials and Solar Cells*, 113 (2013) 100-105.
29. S. C. Cevher, N. A. Unlu, A. C. Ozelcaglayan, **D. H. Apaydin**, Y. A. Udum, L. Toppare, A. Cirpan *Journal Of Polymer Science, Part A: Polymer Chemistry* 51, (2013) 1933-1941.
30. D. E. Yildiz, **D. H. Apaydin**, A. Cirpan, L. Toppare, *Journal of Applied Polymer Science*, 128, (2013) 1659-1664.

2012

31. **D. H. Apaydin**, H. Akpınar, M. Sendur, L. Toppare, *Journal of Electroanalytical Chemistry* 665 (2012) 52–57
32. E. Kaya, **D. H. Apaydin**, D. E. Yildiz, L. Toppare, A. Cirpan, *Solar Energy Materials and Solar Cells*, 99 (2012) 321-326
33. M. Karakus, **D. H. Apaydin**, D. E. Yildiz, L. Toppare, A. Cirpan, *Polymer*, 53 (2012) 1198-1202
34. A. C. Ozelcaglayan, M. Sendur, N. Akbasoglu, **D. H. Apaydin**, A. Cirpan, L. Toppare, *Electrochimica Acta*, 67 (2012) 224-229

Awards

Faraday Discussions on Artificial Photosynthesis Best Poster Award “**Electrochemical Capture and Release of Carbon Dioxide Using Organic Semiconductors**” (March 2017, Japan)

Physical Chemistry Chemical Physics Journal 9th International Electrochemistry Meeting Ali Rıza Berkem Poster Award “**Azobenzene Containing Conjugated Polymers And Their Electrochromic Applications**” (September 2011, Turkey)

Conferences

Third generation conjugated polymers for photoelectrochemical reduction of CO₂
D. H. Apaydin, E. Tordin, E. Portenkirchner, G. Aufischer, S. Schlager, M. Weichselbaumer, K. Oppelt, N. S. Sariciftci, MRS Boston (2016) (Oral Presentation)

Carbonyl pigment thin films for efficient electrochemical capture and release of carbon dioxide
D.H. Apaydin, E. D. Glowacki, E. Portenkirchner, S. Sariciftci, MRS Boston (2014) (Oral Presentation)

Direct Electrochemical Capture and Release of CO₂ Using Nature Inspired Pigments,
D.H. Apaydin, E. D. Glowacki, E. Portenkirchner, S. Sariciftci International Winterschool on Bioelectronics (2013) (Oral Presentation)

Photovoltaic Cell Applications and Mobility Measurements of Benzotriazole Based Conjugated Copolymer M. Karakus, **D. H. Apaydin**, D. E. Yildiz, L. Toppare, A. Cirpan 3rd International Nuclear & Renewable Energy Resources Conference (2012)

Power Conversion Efficiency Enhancement of Organic Solar Cells by Addition of Gold Nanoparticles D. Kozanoglu, **D. H. Apaydin**, A. Cirpan, E. Nalbant Esentürk 8th Nanoscience and Nanotechnology Congress (2012) (Poster Presentation)

Electrochromic and Photovoltaic Properties of a Novel Thiophene Substituted Quinoxaline Derivative **D. H. Apaydin** et al. EUPVSEC (2011) (Poster Presentation)

Azobenzene Containing Conjugated Polymers And Their Electrochromic Applications **D. H. Apaydin**, H. Akpınar, M. Sendur, L. Toppare 9th International Electrochemistry Meeting (2011) (Poster Presentation)

Teaching Experience

Dates June 2014 – Present
Occupation Universitätassistent (Exercises in Physical Chemistry / Physikalische Chemie Praktikum)
Employer Johannes Kepler Universität Linz

Dates September 2007 – June 2010
Occupation Student Laboratory Assistant
Employer Istanbul Technical University, Chemistry Department

Education

Dates November 2012 - Present
PhD Student at Johannes Kepler University Linz
Thesis topic: Electrochemical and photoelectrochemical catalysis using organic semiconductors.

Dates August 2010 – July 2012
Degree Awarded Master of Science
Principal Subject Polymer Science and Technology
Institution Middle East Technical University, Ankara (Turkey)

Dates September 2006 – June 2010
Degree Awarded Bachelor of Science
Principal subject Chemistry
Institution Istanbul Technical University, Istanbul (Turkey)

Language Skills

Mother Tongue **Turkish**
Other Languages **English** (Understanding: Proficient User; Speaking: Proficient User; Writing: Proficient User)
German (B1)